Doctoral dissertation

A Study of Alternating Phase Fed Single-Layer Slotted Waveguide Array Antenna at 38 GHz for Low Grating Lobes with Reflection Canceling Stairs

December 2023.

Under the supervision of

Professor ShigeruYoshimori

Associate Professor Yasuhiro Tsunemitsu

Presented by

Wenbo Liu

Mechanics and Electronics Systems Course

Graduate School of Engineering

Takushoku University

Contents

Abstract

This paper presents a simulation and experimental study of a 10 × 10 alternating phase-fed single-layer waveguide slot array antenna with reflection-canceling stairs (RCSs) at 38 GHz. The aim of the study was to improve the aperture efficiency of the antenna. Two optimization methods were employed: 1) RCSs for each slot were proposed and optimized for height and position to minimize reflection, and 2) the broad wall width and slot offset were optimized to suppress grating lobes. A design procedure for the feed part was also presented. The characterization of the proposed antenna was found to be in good agreement with simulation results, with a measured S11 of less than −20 dB and a gain of more than 27.71 dBi at 38 GHz (corresponding to an aperture efficiency of 85.6%). The results of this study demonstrate the feasibility of using the proposed antenna in millimeter-wave communication systems.

Besides, we also derive the underlying physic mechanism of slotted rectangular waveguide antenna in chapter II, discuss the further issues of the devices in chapter VI and present the prospective work in the final chapter VII.

Chapter 1
Introduction

1.1 Brief history of slotted antenna array

In 1865, with the publication of "A Dynamic Theory of electromagnetic field" by James Clerk Maxwell, the fact that the electric and magnetic field propagation as a wave in the space with the speed of light is demonstrated [1]. In 1885, Heinrich Hertz demonstrated direction beams using a parabolic reflector at 66-cm wavelength (454 MHz). And much of the works in the initial time are carried out in microwave frequency bandwidth. Since then, after Guglielmo Marconi invented a dipole antenna transmission system in 1895, the interest was shifted into longer wavelength range for long distance transmission.

The invention of vacuum tubes made the application of high frequency electromagnetic wave hot topics again in the 1930s ~ 1940s. Microwave directional antennas were developed for applications such as transmission, radar and Navigation. It was not until the time of World-war II, the slotted waveguide array antennas emerge on the scene [2,3]. Normally, Alan Blumlein was known as the first inventor of slot antenna in 1938.

An overview of the progress in waveguide slotted arrayed antennas up to 1999 has been presented by [4]. Here, we introduce several milestones. First, it was in Montreal Canada, Watson et al. in McGill university invented waveguide slotted arrayed antenna [5,6]. At these works, Watson et al. demonstrated the usefulness of several kind of slot on the rectangular waveguide, such as broad wall longitude and transverse slots and inclined edge wall slots. Consequently, various works are done to optimize the design method of slotted waveguide arrays antenna. Since in the pre-computer age, simple models with high efficiency are required to predict the performance of device with the limit simulation resource. Stevenson proposed an equivalent circuit model [7]. He successfully calculated the slotted waveguide antenna by using basic circuit parameters ($R, G, j\omega L, j\omega C$). Then, Stegen provided carefully slot characterization result for antenna design [8]. Besides, novel algorisms are developed to calculate the slotted waveguide antenna without using powerful simulation tools, such as variational method by Oliner [9] and the moment method by

Vu Khac[10]. A comprehensive simulation model that includes slot models, mutual coupling effect and waveguide model has been published by Elliot in 1984 [11]. Since then, the so-called Elliot method became popular in slotted waveguide arrayed antennas design.

Nowadays, the research on slotted waveguide arrayed antenna became hot topics again due to 2 aspects. First, the explosive growing requirement of multi-medias information for every user makes the extremely high data-capacity wireless communication indispensable in daily life of almost everyone. As a result, the research and commercial interests are focus on millimeter-applications, such as satellite communication and fifth-generation (5G) communication [12-19]. Slotted waveguide arrayed antenna is feasible to be fabricated for this application bandwidth. Besides, these antennas offer advantages, including an all-metal structure, low loss and high power. Second is the development of simulation technology. Thanks to the incredible development of computers, full wavelength simulation becomes possible. By solving Maxwell's equation through finite element method (FEM), precious simulation with perfect agreement with experiment can be done. In this work, the simulation works are finished with the support of commercial software Femtet by (Murata Software Co., Ltd.)

1.2 Single-layer alternative-phase-fed configuration

Figure 1.1 shows a configuration of single-layer slotted array antennas, where T-junctions connect to the end of slotted waveguides are employed as feeding parts [20]. The advantage of single-layer configuration is outstanding comparing to multiple layer configuration in terms of fabrication simplicity as shown in Figure 1.1. One more essential technic that makes the fabrication easier is alternative-phase-fed technics by carefully designing the T-junction. Since the perfect alternative phase condition between 2 adjacent waveguides cancel the sidewall current, we can individually fabricate the base plate and the radiating plate and then connect them with screws [see Figure 1.1.].

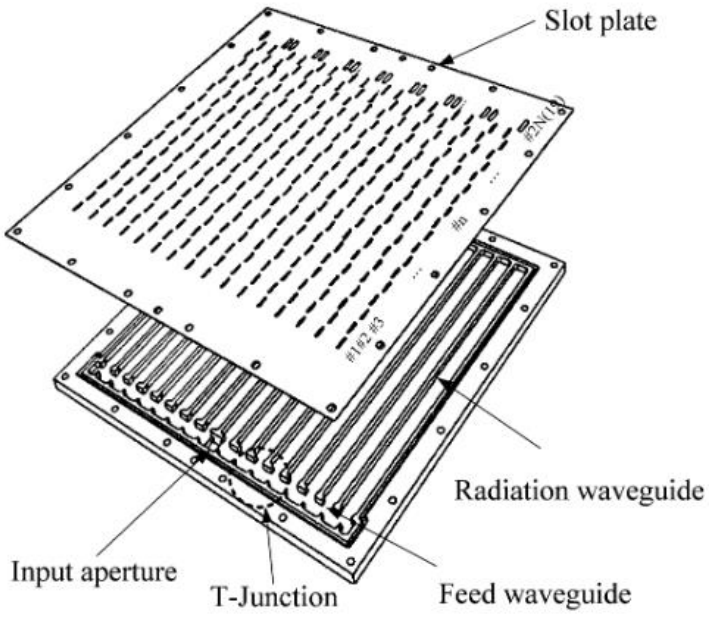

Fig. 1.1. Configuration of single-layer slotted waveguide arrayed antennas with T-junction in [20]. *Copyright © 2006, IEEE*

However, the draw backs are shown in Figure 1.2, where we find the so-called frequency squirting effect that beam direction will slightly change with frequency due to the asymmetric feeding configuration employ only at one end of waveguide. To solve this issue, Park et al. in [20] proposed center-fed configuration as shown in Figure 1.3. As a result, frequency-independent beam direction is demonstrated in Figure 1.4.

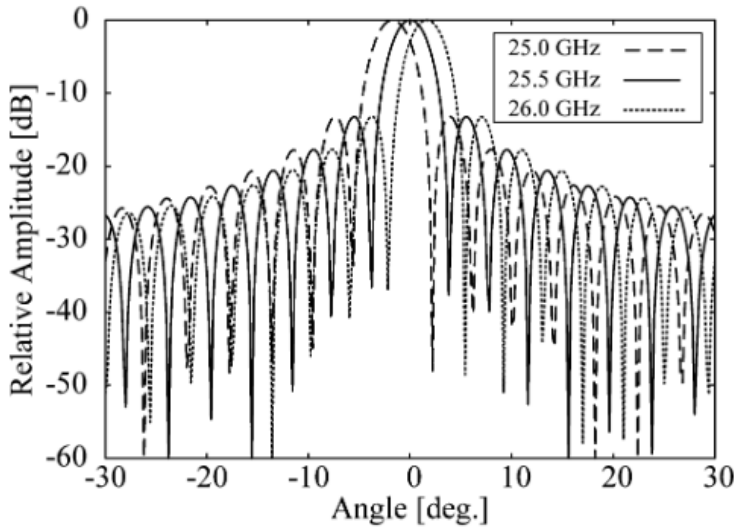

Fig. 1.2. Measured radiation pattern of end-feeding single layer slotted waveguide arrayed antennas in [20]. *Copyright © 2006, IEEE*

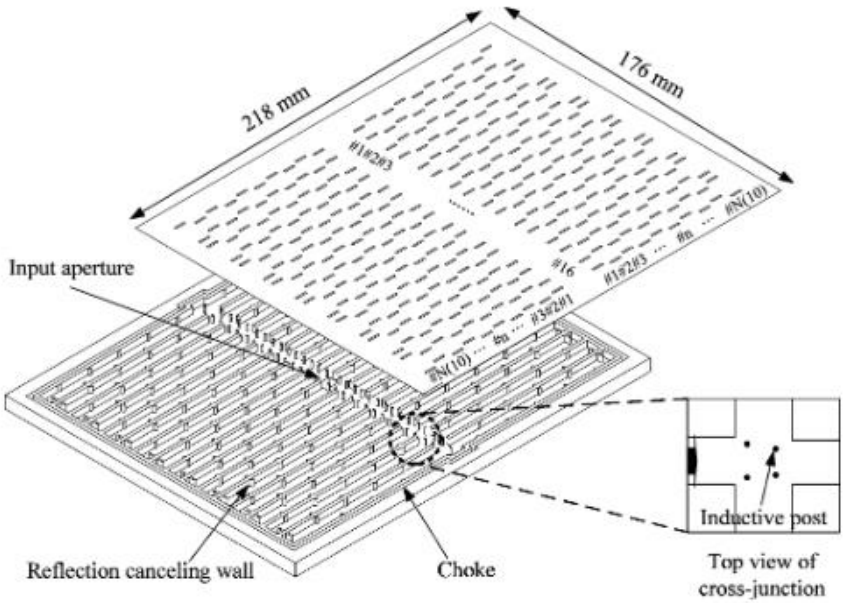

Fig. 1.3. Configuration of center-fed [20]. *Copyright © 2006, IEEE*

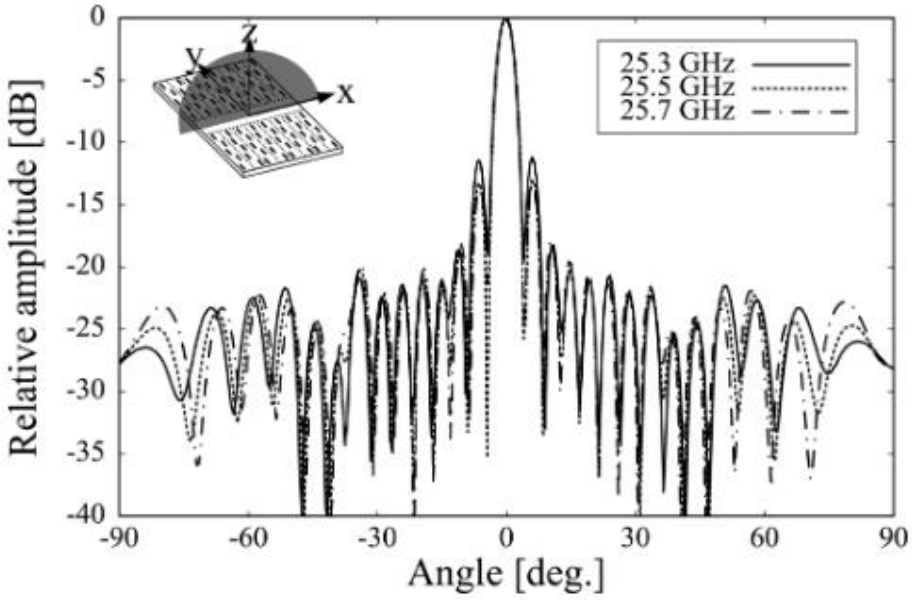

Fig.1.4. beam direction is independent with frequency by center-fed configuration [20]. *Copyright © 2006, IEEE*

1.3 Target and motivation

Two possible methods are proposed to realize uniform power radiation from each slot of a linear slotted waveguide. One is using slotted waveguide with variable offset, where slots with increasing offset towards the end of a waveguide can compensate the power loss. This design is concise, however the strong reflection and large radiation sidelobes make it extremely low efficiency. Second is employing inductive stair on the side wall to eliminate reflection. According to the previous work, the device with conductive wall also has limit efficiency of 57%, which is mainly caused by two reasons [21]. First is the relatively large offset make distance between two adjacent diagonal slots larger than $\sqrt{2}$ times of free space wavelength, which in principle generate large side lobes in $\phi = 45$ degree plane to reduce the power in boresight direction of the beam. Second, the inductive wall result in phase delay of each radiating slot to affect the radiation pattern.

To address these issues, several waveguide structures has been proposed, including nonuniform and asymmetric ridge waveguides [22-27]. However, by considering the practical applications and volume fabrication, we wish to realize high-efficiency, low reflection slotted antenna design based on normal rectangular waveguide. And in the next section, we will detailed describe the proposal of this work and clarify the main two topics that we try to solve in this work: (1) to suppress reflection and (2) to eliminate the sidelobes at $\phi = 45$ degree plane.

1.4 Proposal

We mainly proposed two ideas in this work to obtain large aperture efficiency.

First, we proposed reflection canceling stair (RCS) to eliminate the reflection. One advantage of RCS is the reduced height towards the end of waveguide can compensate power loss. As a result, uniform slot offset is employed. Another merit is RCS results in negligible phase delay comparing to inductive walls.

Second, we propose to optimize the broad wall width of the waveguide. In 38 GHz bandwidth, standard WR-28(7.112 x 3.556 mm) waveguide is usually utilized. However, in terms of sidelobes reduce and slot offset reduce, we need to optimize the broad wall width.

1.5 Thesis outline

The remaining parts of the thesis is organized as follows. We derive the most fundamental theory of rectangular waveguide and slot radiation in chapter 2. Chapter 3 is introduction of calculation method [(finite element method (FEM)], simulation software (Femtet by Murata software Co. Ltd.) and the simulation method. Chapter 4 is the design of antenna, where we describe the design of feeding part (input aperture, feeding waveguide etc.), radiating part (RCS, broad wall width). Chapter 5 is fabrication and characterization of the device that designed in chapter 4. Chapter 6 discusses two further issues of the device: fabrication tolerance and propagation loss. Chapter 7 gives the conclusion and prospective work of the thesis.

1.6 References

[1] J. C. Maxwell, "A dynamical theory of the electromagnetic field," Philosophical Transactions of the Royal Society of London, vol. 155, pp. 459-512, 1865.

[2] L. C. Van Atta, "A history of early microwave antenna development," IEEE Antennas and Propagation Society Newsletter, vol. 23, no. 5, pp. 10-14, 1981.

[3] H. Sobol and K. Tomiyasu, "Milestones of microwaves," IEEE Transactions on Microwave Theory and Techniques, vol. 50, no. 3, pp. 594-611, 2002.

[4] S. R. Rengarajan, L. G. Josefsson, and R. S. Elliott, "Waveguide-fed slot antennas and arrays: A review," Electromagnetics, vol. 19, no. 1, pp. 3-22, 1999.

[5] W. H. Watson, "Resonant slots," Journal of the Institution of Electrical Engineers-Part IIIA: Radiolocation, vol. 93, no. 4, pp. 747-777, 1946.

[6] N. Marcuvitz, Waveguide handbook, Iet, 1951.

[7] A. F. Stevenson, "Theory of slots in rectangular wave□guides," Journal of Applied physics, vol. 19, no. 1, pp. 24-38, 1948.

[8] R. J. Stegen, "Slot radiators and arrays at X-band," Transactions of the IRE Professional Group on Antennas and Propagation, vol. 1, no. 1, pp. 62-84, 1952.

[9] A. Oliner, "The impedance properties of narrow radiating slots in the broad face of rectangular waveguide: Part I--Theory," IRE Transactions on Antennas and Propagation, vol. 5, no. 1, pp. 4-11, 1957.

[10] T. Vu Khac and C. Carson, "Impedance properties of a longitudinal slot antenna in the broad face of a rectangular waveguide," IEEE Transactions on Antennas and Propagation, vol. 21, no. 5, pp. 708-710, 1973.

[11] R. Elliott, "An improved design procedure for small arrays of shunt slots," IEEE Transactions on Antennas and Propagation, vol. 31, no. 1, pp. 48-53, 1983.

[12] N. Goto, "A waveguide-fed printed antenna," IEICE Tech. Rep., vol. AP89, no. 3, pp. 17-21, Apr. 1989.

[13] K. Sakakibara, J. Hirokawa, M. Ando, and N. Goto, "Single-layer slotted waveguide arrays for millimeter wave applications," IEICE Trans. Commun., vol. E79-B, no. 12, pp. 1765-1772, Dec. 1996.

[14] K. Sakakibara et al., "Alternating phase-fed waveguide slot arrays with a single-layer multiple-way power divider," IEEE Proc.-Microw. Antennas Propag., vol. 144, no. 6, pp. 425-430, Dec. 1997.

[15] Y. Kimura et al., "A low-cost and very compact wireless terminal integrated on the back of a waveguide planar array for 26 GHz band fixed wireless access (FWA) systems," IEEE Trans. on Antennas and Propag., vol. 53, no. 8, pp. 2456-2463, Aug. 2005.

[16] J. L. Volakis, Antenna engineering handbook, 4th ed. New York, USA: McGraw-Hill, 2007, pp. 202-253.

[17] K. Lomakin et al., "3D Printed Slotted Waveguide Array Antenna for Automotive Radar Applications in W-Band," in Proc. EuMC, Madrid, Spain, 2018, pp. 1409-1412.

[18] H. Zhang et al., "A Low-Profile Millimeter-Wave Circularly-Polarized Multilayer Waveguide Antenna Array for Satellite Communication Application," in Proc. EuCAP, Copenhagen, Denmark, 2020, pp. P2.057.

[19] I. Costa, S. Cerqueira, and D. Spadoti, "Dual-band slotted waveguide antenna array for adaptive mm-wave 5G networks," in proc. EUCAP, Paris, France, 2017, pp. 1322-1325.

[20] S. Park et al., "Center feed single layer slotted waveguide array," IEEE Trans. Antennas Propag., vol. 54, no. 5, pp.1474-1480, May 2006.

[21] Y. Tsunemitsu et al., "Reflection characteristics of center-feed single-layer waveguide arrays," IEICE Trans. Commun., vol. E88-B, no. 6, pp. 2313-2319, Jun. 2005.

[22] Y. Tsunemitsu et al., "Single-layer slotted waveguide array with reflection canceling stairs," in proc. IEEE AP-S Int. Symp., Albuquerque, USA, 2006. pp. 3149-3152.

[23] W. Liu and Y. Tsunemitsu, "The Slotted Waveguide Array Antenna with Reflection Canceling Stairs in Millimeter Waveband," in proc. EuCAP, Copenhagen, Denmark , 2020, pp. Poster-2-A10.

[24] W. Liu and Y. Tsunemitsu, "The Waveguide Slot Array Antenna in Millimeter Waveband using the Reflection Canceling Stairs for the Sidelobe Suppression," in proc. IEEE AP-S Int. Symp., Montreal, Canada, 2020, pp. 531-532.

[25] W. Liu and Y. Tsunemitsu, "A Single-Layer Center-Feed Slotted Antenna Array with Reflection Canceling Stairs in 38-GHz Waveband," in proc. EuCAP, Madrid, Spain, 2022.

[26] W. Liu and Y. Tsunemitsu, "Grating Sidelobe Suppression in Single-Layer Center-Feed Waveguide Antenna Array at 38 GHz," in proc. IEEE AP-S/URSI. 2022, pp. 1220-1221.

[27] W. Liu and Y. Tsunemitsu, "A Waveguide Slot Array Antenna With Reflection-Canceling Stairs for Sidelobes Suppression at 38 GHz," in IEEE Access, vol. 11, pp. 72942-72949, 2023. doi: 10.1109/ACCESS.2023.3294821

Chapter 2
Theory of slotted rectangular waveguide

This chapter theoretically analyzes slotted rectangular waveguide to clarify the underlying mechanism. We first demonstrate the wave propagation in the rectangular waveguide starting from the most fundamental Maxwell equations. Then we also present the radiation physics of a narrow rectangular slot on the broad wall of a rectangular waveguide along longitude direction. Critical concepts derived from this chapter are essential guidelines for the following design and simulation work.

2.1 Electromagnetic wave propagation in rectangular waveguide

In this section, we derive the analytic solution of Helmholtz equation under the boundary condition of rectangular waveguide. We can assume the wave is propagating inside lossless material (ϵ, μ) while the boundary is perfect conductor boundary. The configuration of a rectangular waveguide is shown in Figure 2.1, where the broad width and narrow width are a and b respectively.

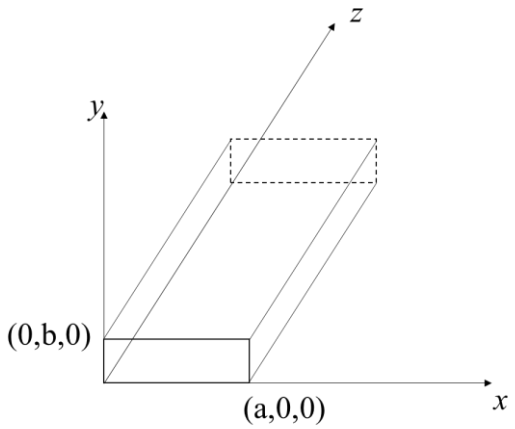

Figure 2.1. The configuration of rectangular waveguide.

Starting from the normal Maxwell equations and using the conditions that no free charges and conducting current existence in the lossless material (ϵ, μ). Consequently, the Maxwell equations can be written as follows:

$$\nabla \cdot \boldsymbol{D} = 0 \tag{2.1.1}$$

$$\nabla \cdot \boldsymbol{B} = 0 \tag{2.1.2}$$

$$\nabla \times \boldsymbol{H} = \frac{\partial \boldsymbol{D}}{\partial t} \tag{2.1.3}$$

$$\nabla \times \boldsymbol{E} = -\frac{\partial \boldsymbol{B}}{\partial t} \tag{2.1.4}$$

Notice that although the following operations are carried out on the electric field $\boldsymbol{E}$, similar operation can be done by using magnetic field $\boldsymbol{H}$. First, by using the vector calculation formula (2.2)

$$\nabla \times \nabla \times \boldsymbol{E} = \nabla(\nabla \cdot \boldsymbol{E}) - \nabla^2 \boldsymbol{E} \tag{2.2}$$

and calculating the curl of (2.1.4), we can obtain:

$$\nabla \times \nabla \times \boldsymbol{E} = \nabla(\nabla \cdot \boldsymbol{E}) - \nabla^2 \boldsymbol{E} = -\epsilon\mu \frac{\partial^2}{\partial t^2} \boldsymbol{E} \tag{2.3}$$

Since there is no free charges and the wave propagating inside isotropic, $\nabla \cdot \boldsymbol{E} = 0$. Thus, we obtain the following wave equation:

$$\nabla^2 \boldsymbol{E} - \epsilon\mu \frac{\partial^2}{\partial t^2} \boldsymbol{E} = \boldsymbol{0} \tag{2.4}$$

To treat the equation (2.4) with D'Alambertian transformation:

$$\xi = z + \frac{t}{\sqrt{\epsilon\mu}} \tag{2.5.1}$$

$$\eta = z - \frac{ct}{\sqrt{\epsilon\mu}} \tag{2.5.2}$$

$$\frac{\partial}{\partial \xi} = \frac{\partial}{\partial z} + \sqrt{\epsilon\mu}\frac{\partial}{\partial t} \tag{2.5.3}$$

$$\frac{\partial}{\partial \eta} = \frac{\partial}{\partial z} - \sqrt{\epsilon\mu}\frac{\partial}{\partial t} \tag{2.5.4}$$

$$\left(\frac{\partial}{\partial z} + \sqrt{\epsilon\mu}\frac{\partial}{\partial t}\right)\left(\frac{\partial}{\partial z} - \sqrt{\epsilon\mu}\frac{\partial}{\partial t}\right)\boldsymbol{E} = \frac{\partial^2 \boldsymbol{E}}{\partial \xi \partial \eta} = \mathbf{0} \tag{2.5.5}$$

We find two facts from the D'Alambertian transformation of wave function. First, the solution of (2.4) can be expressed as arbitrary linear combination of two vector functions $\boldsymbol{f}(\xi)$ and $\boldsymbol{g}(\eta)$. Second, the solution can be recognized as combination of two waves with opposite directions, and the propagation speed is:

$$c = \frac{1}{\sqrt{\epsilon\mu}} \tag{2.6}$$

From the analysis above, we know the propagation nature of electromagnetic wave and derive the propagation speed. However, it is hard to determine the distribution of electric and magnetic field by just the wave equation. Thus, in the following part, we derive the wave mode in a rectangular waveguide. Generally, respective part that contains time and space variable is separable:

$$\boldsymbol{E}(\boldsymbol{r}, t) = \boldsymbol{E}(\boldsymbol{r}) \cdot T(t) \tag{2.7}$$

By substituting (2.7) into wave equation we obtain:

$$\frac{c^2\nabla^2\boldsymbol{E}(\boldsymbol{r})}{\boldsymbol{E}(\boldsymbol{r})} = \frac{T(t)''}{T(t)} \tag{2.8}$$

Equation (2.8) is always true if and only if both LHS and RHS equals to a constant number α. Since the light is oscillation will not vanish in the lossless material, the constant α should be negative number, therefor we obtain:

$$T'' - \alpha T = 0, \alpha < 0 \tag{2.9}$$

As a result, we find the wave oscillation in time domain is obey the following equation:

$$T = Asin(\sqrt{-\alpha}t + \theta) \tag{2.10}$$

where A and θ can be determined by the initial conditions. Especially, when we treat the case of monochromatic wave, the parameter α can be determined by the angular frequency:

$$\alpha = -\omega^2 \tag{2.11}$$

In the space domain, we obtain Helmholtz equation as follows:

$$(\nabla^2 + k^2)\boldsymbol{E}(\boldsymbol{r}) = 0 \tag{2.12}$$

Here we consider a monochromatic wave, whose wave number is:

$$k^2 = \frac{\omega^2}{\mu\varepsilon} = k_x^2 + k_y^2 + k_z^2 \tag{2.13}$$

Next, we continue to carry out variable separation as follows:

$$E_i(x, y, z) = X(x) \cdot Y(y) \cdot Z(z), i = x\ , y\ or\ z \tag{2.14}$$

$$\frac{1}{X} \cdot \frac{d^2X}{dx^2} + \frac{1}{Y} \cdot \frac{d^2Y}{dy^2} + \frac{1}{Z} \cdot \frac{d^2Z}{dz^2} = -k^2 \tag{2.15}$$

As Figure 2.1 shown, the wave is propagating along z direction, while standing at x-y plane. That is to say, to determine the mode is to determine the wave number in x and y direction for a rectangular waveguide. The respective mode of x and y direction can be derived from the following equations:

$$\frac{d^2X}{dx^2} + k_x^2 \cdot X = 0 \tag{2.16.1}$$

$$\frac{d^2Y}{dy^2} + k_y^2 \cdot Y = 0 \tag{2.16.2}$$

Consequently: following equations are derived.

$$X = Asin(k_x \cdot x) + Bcos(k_x \cdot x) \tag{2.17.1}$$

$$Y = Csin(k_y \cdot y) + Dcos(k_y \cdot y) \tag{2.17.2}$$

And combining the wave propagation nature in z direction:

$$Z = E \cdot e^{-jk_z \cdot Z} \tag{2.18}$$

We next to determine the mode by the following boundary conditions:

First, all electromagnetic problem follows the following boundary conditions:

$$E_{1t} = E_{2t} \tag{2.19}$$

Especially for TE mode:

$$E_z = 0 \tag{2.20}$$

By considering the tangential component is zero (2.1.4, 2.19 and 2.20) at boundary, we obtain the TE mode as follows:

$$E_x \propto \cos\left(\frac{m\pi}{a}x\right) \cdot \sin\left(\frac{n\pi}{b}y\right) \cdot e^{-jk_z \cdot z} \tag{2.21.1}$$

$$E_y \propto \sin\left(\frac{m\pi}{a}x\right) \cdot \cos\left(\frac{n\pi}{b}y\right) \cdot e^{-jk_z \cdot z} \tag{2.21.2}$$

$$E_z = 0 \tag{2.21.3}$$

$$H_x \propto \sin\left(\frac{m\pi}{a}x\right) \cdot \cos\left(\frac{n\pi}{b}y\right) \cdot e^{-jk_z \cdot z} \tag{2.21.4}$$

$$H_y \propto \cos\left(\frac{m\pi}{a}x\right) \cdot \sin\left(\frac{n\pi}{b}y\right) \cdot e^{-jk_z \cdot z} \tag{2.21.5}$$

$$H_z \propto \cos\left(\frac{m\pi}{a}x\right) \cdot \cos\left(\frac{n\pi}{b}y\right) \cdot e^{-jk_z \cdot z} \tag{2.21.6}$$

The amplitude of each component is trivial, in the case of steady-state sinusoidal situation, one can easily derive them from the Maxwell equations. Thus, the mode T_{mn} is determined as follows:

$$k_x = \frac{m\pi}{a}, m = 0,1,2,3 \ldots \tag{2.22.1}$$

$$k_y = \frac{n\pi}{b}, n = 0,1,2,3 \ldots \tag{2.22.2}$$

where m and n can not be zero simultaneously.

As shown in Figure 2.1, the broad wall width a is larger than the narrow wall width b, thus the mode with longest wavelength (cutoff wavelength), which was allowed to propagate through the waveguide, is TE_{10}:

$$\lambda_{c,10} = \frac{2\pi}{\sqrt{\left(\frac{m\pi}{a}\right)^2 + \left(\frac{n\pi}{b}\right)^2}} = 2a \tag{2.23}$$

Similarly, we can obtain the secondary mode wavelength:

$$\lambda_{20} = a \tag{2.24.1}$$

$$\lambda_{01} = 2b \tag{2.24.2}$$

As a result, we find the essential single mode condition for a rectangular waveguide:

$$\lambda < 2a \; and \; \lambda > max(2b, a) \tag{2.25}$$

For standard WR-28 waveguide, $a = 7.112\ mm, b = 3.556\ mm$, the single mode condition is:

$$a < \lambda < 2a \tag{2.26}$$

Next, we derive the propagation constant k_z:

$$k_z = \sqrt{k^2 - k_x^2 - k_y^2} \tag{2.27}$$

As a result, we can define the wavelength in the waveguide (λ_g) to clarify the resonant property along z direction:

$$\lambda_g = \frac{2\pi}{k_z} = \frac{2\pi}{\sqrt{k^2 - \left(\frac{m\pi}{a}\right)^2 - \left(\frac{n\pi}{2b}\right)^2}}, m = 1, n = 0 \tag{2.28}$$

By considering equation (2.6 and 2.13), we obtain the following equation:

$$\lambda_g = \frac{\lambda}{\sqrt{1 - \left(\frac{\lambda}{2a}\right)^2}} \tag{2.29}$$

Usually, the radiating slot distributes along z direction has a gap of $\frac{1}{2}\lambda_g$ to minimize the mutual coupling among each other.

2.2 Radiating from slot

We derive the radiation pattern of a slot along longitudinal direction of waveguide in frequency domain. For simplicity and practical applications, instead of using Fourier transform, all the following operations are carried out on the case of steady-state electromagnetic (EO) field under sinusoidal excitations. Consequently, the electric and magnetic fields are written as following:

$$\boldsymbol{E}(\boldsymbol{r},t) = \boldsymbol{E}(\boldsymbol{r}) \cdot e^{[j(\omega t - \boldsymbol{k}\boldsymbol{r})]} \tag{2.30.1}$$

$$\boldsymbol{H}(\boldsymbol{r},t) = \boldsymbol{H}(\boldsymbol{r}) \cdot e^{[j(\omega t - \boldsymbol{k}\boldsymbol{r})]} \tag{2.30.2}$$

Thus, the differential operator can be replaced by:

$$\frac{\partial}{\partial t} = j\omega \tag{2.31.1}$$

$$\nabla = -j\boldsymbol{k} \tag{2.31.2}$$

In addition, we assume the wave is propagating inside isotropic material:

$$\mathbf{D} = \epsilon \boldsymbol{E} \tag{2.32.1}$$

$$\boldsymbol{B} = \mu \boldsymbol{H} \tag{2.32.2}$$

$$\boldsymbol{J} = \sigma \boldsymbol{E} \tag{2.32.3}$$

where $\boldsymbol{D}$, $\boldsymbol{E}$, $\boldsymbol{B}$, $\boldsymbol{H}$, $\boldsymbol{J}$, ϵ, μ, σ denote electric displacement density, electric field, magnetic flux density, magnetic field, current density, permittivity, permeability and electric conductivity, respectively.

As a result, the Maxwell equation is presented in the following format, where 4 equations are all related to the electric or magnetic field:

$$\nabla \cdot \mathbf{E} = \frac{\rho}{\epsilon} \tag{2.33.1}$$

$$\nabla \cdot \frac{\mathbf{B}}{\mu} = \nabla \cdot \boldsymbol{H} = 0 \tag{2.33.2}$$

$$\nabla \times \boldsymbol{H} = (\sigma + j\omega\epsilon)\boldsymbol{E} \tag{2.33.3}$$

$$\nabla \times E = -j\omega\mu\boldsymbol{H} \tag{2.33.4}$$

Since (2.33.2) is valid in whole space, which means nonexistence of magnetic monopole, the magnetic field can be expressed by a curl of vector:

$$\boldsymbol{B} = \mu\boldsymbol{H} = \nabla \times \mathbf{A} \tag{2.34}$$

Here we call $\boldsymbol{A}$ the magnetic vector potential. And from the equation (2.33.4) and (2.34), we obtain:

$$\nabla \times (\mathrm{j}\omega\boldsymbol{A} + \boldsymbol{E}) = 0 \tag{2.35}$$

Due to the curl of a gradient of any scalar function is zero, the electric field can be express by magnetic vector potential $\boldsymbol{A}$ and electric scalar potential $\boldsymbol{\phi}$ as follows:

$$\boldsymbol{E} = -j\omega\boldsymbol{A} - \nabla\boldsymbol{\phi} \tag{2.36}$$

By eliminating $\boldsymbol{E}$ and $\boldsymbol{H}$ of (2.3.3) by using (2.34) and (2.36), we obtain:

$$\nabla \times \boldsymbol{H} = \frac{1}{\mu}\nabla \times \nabla \times \boldsymbol{A} = (\sigma + j\omega\epsilon)(-j\omega\boldsymbol{A} - \nabla\phi) \tag{2.37}$$

Using the following vector calculation formula (2.2) and Lorentz gauge:

$$\nabla \cdot \boldsymbol{A} = -j\omega\mu\epsilon\phi \tag{2.38}$$

We can obtain the vector Helmholtz equation:

$$\nabla^2\boldsymbol{A} + k^2\boldsymbol{A} = -\mu\boldsymbol{J} \tag{2.39}$$

By performing divergence operation on equation (2.36), we obtain the scalar Helmholtz equation:

$$\nabla^2\phi + k^2\phi = -\frac{\rho}{\epsilon} \tag{2.40}$$

Where $k = \omega\sqrt{\mu\epsilon}$ denotes the wavenumber.

According to the boundary condition, the solution of (2.39) presents the possible electric and magnetic field distribution in the specific region, such as rectangular, round or any type of waveguide (we usually call this mode). Normally it is impossible to analytically solve the (2.39), unless the boundary is very simple and symmetric. However, numerical solution is always possible, thus we can express the electric field by the following equation through the magnetic vector potential $\boldsymbol{A}$:

$$\boldsymbol{E} = -\mathrm{j}\omega\mathbf{A} + \nabla \cdot \frac{\nabla \cdot \boldsymbol{A}}{j\omega\mu\epsilon} \tag{2.41}$$

Next, we consider the retarded vector potential of a current source. Since the wave propagating speed is finite, the observer, even near the source, can't immediately detect the information of the source, due to a retardation of $t - \frac{r}{c}$. As a result, the magnetic vector potential of field point $\boldsymbol{r}$ can be presented by the following Biot-Savart Law from the current source point $\boldsymbol{r'}$. [Notice that we use $\boldsymbol{r}$, x, y and z denote the field point and $\boldsymbol{r'}$, x', y' and z' denote the source point in the following entire dissertation. While the relative position is shown in Figure 2.2.]

$$\boldsymbol{A} = \frac{\mu}{4\pi} \iiint \frac{\boldsymbol{J}(\boldsymbol{r'}, t - |\boldsymbol{r} - \boldsymbol{r'}|/c)}{|\boldsymbol{r} - \boldsymbol{r'}|} dv \tag{2.42}$$

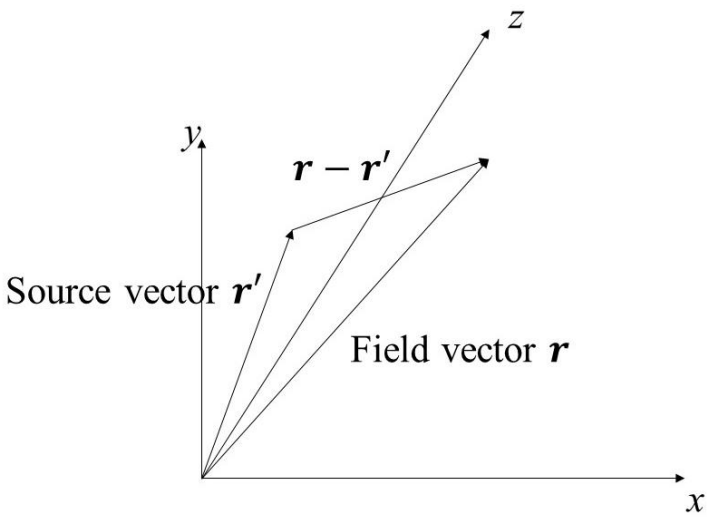

Fig. 2.2. The source point and field point

The relative position can be expanded as following:

$$|\boldsymbol{r}-\boldsymbol{r}'| = \mathrm{r}\cdot\sqrt{1-2\frac{\hat{\boldsymbol{r}}\cdot\boldsymbol{r}'}{r}+\left(\frac{r'}{r}\right)^2} = r\cdot\{1+\left(\frac{r'}{r}\right)(\hat{\boldsymbol{r}}\cdot\widehat{\boldsymbol{r}'})\ldots\ldots\} \tag{2.43}$$

Normally, to take the following approximation is sufficient, since we interest in the area of $r' \ll r$:

$$|\boldsymbol{r}-\boldsymbol{r}'| \approx \mathrm{r} \tag{2.44}$$

As a result, the retarded vector potential becomes:

$$\boldsymbol{A} = \frac{\mu}{4\pi r}\iiint \boldsymbol{J}(\boldsymbol{r}', t-|\boldsymbol{r}-\boldsymbol{r}'|/c)dv' \tag{2.45}$$

Thus, in frequency domain, the retarded vector potential can be obtained from Fourier transform:

$$\boldsymbol{A}_{\boldsymbol{\omega}} = \frac{\mu}{4\pi}\cdot\frac{e^{ikr}}{r}\iiint \boldsymbol{J}(\boldsymbol{r}', \omega)\cdot e^{-i\boldsymbol{k}\cdot\boldsymbol{r}'}\, dv' \tag{2.46}$$

Next, we can calculate the retarded vector potential of a narrow rectangular slot by using dipole model as Figure 2.3.

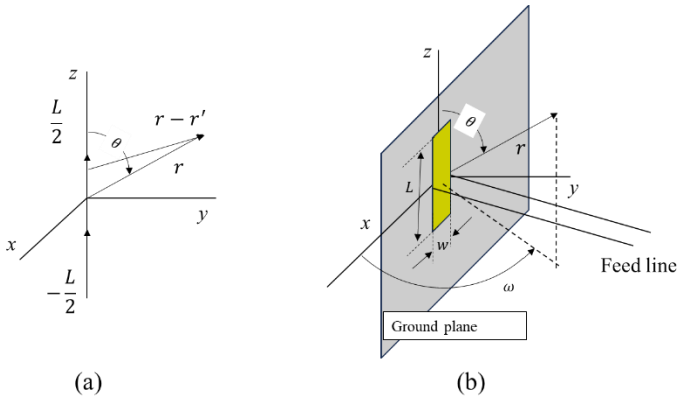

Figure 2.3. (a) Current distribution of a dipole antenna

(b) configuration of a narrow rectangular slot

The current distribution can be presented by:

$$I = I_m \sin[k(L - |z|)] \tag{2.47}$$

Besides:

$$\boldsymbol{J}dv = Idz \tag{2.48.1}$$

$$\boldsymbol{k} \cdot \boldsymbol{r'} = cos\theta \tag{2.48.2}$$

Therefor the magnetic vector potential of far field (where $r' \ll r$) generated from a dipole antenna can be written as：

$$\boldsymbol{A}_\omega = \frac{\mu I_m}{4\pi} \cdot \frac{e^{ikr}}{r} \int_{-L}^{L} \sin[\mathrm{k(L} - \mathrm{|z|)}] e^{-ikzcos\theta} dz \tag{2.49}$$

The integral operation method can be found in Appendix I, and the result is following:

$$\boldsymbol{A}_{\omega} = \frac{\mu I_m}{2\pi} \cdot \frac{e^{ikr}}{kr} [\frac{\cos(kLcos\theta) - \cos(kL)}{\sin^2 \theta}] \tag{2.50}$$

By expanding the following items into first order:

$$\cos(kLcos\theta) - \cos(kL) = 1 - \frac{(kLcos\theta)^2}{2} - \left[1 - \frac{(kL)^2}{2}\right] = \frac{1}{2} k^2 L^2 \sin^2 \theta \tag{2.51}$$

And considering the following relation:

$$\boldsymbol{E}_{\theta} = j\omega\mu \cdot sin\theta \cdot \boldsymbol{A}_{\omega} \tag{2.52}$$

We finally obtain the following radiation approximation relation in the far field region:

$$\boldsymbol{E}_{\theta} \approx sin\theta \tag{2.53}$$

2.3 Summary

We have briefly introduced the physic fundaments of the propagation nature of electromagnetic wave in rectangular waveguide and the radiation nature of a narrow rectangular slot along longitude direction. All the equations are derived from four basic Maxwell equations. In general, the following 4 equations (2.23, 2.25, 2.29 and 2.53) are essential for the next work.

First, the cutoff wavelength is determined by (2.23), which means that the wavelength longer than this value is invalid to propagating into the rectangular waveguide:

$$\lambda_{c,10} = 2a \tag{2.23}$$

Second, the rectangular waveguide size to determine the single mode condition are given by (2.25):

$$\lambda < 2a \; and \; \lambda > max(2b, a) \tag{2.25}$$

Third, the wavelength inside the rectangular waveguide is determined by (2.29):

$$\lambda_g = \frac{\lambda}{\sqrt{1 - \left(\frac{\lambda}{2a}\right)^2}} \tag{2.29}$$

Finally, the far-field radiation pattern of a narrow slot can be approximately written as (2.53):

$$\boldsymbol{E}_\theta \approx sin\theta \tag{2.53}$$

(Notice: related basic knowledges can be found in several textbook of slotted antenna array.)

2.4 References

[1] L. Josefsson and P. Persson, Conformal Array Antenna Theory and Design. John Wiley & Sons, 2006.

[2] C. A. Balanis, Antenna Theory: Analysis and Design. John Wiley & Sons, 2016.

[3] A. Lakhtakia, V. K. Varadan, and V. V. Varadan, Time-Harmonic Electromagnetic Fields in Chiral Media. Berlin: Springer, 1989.

[4] W. L. Stutzman and G. A. Thiele, Antenna Theory and Design. John Wiley & Sons, 2012.

[5] A. Zangwill, Modern Electrodynamics. Cambridge University Press, 2013.

[6] J. D. Jackson, "Classical Electrodynamics," 1999.

Chapter 3
Simulation method

3.1 Brief introduction of Finite element method

To solve the Helmholtz equation with normal boundary condition is analytically impossible unless some simple and symmetric conditions, such as infinite planer waveguide (slab waveguide), rectangular waveguide [see Chapter 2], cylindrical or spherically symmetric waveguide [the result can be analytically represented with the support of Bessel function for cylindrical case and Legendre function for spherical case respectively]. For a practical case, such as slotted waveguide arrayed antennas with multiple slots, effective algorism to obtain an approximation solution is essential since there is no analytical solution.

First, we consider a differential equation:

$$\mathcal{D}\phi = f \tag{3.1}$$

where $\mathcal{D}$ is the differential operator, ϕ is the function required to be solved, and f is inhomogeneous impulse function (external field), respectively. Notice that the boundary condition of (3.1) is normally a combination of Neumann and Dirichlet condition [idea conductor $\rho = 0$], impedance boundary condition [$\rho \neq 0$], Sommerfeld condition, and multiple complex higher order boundary condition. As a result, even (3.1) has simple format, there is no analytical solution due to the complicated boundary condition. Next, we introduce two approaches to obtain approximation solution of (3.1).

First, Rayleigh-Ritz method are introduced as follows. We first introduce the dot product of functions:

$$[\phi, \chi] = \int_{\Omega} \phi \chi^* d\Omega \tag{3.2}$$

The Differential operator $\boldsymbol{\mathcal{D}}$ is self-adjoint if

$$[\boldsymbol{\mathcal{D}}\phi, \chi] \;=\; [\phi, \boldsymbol{\mathcal{D}}\chi] \tag{3.3}$$

The Differential operator $\boldsymbol{\mathcal{D}}$ is positive definite if

$$[\boldsymbol{\mathcal{D}}\phi, \phi] \;\geq 0 \; and \; [\boldsymbol{\mathcal{D}}\phi, \phi] = 0, only \; if \; \phi = 0 \tag{3.4}$$

According to functional theory (variational method), for a self-adjoint and positive-definite differential operator, the solution of (3.1) can be solved by calculating the minimal value of following equation [1]:

$$F(\tilde{\phi}\,) = \frac{1}{2}\left[\mathcal{D}\tilde{\phi}, \tilde{\phi}\right] - \frac{1}{2}[\tilde{\phi}, f] - \frac{1}{2}[f, \tilde{\phi}] \tag{3.5}$$

where $\tilde{\phi}$ is trial function.

Next critical technology is to expand the trial function as follow:

$$\tilde{\phi} = \sum_i c_i v_i = [c]^t[v] = [v]^t[c]\,, i = 1,2,3 \ldots . finite \; number \; n \tag{3.6}$$

where c_i is undetermined coefficients and v_i is function basis for expansion.

By substituting (3.6) into (3.5), we obtain

$$F = \frac{1}{2}[c]^t \int_\Omega [v]\boldsymbol{\mathcal{D}}[v]^t d\Omega[\mathrm{c}] - [c]^t \int_\Omega [v] f d\Omega \tag{3.7}$$

The solution of (3.1) can be obtained by solving following system of linear equations. the minimal value of F in (3.7) can be obtained when we take the partial derivative:

$$\frac{\partial F}{\partial c_i} = \frac{1}{2}\int_\Omega v_i \boldsymbol{\mathcal{D}}[v] d\Omega[\mathrm{c}] + \frac{1}{2}[c]^t \int_\Omega v\boldsymbol{\mathcal{D}}v_i d\Omega + - \int_\Omega v_i f d\Omega = 0 \tag{3.8}$$

By combining all the components ($i = 1,23, \ldots n$) of Equation (3.8) together, we get the following n dimensional linear equations system:

$$[S][c] = [b] \tag{3.9}$$

where

$$S_{ij} = \int_{\Omega} v_i \mathcal{D} v_j d\Omega \tag{3.10.1}$$

$$b_i = \int_{\Omega} v_i f d\Omega \tag{3.10.2}$$

From the explanation above, we find the fact that to solve (3.1) is to solve a n dimensional linear equations system. Proper selection of the function basis $[v]$ determine the error value between the exact and trial solution. Apparently, the above Rayleigh-Ritz method is impact in terms of theory. Because the method has clarified that to solve differential equation is to solve linear equations system, which is obtained by discretizing the original equation. Besides, the precision of the solution by Rayleigh-Ritz method is determined by the function basis selection. We know the dimension of (3.9) is equal to the capacity of basis *n*. However, to select proper basis (function type and number of basis *n*) is difficult work. First, it is obvious that by selecting complete basis we can obtain exact solution. On the other hand, only incomplete basis is existing for general problem. In addition, to increasing the numbers of basis is not effective way because it will increase the calculation load [dense linear equations have time complexity with $O(n^3)$]. Besides, the increasing of capacity of basis *n* will not increase the precision of solution if the function type is inappropriate.

To solve the drawbacks of Rayleigh-Ritz method, we will introduce the following Galerkin method with subdomain configuration.

First, we define the residual *r* as follow:

$$r = \boldsymbol{\mathcal{D}}\tilde{\phi} - f \neq 0 \tag{3.11}$$

Then we define the residual weighting integral as follows:

$$R_i = \int_{\Omega} w_i r d\Omega \tag{3.12}$$

where w_i denotes the weighting and optimal trial solution $\tilde{\phi}$ leads that $R_i = 0$.

Next, we determine the trial function by subdomain configuration. As we describe in Rayleigh-Ritz method, the most difficult and essential procedure is to determine the trial function, while basis expansion method has fatal flaw for a practical issue. The difficulty is to determine the trial function at entire domain. For this reason, we first divide the entire domain into small grids. And in each small grid Ω_i, the trial function can be treated as polynomial function $\sum_i a_i x^i$. Usually, to take constant or linear function as trail function for subdomain is enough. One can also increase the precision by decreasing the grid size or increase the power of polynomial function we used for each subdomain.

Following, we derive the linear equations system of original differential function (3.1) by Galerkin method with subdomain configuration.

First step is to discrete the domain Ω as series of Ω^e $(e = 1,2,3 \ldots M)$. Normal subdomains (grid types) used for every dimension are illustrated in Figure 3.1.

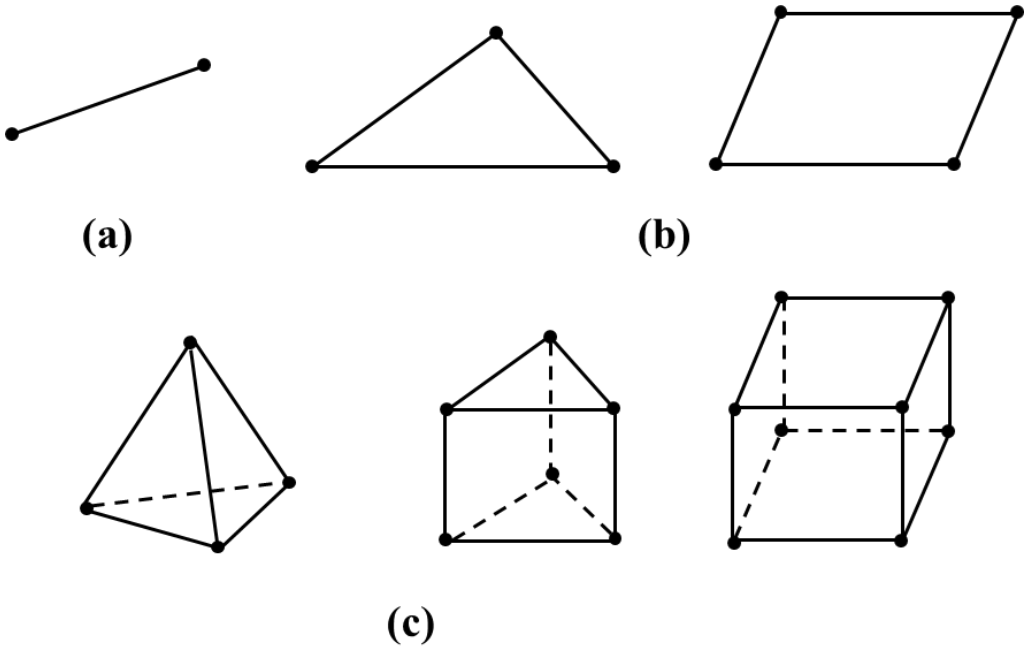

Fig. 3.1. The normal subdomain used for (a) 1-dimension (b) 2-dimensional and (c) 3-dimension.

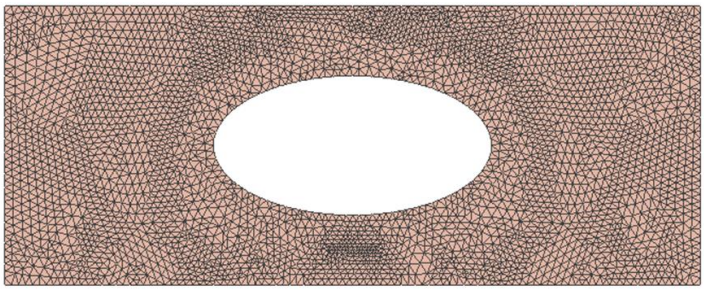

(a)

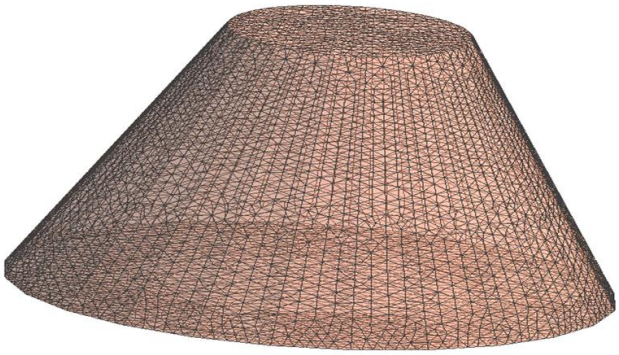

(b)

Fig. 3.2. The example of domain discretion for (a) 2 dimension and (b) 3 dimension.

The trial function in subdomain can be represented by the combination of the value in the nodes of the section:

$$\tilde{\phi}^e = \sum_{j=1}^{n} N_j^e \phi_j^e = [N^e]^t[\phi^e] = [\phi^e]^t[N^e] \tag{3.13}$$

Thus the residual weighting integral is:

$$[R] = \sum_{e=1}^{M} ([K^e][\phi^e] - [b^e]) \tag{3.14}$$

When we take the residual as 0, we obtain the linear equations system with the following matrix format:

$$[K^e][\phi^e] = [b^e] \tag{3.15}$$

where [K] is NxN matrix, $[\phi]$ and $[b]$ are N x 1 vectors, each component of K and b can represent as:

$$K_{ij}^e = \int_{\Omega^e} N_i^e \boldsymbol{D} N_j^e d\Omega \tag{3.16.1}$$

$$b_i^e = \int_{\Omega^e} f N_i^e d\Omega \tag{3.16.2}$$

Totally, there is NxM linear functions.

Final task is to solve a large dimension linear equations system as follow:

$$A\bar{x} = \bar{b}\,, where\ A \in R^n \times R^n \tag{3.17}$$

The traditional method such as Gaussian elimination method has a time complexity of $O(n^3)$. According to the process that we obtain (3.17), the matrix is almost empty. As a result, we can use the famous Crout decomposition (LU decomposition) method to increase the solving speed. We try to decompose the coefficient matrix as follow:

$$A = LU \tag{3.18}$$

where L is lower triangular matrix, while U is upper triangular matrix.

By the Crout decomposition, the original problem is converted as follow:

$$Ly = b \tag{3.19.1}$$

$$Ux = y \tag{3.19.2}$$

Notice that the solution of (3.19.1) and (3.19.2) is fast:

$$y_1 = \frac{b_1}{l_{11}} \tag{3.20.1}$$

$$y_i = \frac{1}{l_{ii}}\left(b_i - \sum_{k=1}^{i-1} l_{ik} y_k\right), i > 1 \tag{3.20.2}$$

By substituting (3.20) into (3.19.2), we can obtain:

$$x_n = \frac{y_n}{l_{nn}} \tag{3.21.2}$$

$$x_i = \frac{1}{u_{ii}}\left(y_i - \sum_{k=i+1}^{n} u_{ik} x_k\right)\ i < n \tag{3.21.2}$$

In addition, we use the following equations to explain why LU decomposition is suitable for FEM. Notice that by Galerkin method, we obtain a sparse matrix. As shown in follow, many elements in matrix is 0 that the decomposition is fast:

$$A = [a_{ij}] = \begin{bmatrix} l_{11} & \cdots & 0 \\ \vdots & \ddots & \vdots \\ l_{n1} & \cdots & l_{nn} \end{bmatrix} \begin{bmatrix} u_{11} & \cdots & u_{1n} \\ \vdots & \ddots & \vdots \\ 0 & \cdots & u_{nn} \end{bmatrix} \tag{3.22}$$

We can obtain n^2 equations with $n^2 + n$ variable. As a result, we can choose any n variable as arbitrary value and then to calculate the remaining n^2 parameters.

Normally, if we choose all the diagonal elements of U (u_{ii}) as 1, then the remaining elements of L and U is easy to be calculated.

3.2 Brief introduction of Femtet

First is the overview of Femtet. Femtet stands out in the crowded field of simulation software due to its unique capabilities and user-friendly interface. Developed by Murata Software, a company with a strong reputation for innovation in the software industry, Femtet is designed to meet the complex simulation needs of professionals across different engineering disciplines.

Next, we introduce several Key features of this software:

1. Multiphysics Simulation:
   Femtet excels in multiphysics simulations, allowing users to seamlessly integrate and simulate various physical phenomena within a single environment. This capability is crucial for projects where different aspects of a system interact and influence each other.
2. Electromagnetic Analysis:
   The software provides advanced tools for electromagnetic analysis, making it an invaluable resource for engineers working on projects related to electric motors, sensors, antennas, and other devices where electromagnetic interactions are critical.

3. Thermal Analysis:
   Engineers dealing with thermal management challenges find Femtet particularly useful. The software enables detailed thermal analysis, helping to optimize designs for heat dissipation, thermal conductivity, and other thermal-related factors.

4. Structural Mechanics:
   Femtet offers robust tools for structural mechanics simulations. This includes stress analysis, deformation studies, and assessments of structural integrity, essential for industries ranging from aerospace to civil engineering.

5. Fluid Dynamics:
   Fluid dynamics simulations are a forte of Femtet, making it a valuable asset for projects involving the flow of liquids or gases. Applications include aerodynamics, HVAC system design, and fluid-structure interaction studies.

6. User-Friendly Interface:
   One of the standout features of Femtet is its user-friendly interface. The software is designed to be accessible to both seasoned simulation experts and those new to the field. The intuitive interface allows users to set up simulations efficiently and interpret results with ease.

7. Versatility in Material Modeling:
   Femtet supports a wide range of material models, allowing engineers to accurately represent the behavior of different materials under various conditions. This flexibility is essential for achieving realistic and reliable simulation results.

Femtet finds applications in diverse industries, including:

1. Electronics: For analyzing electromagnetic compatibility, designing sensors, and optimizing electronic components.

2. Automotive: In the development of electric vehicles, optimizing thermal management systems, and analyzing structural components for safety and durability.

3. Aerospace: For aerodynamic studies, structural analysis of components, and thermal management in spacecraft.

4. Energy: In the design and optimization of renewable energy systems, such as wind turbines and solar panels.

5. Mechanical Engineering: For simulating stress and strain in mechanical components, optimizing designs for strength and durability.

6. Biomedical Engineering: In the study of electromagnetic interactions in medical devices and the thermal analysis of equipment used in healthcare.

3.3 Harmonic analysis by Femtet

There are 3 kinds of solvers in Femtet for Electromagnetic problems. For low frequency cases [Constant Current/Voltage (AC) up to 1 MHz], Femtet provides electric and magnetic solver. For the frequency range from 1 MHz to several tens of Giga-Hertz bandwidth, we can use electromagnetic wave solver as shown in Figure 3.3.

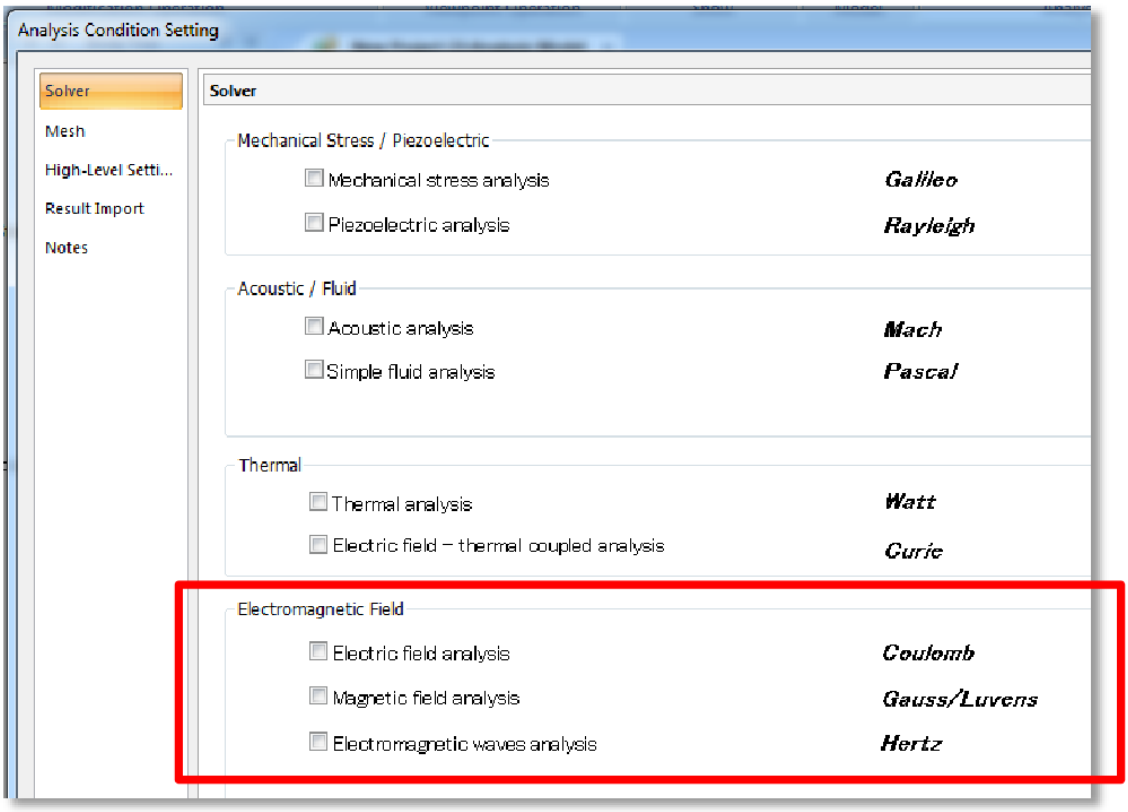

Fig. 3.3. The interface of Femtet to select proper solver.

Besides, there are also three different analyses for the electromagnetic solver. For wave propagation problems with 3D structure, we should use harmonic analysis. By using harmonic analysis, we obtain the electromagnetic wave in the space, the S parameters, the directivity and the surrounding field. Figure 3.4 is the procedure of harmonic analysis by Femtet.

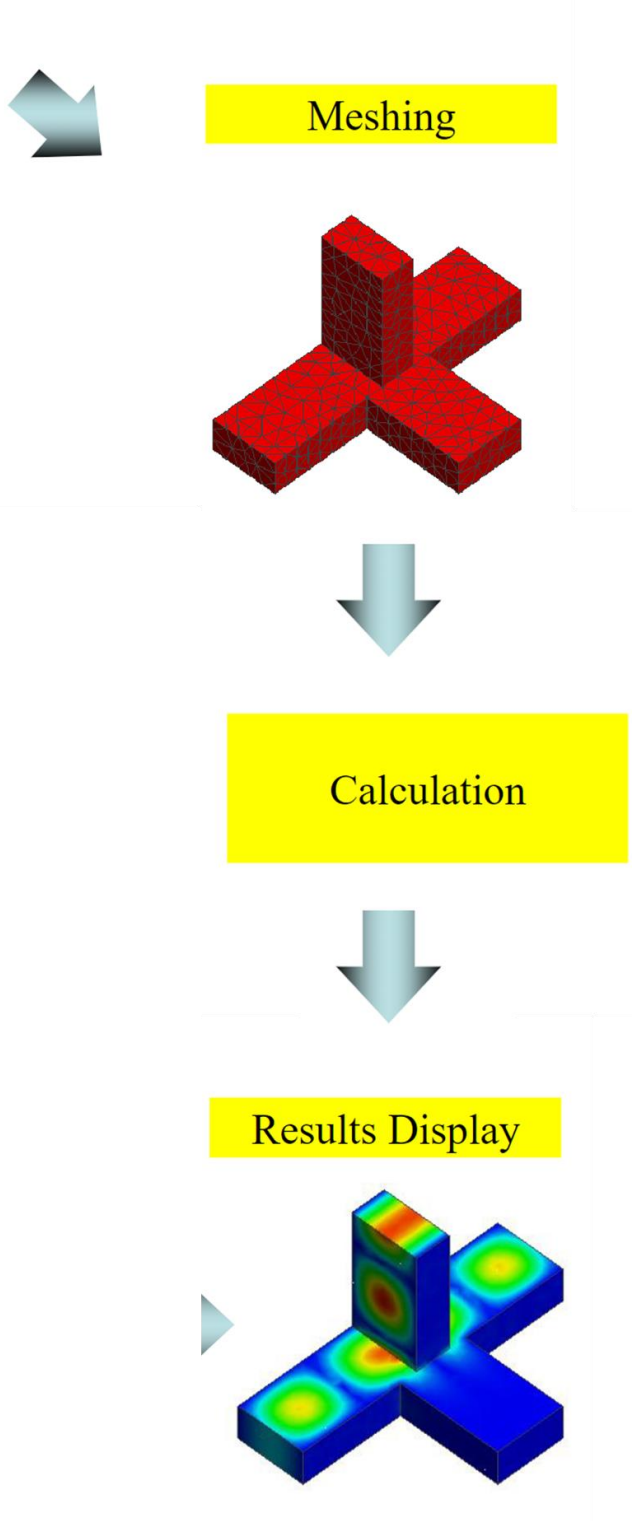

Fig. 3.4. The harmonic analysis process.

3.4 Summary

Chapter 3 is a pivotal segment offering a detailed exploration of the Finite Element Method (FEM) and the specialized simulation software, Femtet, focusing on its application in high-frequency electromagnetic wave analysis through harmonic analysis.

3.1 is introduction to FEM. The chapter commences with a comprehensive introduction to the Finite Element Method (FEM), an indispensable numerical approach for solving complex engineering challenges. FEM's fundamental principles are laid out, illustrating its versatility in problem-solving by discretizing structures into manageable elements. This section underscores the adaptability of FEM across diverse engineering domains, underscoring its efficacy in structural mechanics, thermal analysis, and electromagnetic simulations.

3.2 is introduction to Femtet. Building on the FEM foundation, Section 3.2 provides an in-depth overview of Femtet, a robust simulation software developed by Murata Software. The discussion underscores Femtet's user-friendly interface and its ability to handle multiphysics simulations with finesse. Noteworthy is Femtet's prowess in electromagnetic analysis, thermal simulations, and structural mechanics, positioning it as a versatile solution applicable across a spectrum of engineering disciplines.

3.3 is introduction to Harmonic Analysis in Femtet for High-Frequency Electromagnetic Wave Simulation:

A focal point of the chapter, Section 3.3 introduces the application of Femtet in simulating high-frequency electromagnetic waves through harmonic analysis. Harmonic analysis, explained as a technique for studying system behavior under sinusoidal excitations, is particularly relevant in high-frequency scenarios. The section elucidates the core principles of harmonic analysis and demonstrates how Femtet streamlines precise and efficient simulations. Femtet's role in providing insights into electromagnetic compatibility, antenna design, and other high-frequency wave scenarios is underscored.

Finally, we make a conclusion of this chapter as follows.

Chapter 3 serves as a comprehensive guide to both the theoretical underpinnings of FEM and the practical application of Femtet. The emphasis on harmonic analysis within Femtet positions it as an invaluable tool for engineers and researchers navigating the intricacies of high-frequency electromagnetic wave simulations. As technology progresses, users are encouraged to refer to the latest documentation from Murata Software for updates, advanced features, and real-world applications of Femtet in the dynamic field of electromagnetic analysis.

3.5 References

[1] J.-M. Jin, "The finite element method in electromagnetics," John Wiley & Sons, 2015.

[2] C. A. J. Fletcher and C. A. J. Fletcher, "Computational galerkin methods," Springer Berlin Heidelberg, 1984.

[3] A. S. Vander Vorst, A. A. Laloux, and R. J. M. Govaerts, "A computer optimization of the Rayleigh-Ritz method," IEEE Transactions on Microwave Theory and Techniques, vol. 17, no. 8, pp. 454-460, 1969.

[4] Widowati, et al., "Analysis of Crout, Lu, Cholesky Decomposition, and QR Factorization: A Case Study On The Relationship Between Abiotic (Carbon and Nitrogen) and Biotic (Macrobenthos Diversity) Factors," Waste Technology (WasTech), 2014, pp. 56-62.

[5] N. Li, Y. Saad, and E. Chow, "Crout versions of ILU for general sparse matrices," SIAM Journal on Scientific Computing, vol. 25, no. 2, pp. 716-728, 2003.

Chapter 4
Design of slotted waveguide array antenna

4.1 Introduction of the device

Figure 4.1 shows the configuration of an alternating phase-fed single-layer waveguide slot array antenna with 10×10 slots. The design frequency is set to 38 GHz. The input aperture consists of a standard WR-28 waveguide [See Figure 4.1]. To facilitate fabrication and increase the manufacturing yield rate, the three parts of the antenna can be individually fabricated and connected with bolts. This modular design allows for easier assembly and adjustment.

In the input aperture part, a matching waveguide with a 1/4 guided wavelength is employed, along with a feed waveguide located between the input aperture (WR-28) and the 3 dB power divider for reflection suppression. The feed waveguide utilizes an alternative-phase configuration, wherein adjacent waveguides have a 180-degree phase difference and a uniform amplitude distribution. This arrangement effectively cancels the current on the side walls, eliminating the need for electrical connection between the top radiating plate and the waveguide-based layer.

Furthermore, each feeding aperture incorporates an inductive sidewall to enhance feeding efficiency by precisely tuning the amplitude and phase of the TE10 wave. To achieve a high gain, RCSs are employed for each slot on the radiating waveguides. The radiation section of the antenna features slots spaced at intervals of 1/2 guided wavelength along the longitude direction to mitigate the mutual coupling effect.

To design and estimate the structure, full-wave calculations were performed using the finite element method (FEM). We utilized Femtet (Murata Software Co., Ltd.) as the electromagnetic simulation tool, which accounts for various factors including mutual coupling effects and material loss with high accuracy.

The remaining part of this chapter is organized as follows: we first introduce the design of Broad wall width, radiating part and feeding part respectively in subsection 4.2, 4.3 and 4.4. Sub section 4.5 presents the numerical analysis result of the device. ww then summarize this chapter in sub-section 4.6.

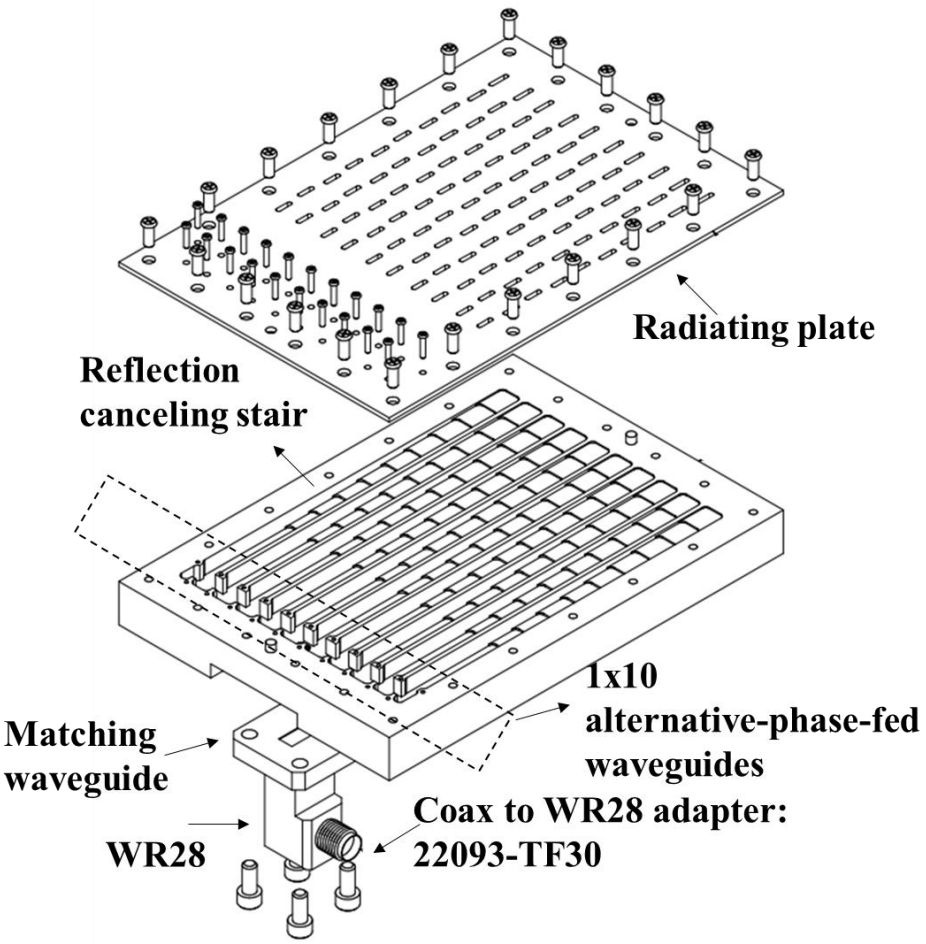

Fig. 4.1. Configuration of a single-layer 10x10 alternative phase-fed slotted waveguide array antenna.

4.2 Broad-wall width design for side-lobe suppression

Figure 4.2 illustrates a 2-dimensional slotted array pattern. For simplicity, we fixed the width of a single waveguide as a and the offset as $r \cdot a$, where $0 < r < 0.5$ to ensure the offset at range of $[0,\frac{a}{2}]$. In the y-direction, the slots are allocated at a distance of half the wavelength in the waveguide. The wavelength of the radiating waveguide depends on the waveguide width a.

The relationship between the wavelength in free space (λ) and the wavelength in the waveguide (λ_g) can be calculated using the following equation:

$$\lambda_g = 2b = \frac{\lambda}{\sqrt{1-\left(\frac{\lambda}{2a}\right)^2}} \tag{4.1}$$

where b is the longitude distance between two adjacent slots.

By considering each slot as a small electric dipole antenna with an identical radiating amplitude and ignoring the mutual coupling effect, we can write the antenna factor as:

$$AF(\theta,\phi) = \sum_m e^{jkX_m \sin\theta\cos\phi} \sum_n e^{jkY_n \sin\theta\sin\phi} \tag{4.2}$$

Here, k represents the wave number in free space. The positions of each slot can be determined using the following formulas:

$$X_{2n} = \left(n - \frac{1}{2} + r\right) \cdot a, n = 1,2,3 \ldots\ldots \tag{4.3}$$

$$X_{2n+1} = \left(n + \frac{1}{2} - r\right) \cdot a, n = 0,1,2 \ldots\ldots \tag{4.4}$$

$$Y_n = \left(n - \frac{1}{2}\right) \cdot b, n = 1,2,3 \ldots\ldots \tag{4.5}$$

The grating lobe is mainly generated from two aspects. First, grating lobes are produced when adjacent slots are separated by distances greater than $\sqrt{2}\lambda$. Second, an asymmetrical slot distribution with multiple radiating centers also generates grating lobes. Thus, we can qualitatively conclude that obtaining low-sidelobe antenna arrays requires compact and symmetric slot distributions.

In Figure 4.3(a), the optimization results for minimizing the slot distance $|O_1O_2|$ are presented. For the standard WR-28 (7.112x3.556 mm) waveguide, an offset of 1.38 mm is required to achieve 10% radiation. However, the designed waveguide (5x3.556 mm) only needs an offset of 0.28 mm to achieve the same radiating amount. Consequently, by reducing the broad wall width to 5 mm, smaller distances between adjacent slots and a symmetric configuration (smaller offset) are achieved.

Using equation (4.2), the corresponding antenna factor is calculated, and the radiation pattern in the ϕ=45° plane between the two waveguides is plotted in Figure 4.3(b). It is observed that the waveguide with a broad wall width of 5 mm exhibits lower sidelobes.

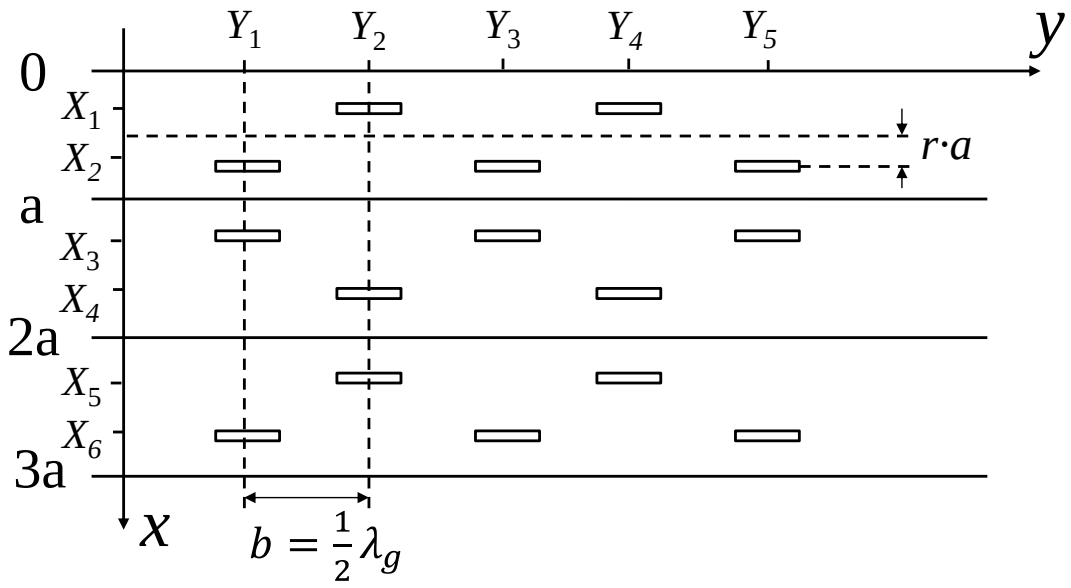

Fig. 4.2. Top view of arrayed antenna in X-Y plane. Broad wall width is a. Offset of slot is r · a, where 0<r<0.5. The slot can be represented by its coordinate (X_n, Y_n).

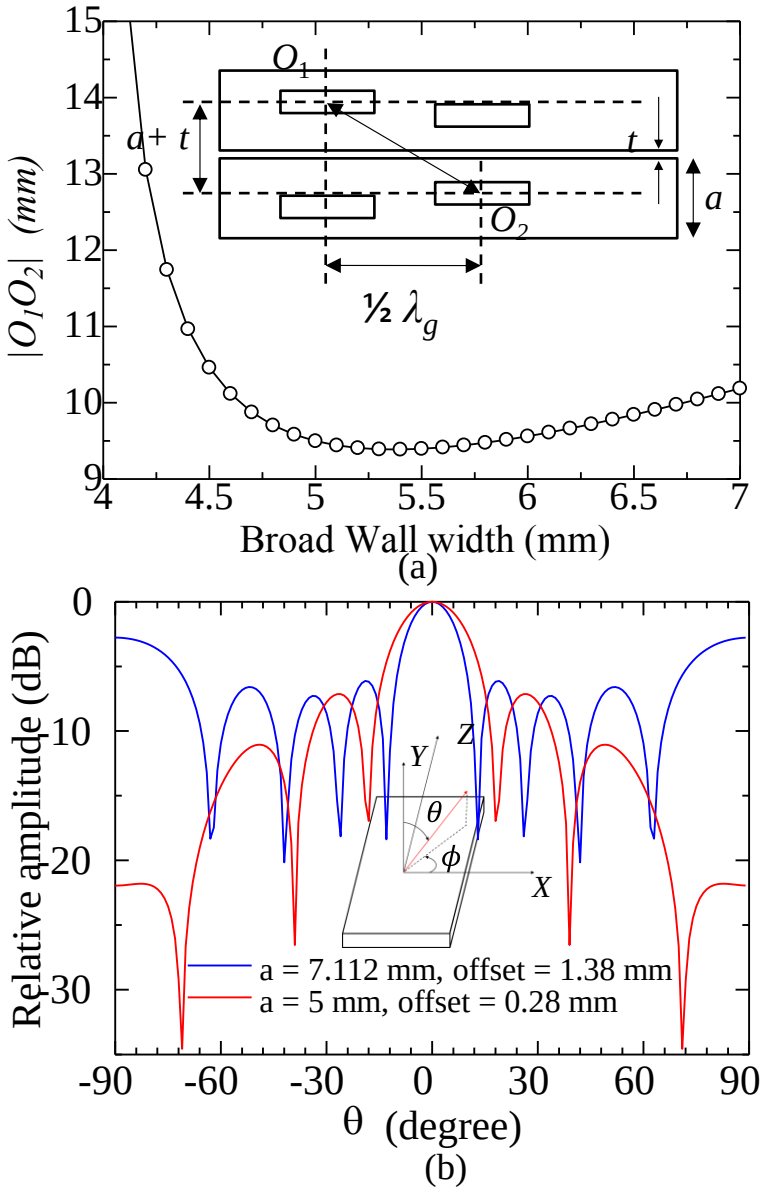

Fig. 4.3. (a) $|O_1O_2|$ as a function of Broad wall width a. (b) Radiation pattern at Phi = 45-degree plane. Red line shows result with 5 mm broad wall and blue line shows result with 7.112 mm broad wall.

4.3 Radiating part design (reflection-canceling stair)

Reflection-canceling stairs (RCS) is proposed by Y. Tsunemitsu in 2007 [1]. The configuration is shown in Figure 4.4. There are mainly 3 merits for slotted waveguide with RCS. First, effective reflection suppression is achieved when the reflection from the slot and corresponding stair has equal amplitude and alternative phase. Second, the waveguide with stair has smaller phase delay comparing to an inductive side wall for reflection cancellation. Third, the decreasing of waveguide height towards the end of the waveguide can compensate for the electromagnetic power loss because the power density is increased with the reduction of height.

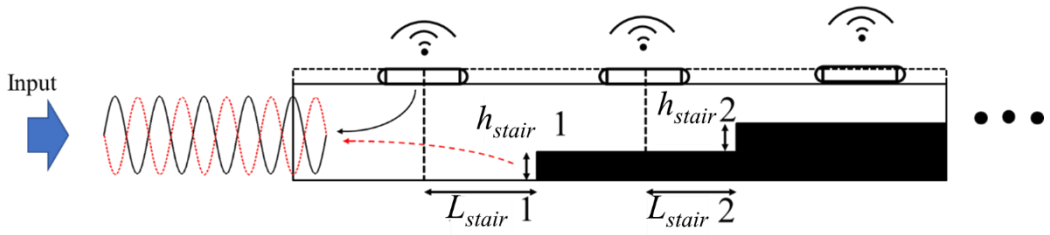

Fig. 4.4. Configuration of slotted waveguide with RCS.

We can use normalized impedance to evaluate the phase delay or advance by the relation between complex S11 and normalized impedance. According to the transmission line theory, the reflection on a transmission line is occurred due to the impedance mismatch between the characteristic impedance and the load impedance. Especially, when the load impedance is zero (short) or infinity (open), the respective current or voltage will be reflected 100%, where the |S11| = 0dB. The following equation (4.6) illustrates the relation among complex reflection S11, the characteristic impedance and the load impedance:

$$S_{11} = \frac{Z_L - Z_0}{Z_L + Z_o} = \frac{Z_{norm} - 1}{Z_{norm} + 1} \tag{4.6}$$

Where Z_L, Z_0 and Z_{norm} are the load impedance, the characteristic impedance, and the normalized impedance respectively. In addition, the following equation derives the real and imaginary part of normalized impedance as:

$$Re(Z_{norm}) = \frac{1 - Re^2 - Im^2}{(1 - Re)^2 + Im^2} \tag{4.7.1}$$

$$Im(Z_{norm}) = \frac{2Im}{(1 - Re)^2 + Im^2} \tag{4.7.1}$$

where the complex S11 can be denoted as:

$$S_{11} = Re + jIm, j = \sqrt{-1} \tag{4.8}$$

By using FEM, we obtain the reflection of a rectangular waveguide with only one slot (*Lo* = 0.28 mm, *Ls* = 3.88 mm, a = 5 mm, h = 3.556 mm). The result is S11= -0.103+0.0218j. By substituting the S11 into equation (4.7.1) and (4.7.2), we can obtain the normalized impedance $Z_{norm} = 0.812 + 0.036j\ \Omega$, where the positive imaginary part shows that the rectangular waveguide with only slot has an inductive property, which results in phase delay. To this end, the traditional inductive reflection canceling components (such as side walls, metal cylinders) are unsuitable for slotted waveguide. Following we introduce the design procedure of slotted waveguide with capacitive reflection canceling components.

Ten identical waveguides form a 10 × 10 antenna array, with each waveguide containing a linear slot allocation. The slot distribution on adjacent waveguides follows a mirror-symmetric pattern, creating an alternative-phase-fed configuration. In order to achieve a uniform radiating amount and minimize reflection for each slot, we employed a RCS for each radiating slot, as depicted in Figure 4.5. We used a 3-D finite element method (FEM) calculation to determine the complex S parameters for the model shown in Figure 4.5. Due to the inherent challenges in directly calculating the radiating power from a slot, we adopt an alternative approach. By evaluating the reflection coefficient (S11), transmission coefficient (S21), and propagation loss within the waveguide, we can indirectly estimate the radiation from the slot using the following equation:

$$Radiation = 1 - |S11|^2 - |S21|^2 - Loss \tag{4.9}$$

In our design process, we sequentially design 10 units from the input side to the end of waveguide, where each unit consists of a radiating slot and a RCS. The design of each unit utilizes the model shown in Figure 4.5 and undergoes full-wave FEM simulation. By specifying the waveguide height (*h*), slot length (*L*s), slot offset (*L*o), height of the RCS (*h*stair), and length of the RCS (*L*stair), we calculate the reflection coefficient (S11) and the radiation from the slot. We begin by setting the slot offset to 0.28mm. Subsequently, the waveguide height of each unit is determined based on the height and *h*stair of the preceding unit. In this manner, we establish a cascading effect in the design process. By conducting parameter scanning of *L*s, *h*stair, and *L*stair, our objective is to attain the desired radiation level while simultaneously minimizing the reflection coefficient S11.

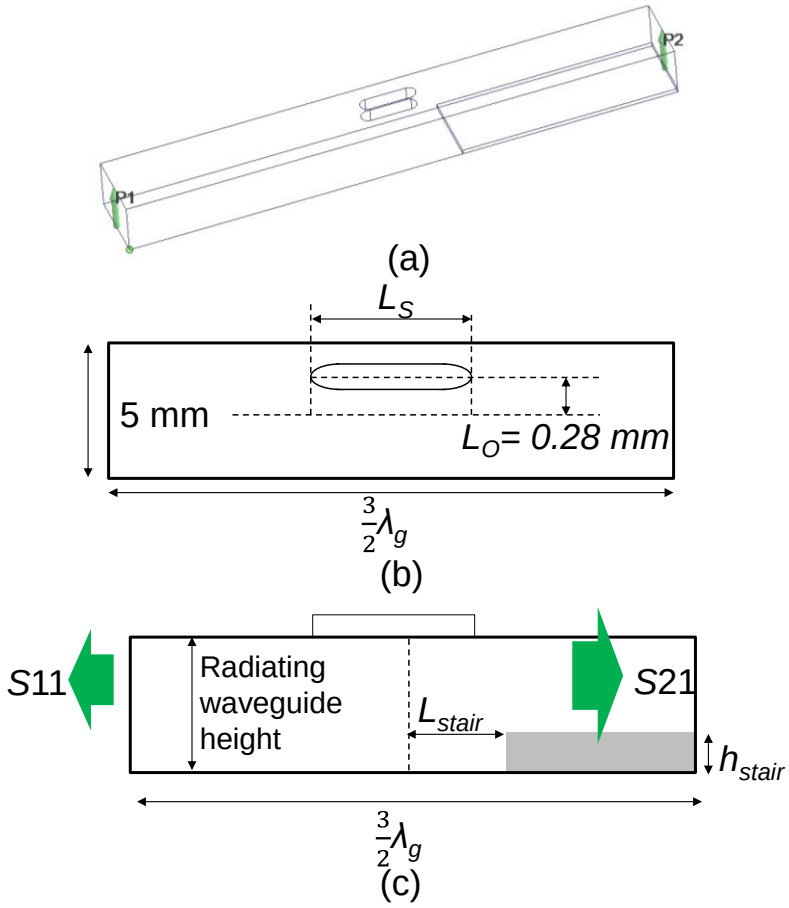

Fig. 4.5. (a) The 3D schematic of a radiating slot with reflection canceling stair. (b) The configuration of slot, where the slot length is Ls and the slot offset is Lo. For all slots, we keep the width as 1 mm and the offset Lo as 0.28 mm. (c) The configuration of reflection canceling stair, where we define the stair height as hstair and the distance to the slot center as Lstair.

Although the recent commercial software (Femtet in this work) has incredible ability to treat 3-D FEM calculation, it is still nontrivial to determine all parameters of one unit. Because there are four parameters (slot offset and slot length for slot, while the length and position of stair) in total. As a result, to brute-force sweep the parameter space is low efficient. n^4 times calculation is required to just determine n different design. Consequently, we try to independently design the slot and stair and slight adjust the structure finally. This method will extremely reduce the design time.

The detailed design of a unit (slot and stair) is shown as follows. The work on the designed waveguide with broad wall of 5-mm is carried out. We will give all the parameters of two types of design slotted waveguide in the final of this section.

First, we can roughly determine the slot parameters without considering the influence of stair. We can choose the parameters (*Lo, Ls*) = (0.28 mm, 3.88 mm) according to the 2-dimensioanl swept result as shown in Figure 4.6. The increasing trend of radiation amount is from the right-down side to the left-up side, which means that small slot offset and large slot length results in large radiation amount. For intuitiveness, we plot the radiation difference from 10% as a function of different slot offset and slot length.

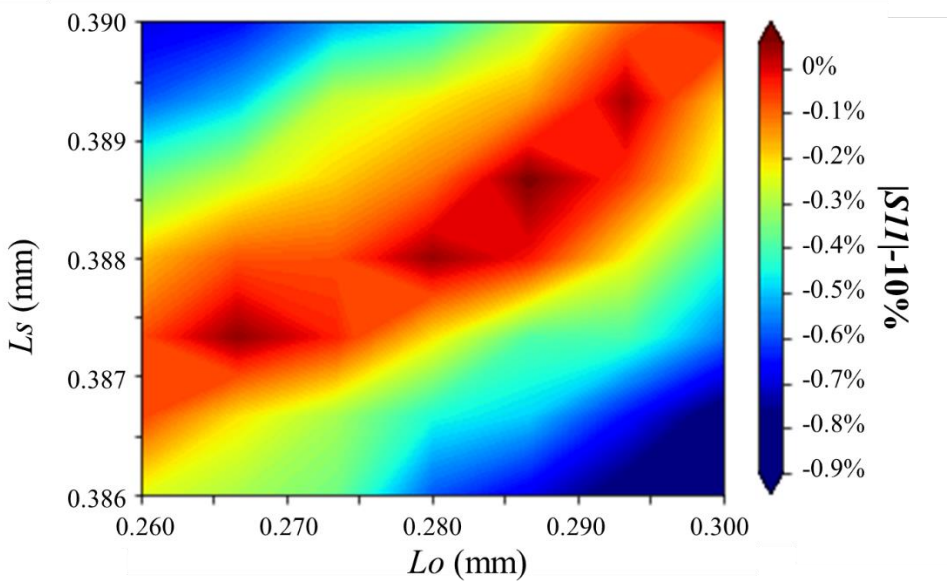

Fig. 4.6. The slot length and the offset versus radiation power. (a = 5 mm)

After we determine the slot deign, we can determine the height of the stair, by calculating the S11 parameter. We assume that the amplitude of stair reflection is mainly determined by its height instead of the length. As shown in Figure 4.7(a), we can determine roughly the stair height. In addition, the Smith chart in Figure 4.7(b) shows that the stair has capacitive property which can compensate the phase delay that caused by slot.

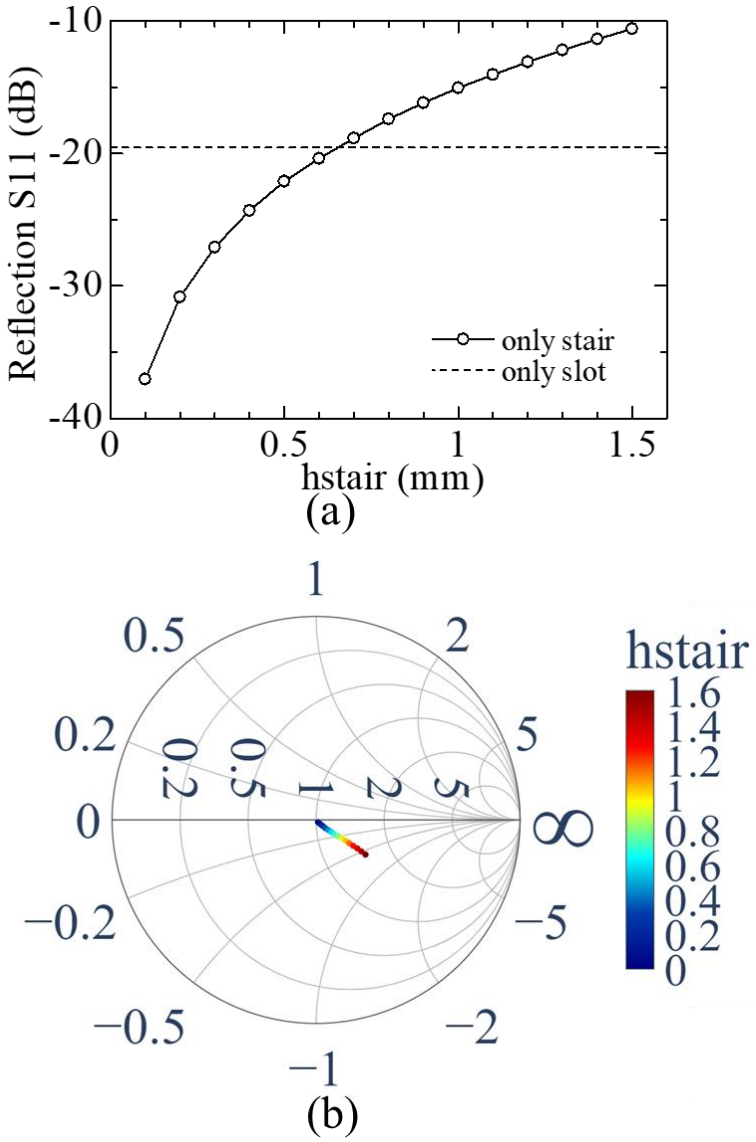

Fig. 4.7. (a) The amplitude of S11 and (b) Smith chart to illustrate the reflection characteristics of slotted waveguide with reflection canceling stair versus different stair height.

Next, we sweep the lstair to tuning the phase of reflection wave from the stair. As shown in Figure 4.8, we obtain an extremely low reflection combination of slot and stair. The position of step only affects the phase of reflection that we can see the reflectance of the unit with slot and step (dot curve) has both larger (in phase) and smaller (out phase) region than it of the unit with only slot (dashed line). Figure 4.8 shows reflectance less than -47 dB is obtained with Lstair = 4.18mm. We then carry out a comparison among the novel unit, the unit with only step and the unit with only step in Figure 4.8. Strong reflection canceling effect of proposed unit is confirmed that less than -40 dB |S11| is obtained near 38 GHz. Smith chart in Figure 4.8(b) shows the normalized impedance as a function of Lstair. For a proper Lstair, the capacity of the reflection canceling stair can totally compensate the inductance of slot, where extremely small reflection is obtained. Consequently, the second unit with slot and stair is designed by same procedure.

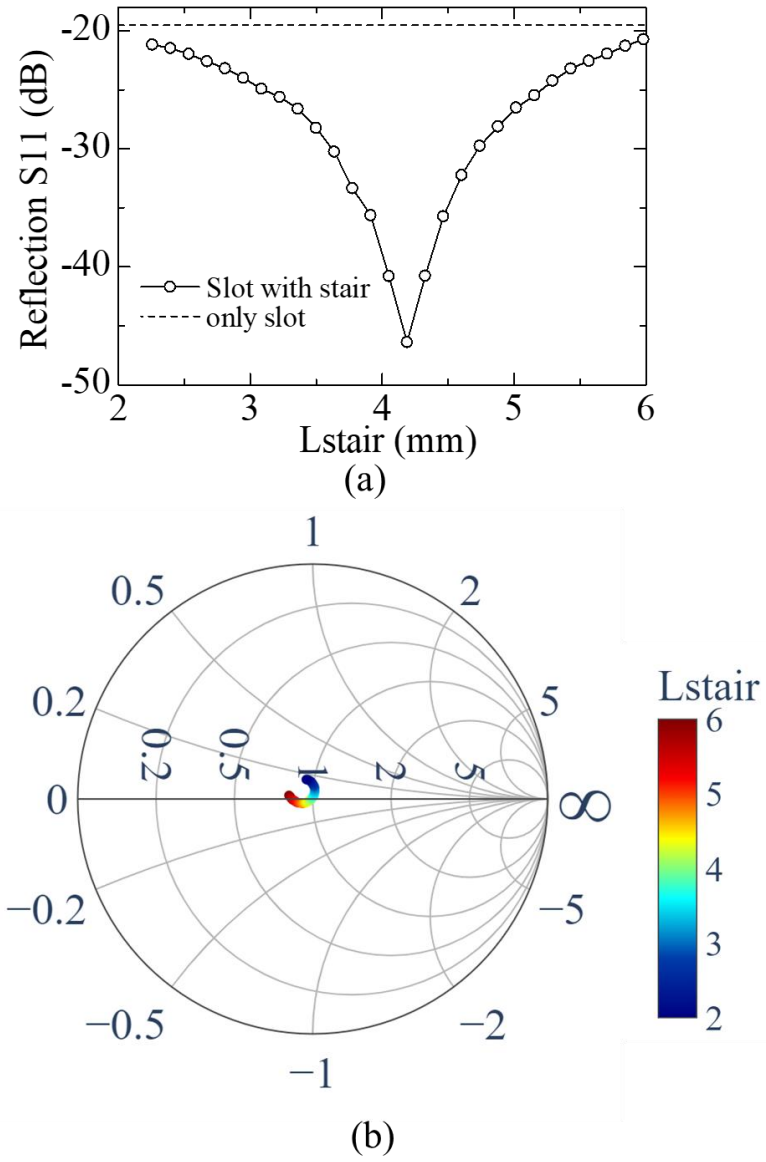

Fig 4.8. (a) The amplitude of S11 and (b) Smith chart to illustrate the reflection characteristics of unit with slot and stair versus Lstair.

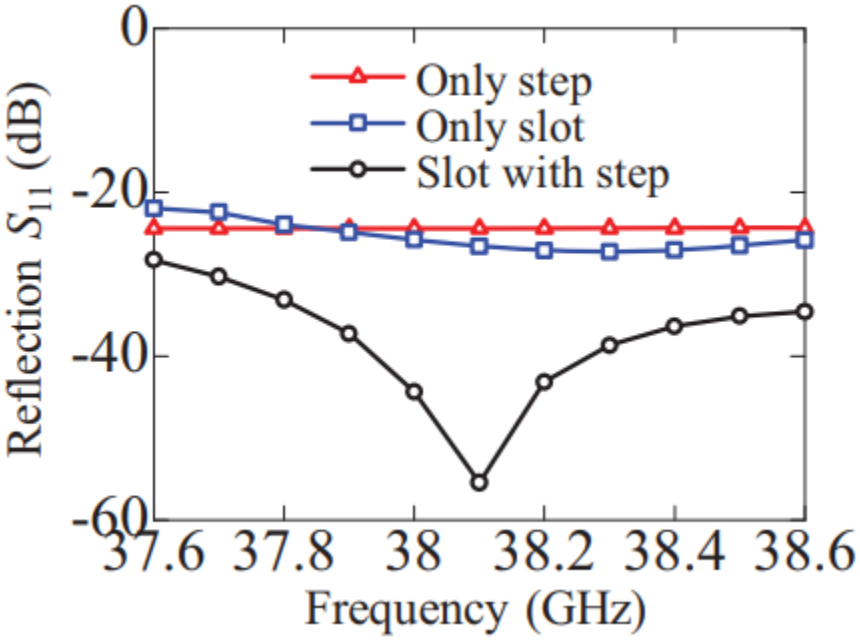

Fig 4.9. The reflection characteristics of three different units.

After we roughly determine the approximate value of design of a unit (slot and stair), we continue to optimize it by combining both the slot and stair together. The reflection from an appropriately designed RCS has an equal amplitude and reverse phase to the slot reflection, effectively suppressing the total reflection [see Figure 4.10(a)]. Consequently, with the antenna parameters specified in Table I, we obtained uniform amplitude and less than -30 dB |S11| for each slot [see Figure 4.10(b)].

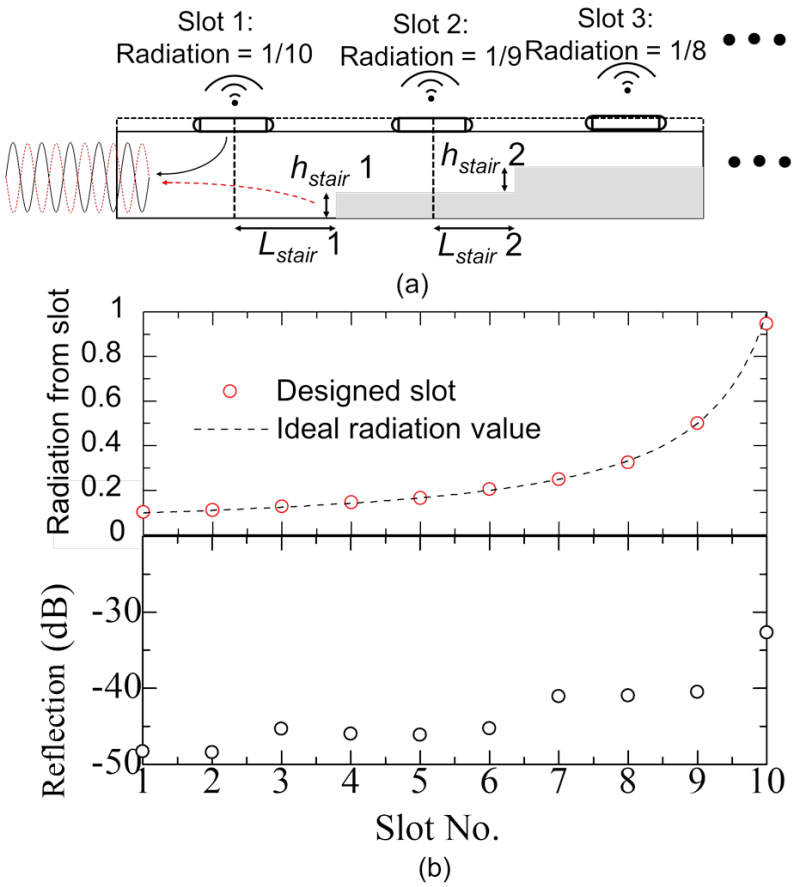

Fig. 4.10. (a) configuration of reflection canceling stairs, h_{stair} and L_{stair} denotes the height and position of reflection stair. (b) The radiation and reflection (S11) of each unit (slot and stair) at 38 GHz.

TABLE I
THE PARAMETERS OF THE RADIATING UNIT

Unit	Ls (mm)	Lstair (mm)	hstair (mm)
1	3.88	4.16	0.41
2	3.96	3.96	0.39
3	4.04	3.96	0.39
4	4.08	3.96	0.39
5	4.12	3.96	0.39
6	4.14	3.66	0.33
7	4.19	3.66	0.33
8	4.27	3.66	0.33
9	4.41	3.46	0.30
10	4.80	3.21	0.296

(Broad wall width = 5mm, slot offset = 0.28 mm)

We also give the design results of another three types of slotted waveguide for the further numerical analysis comparison in section 4.6. Parameters of slotted waveguide with 5-mm broad wall width and no RCS is listed in Table II. While parameters of standard WR-28 (7.112x3.556 mm) slotted waveguide with and without RCS are listed in Table III and IV, respectively.

TABLE II

THE PARAMETERS OF THE RADIATING UNIT

Unit	Ls (mm)	Lo(mm)
1	3.88	0.30
2	3.84	0.31
3	3.88	0.34
4	3.86	0.36
5	3.84	0.42
6	3.86	0.47
7	3.87	0.57
8	3.92	0.79
9	4.10	1.80
10	4.10	1.90

(Broad wall width = 5mm)

TABLE III

THE PARAMETERS OF THE RADIATING UNIT

Unit	Ls (mm)	Lstair (mm)	hstair (mm)
1	3.73	2.26	0.37
2	3.80	2.26	0.37
3	3.85	2.26	0.37
4	3.89	2.26	0.37
5	3.92	2.26	0.37
6	3.97	2.26	0.37
7	4.02	2.26	0.37
8	4.10	2.12	0.37
9	4.50	2.72	0.37
10	4.90	2.42	0.316

(Broad wall width = 7.112 mm, slot offset = 1.38 mm)

TABLE IV

THE PARAMETERS OF THE RADIATING UNIT

Unit	Ls (mm)	Lo(mm)
1	3.80	1.38
2	3.84	1.38
3	3.90	1.47
4	3.86	1.70
5	3.88	1.90
6	3.86	2.30
7	3.85	2.80
8	3.88	2.80
9	3.88	2.80
10	3.88	2.90

(Broad wall width = 7.112 mm)

4.4 Feed part design

The feeding section of the 10×10 single-layer waveguide slot array antenna consisted of a standard WR-28 input aperture, a T-junction 50:50 power splitter, and two 1 × 5 alternating phase-fed radiating waveguides. Figure 11(a) illustrates the configuration of the input aperture and T-junction 50:50 power splitter, where a standard WR-28 waveguide connects to the T-junction using a matching waveguide. Due to the perfect symmetry of the structure in Figure 4.11(a), the waves coupled to the two directions of the T-junction exhibit precisely equal power amplitude and a 180-degree phase difference. Hence, by tuning the length (a), width (b), and height (h) of the matching waveguide to achieve impedance matching and suppress total reflection, we achieved a reflection of -53 dB at 38 GHz when setting (a, b, h) to (4.47 mm, 3.10 mm, 3.20 mm), as depicted in Figure 4.11(b).

The configuration of the 1 × 5 fed waveguides is illustrated in Figure 4.12. Initially, we set the length (l) to 5.225 mm to ensure that the half-wavelength in the waveguide (1/2 λg) is equal to 6.015 mm, which is the sum of the broad wall width (5 mm) and the sidewall thickness (1.015 mm) for the alternating phase-fed condition. Additionally, we precisely adjusted the width (w) and offset (d) of the feed waveguide port, as shown in Figure 4.12(b), to control the phase and amplitude of the fed wave. Furthermore, an inductive wall was incorporated to suppress total reflection, utilizing parameters (d_2) and (q) as depicted in Figure 4.12(b). Four parameters (d, w, d_2, and q) were designed to achieve the two desired properties listed in Table V. Firstly, we achieved less than -20 dB reflection for each port and nearly equal fed wave power distribution (with a power deviation of < 0.43 dB) across all ports, as shown in Figure 13(a). Secondly, we attained an alternating phase-fed condition with a phase deviation of < 1°, as demonstrated in Figure 4.13(b). Besides, we give the deign of feed waveguide for WR-28 also for a reference in Table VI.

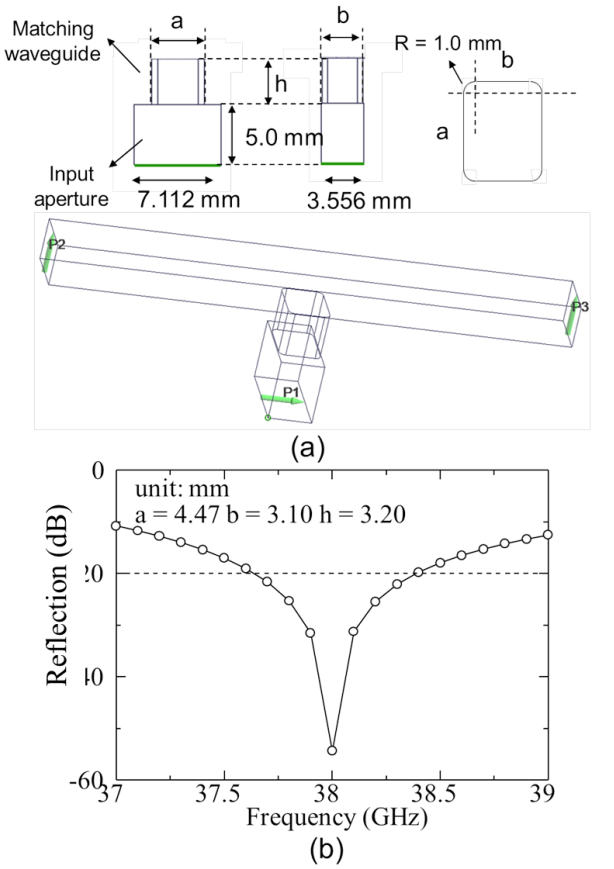

Fig. 4.11. (a) configuration of input aperture, matching waveguide and 3 dB power divider. (b) The reflection (S11) as a function of frequency, when setting the parameters of (a, b, h) = (4.47 mm, 3.10 mm. 3.20 mm).

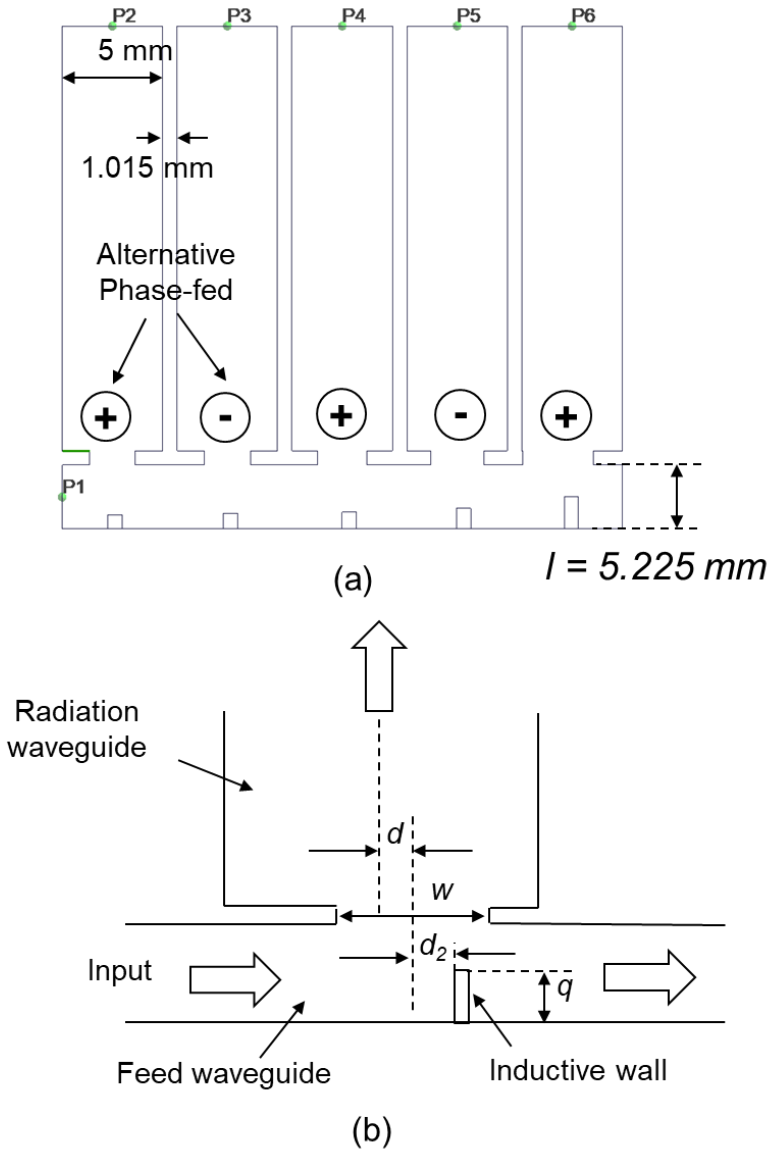

Fig. 4.12. (a) top view of 1x5 feed waveguide (b) the configuration of feed aperture.

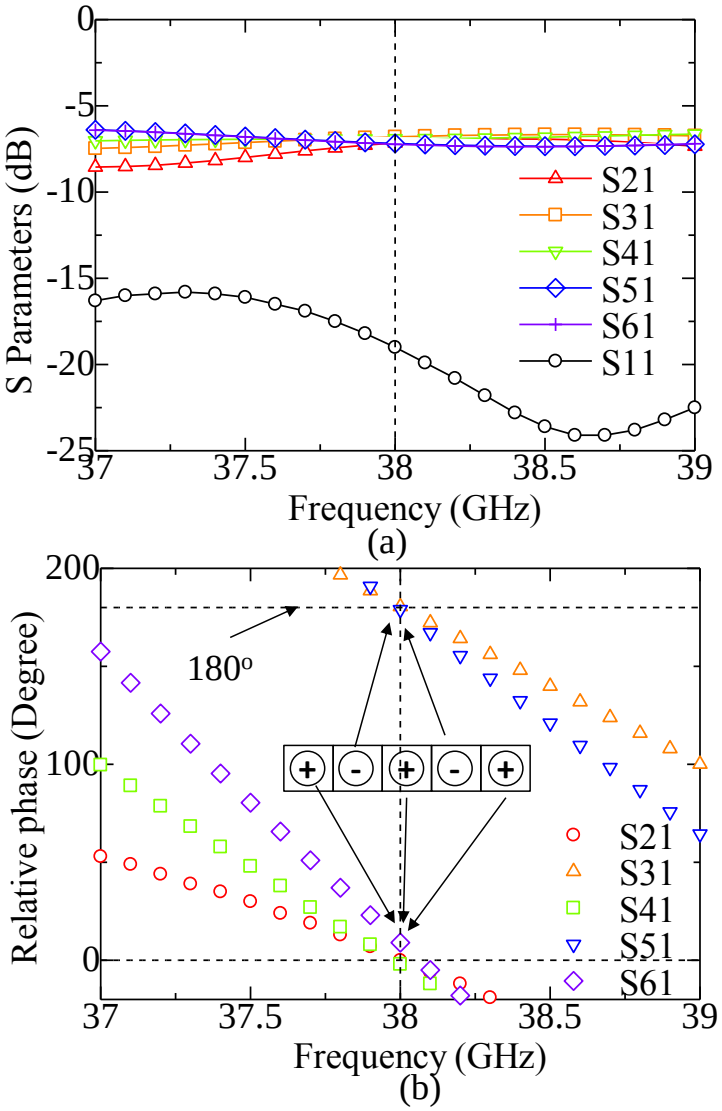

Fig. 4.13. (a) amplitude of each S parameters as a function of frequency. (b) relative phase of each feed waveguide. (Port 1 is input aperture, while port 2~6 are feed waveguide.)

TABLE V

THE PARAMETERS OF THE WAVEGUIDE

Unit	w (mm)	d (mm)	d_2 (mm)	q (mm)
1	3.20	0	-0.3	1.00
2	3.30	0	-0.3	1.10
3	3.50	0	-0.1	1.20
4	3.75	0	0	1.45
5	5.00	-0.1	-0.5	2.30

Broad wall width = 5 mm

TABLE VI

THE PARAMETERS OF THE WAVEGUIDE

Unit	w (mm)	d (mm)	d_2 (mm)	q (mm)
1	3.20	0	-0.3	1.00
2	3.30	0	-0.3	1.10
3	3.50	0	-0.1	1.20
4	3.75	0	0	1.45
5	5.00	-0.1	-0.5	2.30

Broad wall width = 7.112 mm

(a,b,h,l)=(2.400,3.684,3.700,4.512) mm

4.5 Numerical analysis of device

In this section, we carry out simulations based on the 4 types of design slotted waveguide. The simulation target is not only a linear slotted waveguide with 10 radiating unit, but also the performance of 10x10 array and the performance of the whole model of all 4 types of slotted waveguide are carried out. Consequently, we present the reflection and radiation properties of all 4 types of slotted waveguides. The radiation pattern and aperture efficiency analysis will be done together with measurement result in next chapter. In the following subsection, we just give the plot of partial simulation for explanation. However, all simulation results can be found in the Table VII in the final of this chapter.

4.5.1 Single waveguide

Consequently, we compare the performance between a single waveguide with and without reflection canceling stairs in Fig. 4.14. Figure 4.14(a) illustrates the reflective properties as a function of frequency between two kinds of radiating waveguides. We confirm effective reflection suppression is achieved by employing reflection canceling stairs, as shown by the black dot line in Fig. 4.14(a). At 38 GHz, S11 is -14.5 dB for the waveguide with stair, while S11 is -6.2 dB for the waveguide with the only slot. Figure 4.14(b) illustrates the directive gain between two kinds of waveguides, that 15.9 dBi (aperture efficiency of 63.5%) for the waveguide with stair and 13.1 dBi (aperture efficiency of 33.3%) for the waveguide with the only slot.

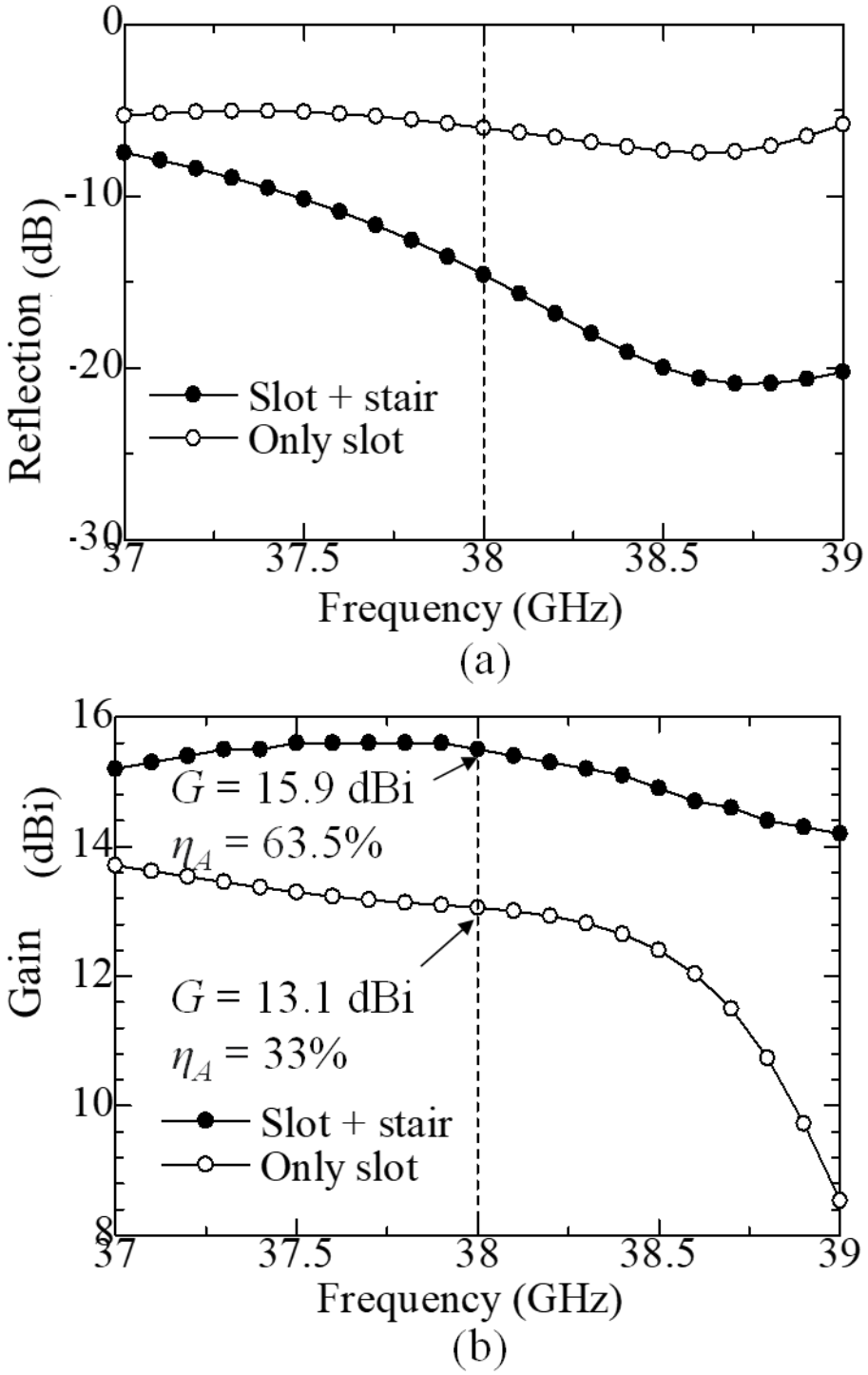

Fig. 4.14. (a) The reflection characteristics (S11) and (b) the directive gain as a function of frequency based on the radiating waveguide with 10 pairs slot and stair and with only slot, respectively.

4.5.2 10x10 array

Figure 4.15 shows the performance of the full model, which includes input aperture, matching waveguide, two 1x5 feed waveguides, and a 10x10 slotted radiating waveguide array. The lines with triangle, square and circle in Fig. 4.15(a) show the respective reflection properties of input aperture, feeding waveguide, and radiating waveguide. In contrast, the line with black dot in Fig. 4.15(a) denotes the total reflection from a full model. -14.5 dB reflection of the full model is achieved at 38 GHz. The black dot line in Fig. 4.15(b) illustrates the directive gain of the full model, while the directive gain of only the 10x10 slotted waveguide array is plotted in the same figure in the black circle line. As a result, we obtain 23.3 dBi (aperture efficiency of 30.3%) for the array with only radiating waveguide, while we obtain 22.9 dBi (28.2%) for the full model at 38 GHz.

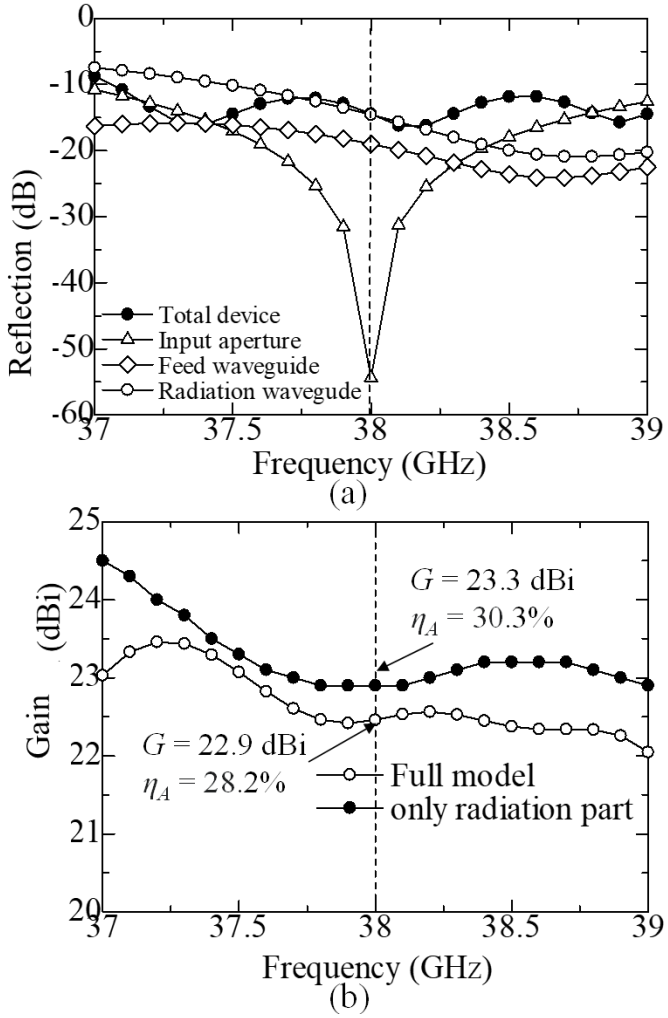

Fig. 4.15. (a) The reflection of each part and entire device (including input aperture, feed waveguide and radiating waveguide). (b) The directive gain of 10x10 array as a function of frequency. (Blue is for full model, black is for only radiating waveguide)

4.5.3 Full model analysis

Figure 4.16(b) compares directive gain among three radiating waveguide arrays. First, we achieve a 27.9 dBi directive gain at 38 GHz using a 5 mm broad wall waveguide array with 10x10 pairs slots and reflection canceling stairs [see the black dot at Fig. 4.16(b)]. The corresponding aperture efficiency is 89.4%. In contrast, low efficiency is obtained for the 5 mm waveguide with only slot and the 7.112 mm

waveguide with reflection canceling stair. Thus, we confirm both the coupling effect between the adjacent waveguide and the reflection of the waveguide can dramatically degrade the performance of the antenna array.

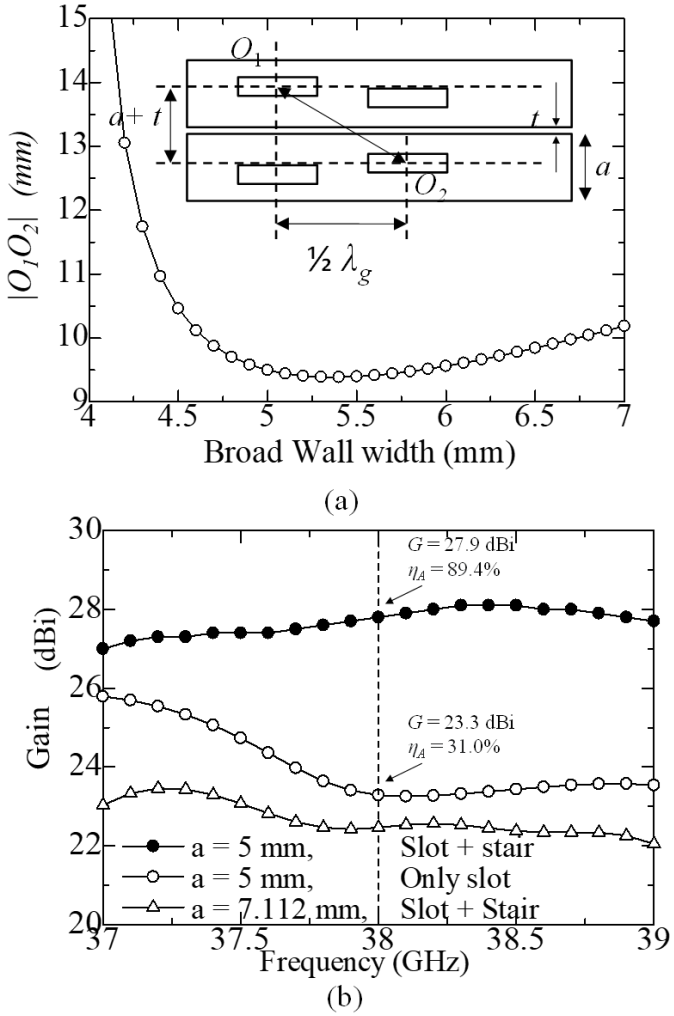

Fig. 4.16. (a) $|O_1O_2|$ as a function of broad wall width, (b) the directive gain as a function of frequency among three kinds of radiating waveguide array (black circle: the 5-mm waveguide with stair , blue circle: the 5-mm waveguide with only slot, and black triangle: 7.112-mm waveguide with stair)

4.6 Summary

In general, we have numerically demonstrated a high-efficiency single-layer slotted waveguide array antenna. Furthermore, only a 0.4 dB power penalty by adding the feeding part indicates that this design is feasible for fabrication.

In the feeding part design, we successfully demonstrate an input aperture with > 800-MHz bandwidth and < -30 dB S11. In addition, we realize alternative-phase (deviation < 1 degree for the first four ports and < 10 degree for the end port) uniform-power (deviation < 0.43 dBi) feeding for ten radiating waveguides through two 1x5 feed waveguides. In the radiating waveguide design part, we successfully suppress the reflection of a single waveguide < -14.5 dB by employing reflection canceling stairs. Simultaneously, the power compensation effect of stair makes it possible to use constant offset for ten slots.

For the waveguide array design, we minimize the offset and the $|O_1O_2|$ to effectively eliminate the grating side lobes. As a result, we realize a remarkable high aperture efficiency of 89.4% with a 5 mm broad wall width.

Table VII

Summary of simulated performance of 4 types of devices

Waveguide type	broad wall width（mm）	Slot only	Slot and step	Pmax (dBi) *	Pout at 38-GHz (dBi)	aperture efficiency（38 GHz）
Single waveguide	5	○		13.99	12.64	32.4%
			○	15.68	15.59	63.9%
	7.112	○		13.71	13.06	33.1%
			○	15.6	15.51	58.1%
10 waveguides array	5	○		25.77	23.26	30.7%
			○	28.4	28.2	95.8%
	7.112	○		-	-	-
			○	24.47	22.89	28.2%
Full mode with feeding part	5	○		25.61	22.57	26.2%
			○	28.24	27.74	86.2%
	7.112	○	-	-	-	-
			○	23.46	22.6	26.3%

* Pmax means the maximum power at the frequency range of 37~39 GHz

Notice: In this chapter, we just show partial of the measurement results of the Table VII to avoid possible confuse. We want to explain that we have compare the linear waveguide, the array and the entire model respectively. To find more data plot, you can refer the content in App. V.

4.7 References

[4.1] Y. Tsunemitsu et al., "Single-layer slotted waveguide array with reflection canceling stairs," in proc. IEEE AP-S Int. Symp., Albuquerque, USA, 2006. pp. 3149-3152.

[4.2] W. Liu and Y. Tsunemitsu, "The Slotted Waveguide Array Antenna with Reflection Canceling Stairs in Millimeter Waveband," in proc. EuCAP, Copenhagen, Denmark , 2020, pp. Poster-2-A10.

[4.3] W. Liu and Y. Tsunemitsu, "The Waveguide Slot Array Antenna in Millimeter Waveband using the Reflection Canceling Stairs for the Sidelobe Suppression," in proc. IEEE AP-S Int. Symp., Montreal, Canada, 2020, pp. 531-532.

[4.4] W. Liu and Y. Tsunemitsu, "A Single-Layer Center-Feed Slotted Antenna Array with Reflection Canceling Stairs in 38-GHz Waveband," in proc. EuCAP, Madrid, Spain, 2022.

[4.5] W. Liu and Y. Tsunemitsu, "Grating Sidelobe Suppression in Single-Layer Center-Feed Waveguide Antenna Array at 38 GHz," in proc. IEEE AP-S/URSI. 2022, pp. 1220-1221.

[4.6] W. Liu and Y. Tsunemitsu, "A Waveguide Slot Array Antenna With Reflection-Canceling Stairs for Sidelobes Suppression at 38 GHz," in IEEE Access, vol. 11, pp. 72942-72949, 2023. doi: 10.1109/ACCESS.2023.3294821

Chapter 5. Fabrication and characteristics of antenna

5.1 Schematic figure of the device and characterization setup

Figure 5.1 shows the configuration of an alternating phase-fed single-layer waveguide slot array antenna with 10 × 10 slots. The design frequency is set to 38 GHz. The input aperture consists of a standard WR-28 waveguide [See Figure 5.1]. To facilitate fabrication and increase the manufacturing yield rate, the three parts of the antenna can be individually fabricated and connected with bolts. This modular design allows for easier assembly and adjustment.

In the input aperture part, a matching waveguide with a 1/4 guided wavelength is employed, along with a feed waveguide located between the input aperture (WR-28) and the 3 dB power divider for reflection suppression. The feed waveguide utilizes an alternative-phase configuration, wherein adjacent waveguides have a 180-degree phase difference and a uniform amplitude distribution. This arrangement effectively cancels the current on the side walls, eliminating the need for electrical connection between the top radiating plate and the waveguide-based layer.

Furthermore, each feeding aperture incorporates an inductive sidewall to enhance feeding efficiency by precisely tuning the amplitude and phase of the TE10 wave. To achieve a high gain, RCSs are employed for each slot on the radiating waveguides. The radiation section of the antenna features slots spaced at intervals of 1/2 guided wavelength along the longitude direction to mitigate the mutual coupling effect.

All the parameters of feeding part, radiating part for both two devices can be found in the Table I and Table II, Chapter 4.

The proposed antenna design parameters derived in Section III were utilized for the fabrication of the antenna by Oshima Prototype Engineering Co., Ltd. To serve as a reference, a traditional antenna array without RCSs was also manufactured. Figure 5.2 presents top, back, and side views of the fabricated device, which features a

compact single-layer configuration and a standard WR-28 aperture, ensuring ease of use.

To evaluate the performance of the fabricated antenna, the reflection coefficient S11 was measured using the Keysight (Agilent) N5234A PNA-L vector network analyzer covering a frequency range of 10 MHz to 43.5 GHz. Short-open-load-through (SOLT) calibration was performed using an Agilent 85056D calibration kit. In addition, commercial software Femtet was employed for finite-element method (FEM) simulations of the S parameters, enabling a comparison of the measurement and simulation results.

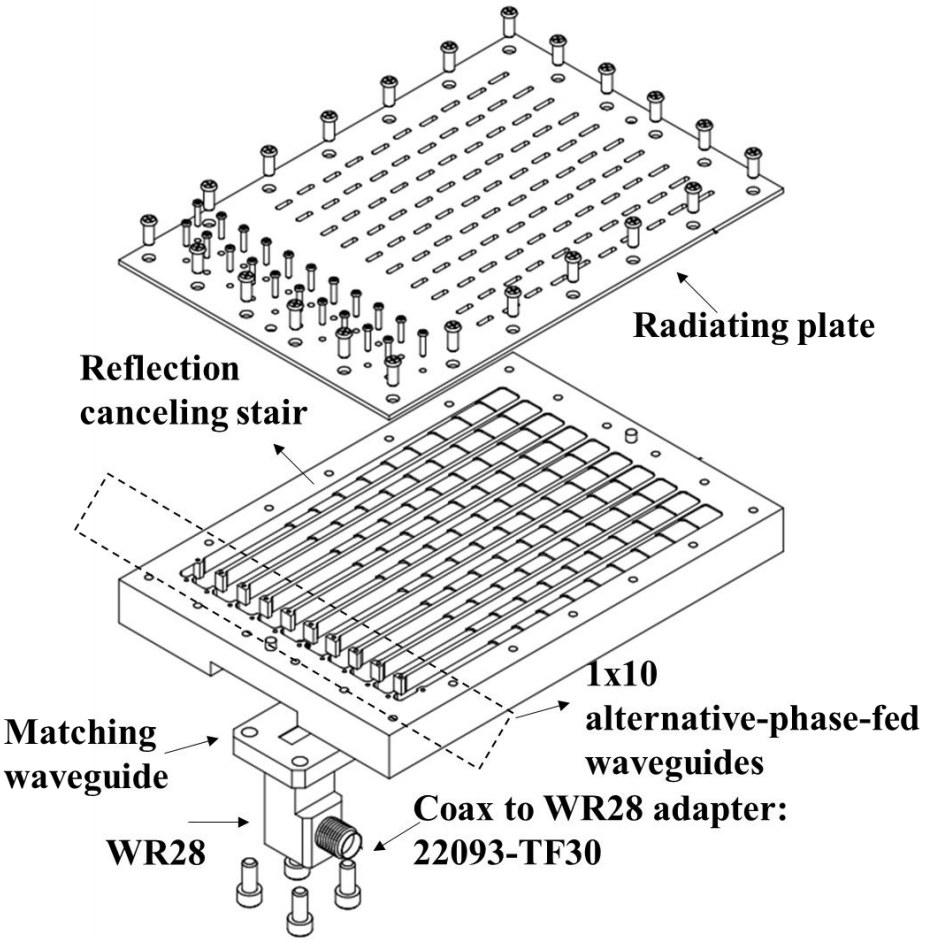

Fig. 5.1. Configuration of a single-layer 10x10 alternative phase-fed slotted waveguide array antenna.

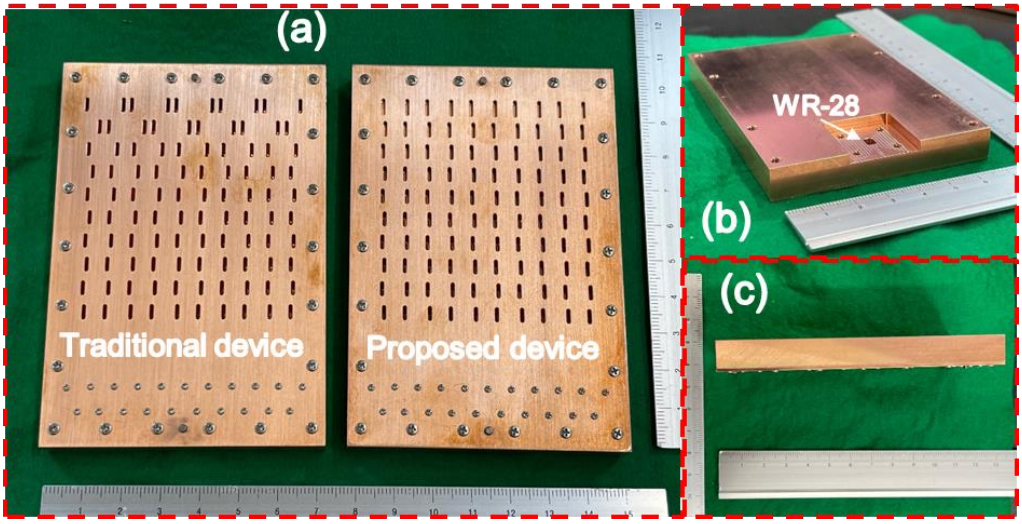

Fig. 5.2. (a) top view of the 10x10 antenna array (screws are used to fix the top radiation plate and the rest part). (b) the backside of the device. (c) side view of device.

5.2 Characterization method

The characterization method is illustrated in Figure 5.3.

Figure 5.3(a) shows that to measure the S11 parameter is simple, and ca be done directly by the network analyzer N5234A.

To estimate the absolute maximum radiation power, a comparison was conducted between the measured radiation pattern of the Device Under Test (DUT) and that of a standard gain horn antenna (FLANN MICROWAVE Model 22240-25) [See Figure 5.3(b)].

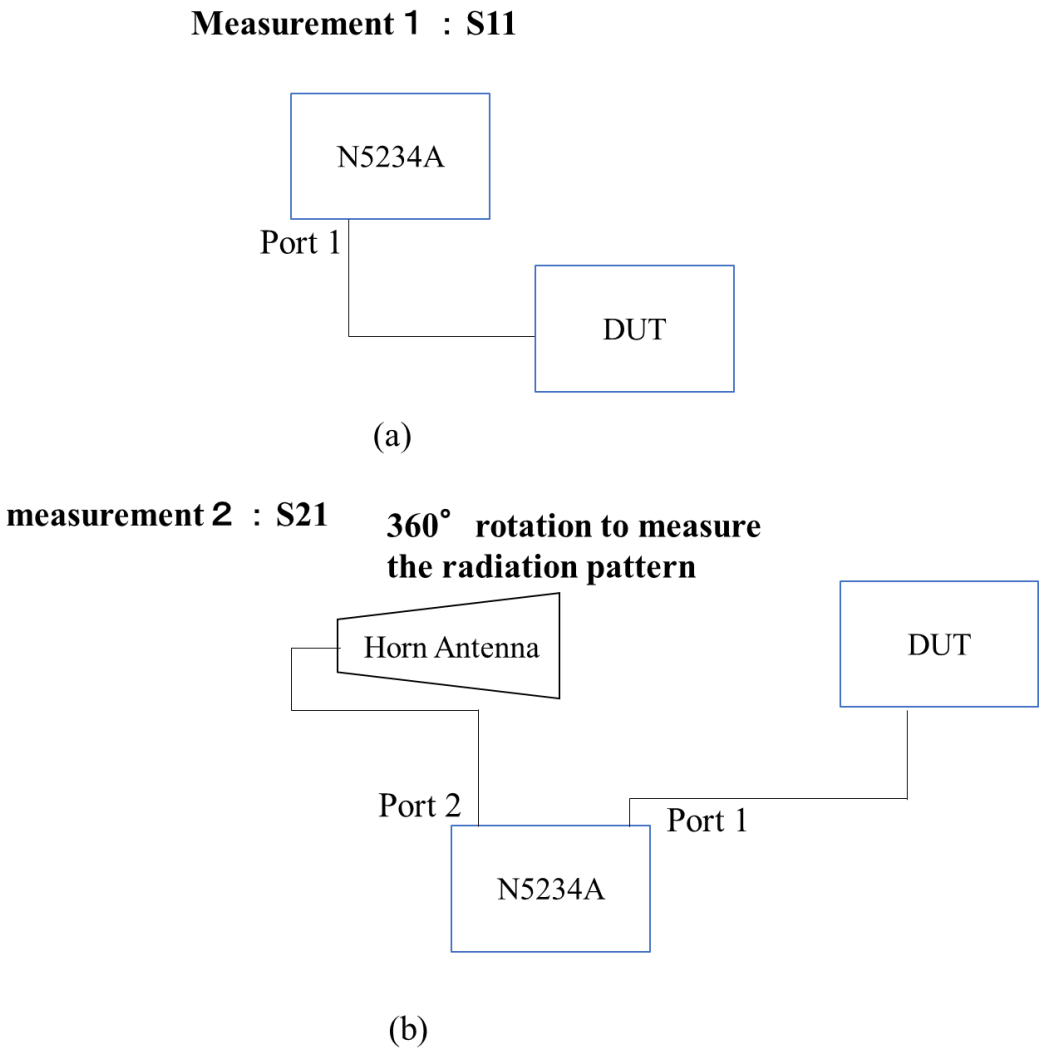

Fig. 5.3. Measurement setup of (a) reflection properties S11, (b) radiation properties S21.

5.3 Radiation pattern

Figure 5.4 illustrates the comparison between the RCS antenna array (red) and the conventional antenna array (black). The graph plots the S11 parameter (reflection) as a function of frequency from 37 to 39 GHz. Both experimental (solid line) and simulated data (dashed line) are presented, showing good agreement. The results

validate the accuracy of the simulation and demonstrate the superior performance of the RCS antenna array, which exhibits reduced reflection losses (< 15 dB at 38 GHz). This graph provides compelling evidence supporting the advantages of the RCS design within the specified frequency range, contributing to the overall findings of the study.

Figures 5.5 and 5.6 illustrate the relative radiation patterns of the antenna array. The solid lines correspond to the measured results, while the dashed lines represent the simulated results. Specifically, the red lines illustrate the device equipped with RCSs, while the blue lines depict the device without RCSs. The strong agreement observed between the measured and simulated results in both Figure 5.5 and Figure 5.6 provides compelling evidence for the successful fabrication of devices with both configurations. Moreover, previous observations have highlighted that although the sidelobes on the E or H plane, resembling those of a co-phase fed antenna array, do not significantly affect the antenna gain. In contrast, the presence of large sidelobes in the ϕ = 45-degree plane, arising from the increasing slot offset, heavily degrades antenna performance. Consequently, addressing this issue is important. In this context, Figure 5.6 focuses specifically on the relative radiation patterns on the ϕ = 45-degree plane. By incorporating RCSs, both the simulation and experimental results demonstrate a remarkable reduction in the first grating sidelobes near $\theta = \pm 60°$ on the ϕ = 45-degree plane, with suppression levels ranging from -10 dB to -20 dB. These results suggest that the integration of RCSs holds great potential for enhancing antenna efficiency by effectively mitigating sidelobes.

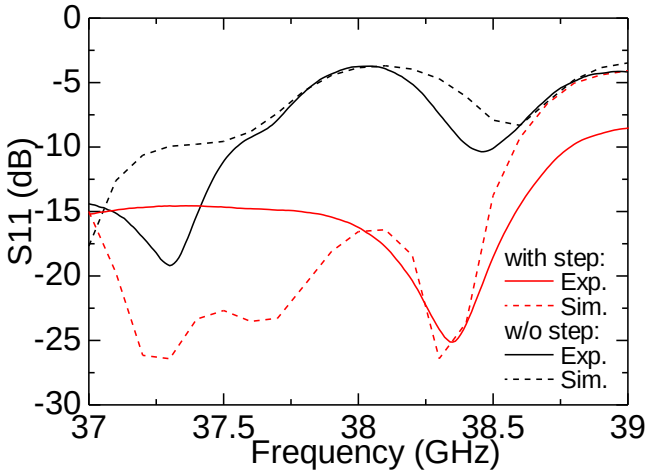

Fig. 5.4. Comparison of the reflection coefficient S11. (red line: device with reflection canceling stairs, black line: device with only slot, solid line: experimental data, dashed line: simulation data)

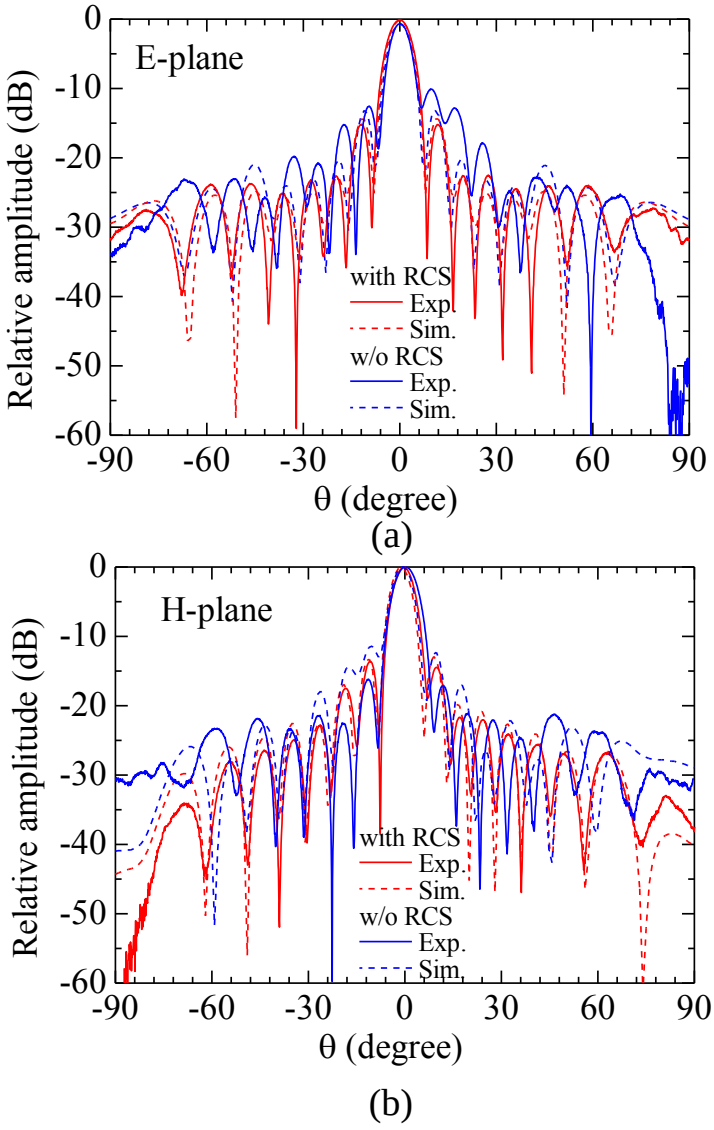

Fig. 5.5. Radiation pattern in (a) E-plane and (b) H-plane.

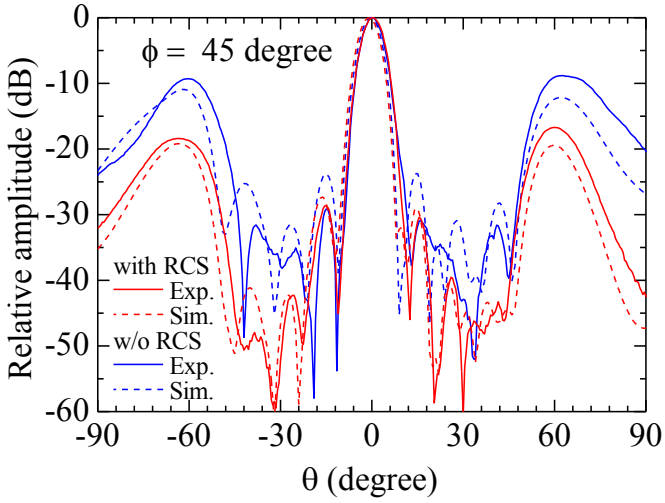

Fig. 5.6. Measured and simulated radiation pattern on phi = 45-degree plane.

5.4 Antenna gain and aperture efficiency

Figure 5.7 illustrates the simulated gain between 37 to 39 GHz by solid lines, while the measured gains at 37, 38, and 39 GHz are represented by diamond marks, respectively. The dashed straight lines in the figure indicate the aperture efficiency (η), which is calculated using Equation (7) [5]:

$$\eta = \frac{\lambda^2 G}{4\pi A} \tag{7}$$

Here, λ represents the free-space wavelength, G denotes the linear gain, and A signifies the effective radiation area.

At 38 GHz, the proposed antenna exhibited measured and simulated gains of 27.71 dBi (85.6%) and 27.74 dBi (86.1%), respectively. In contrast, the traditional antenna demonstrated measured and simulated gains of 22.67 dBi (26.8%) and 22.60 dBi (26.4%), respectively, at the same frequency. Additionally, an aperture efficiency larger than 80% was achieved by incorporating reflection canceling structures (RCSs) within the frequency range of 37.5 to 38.5 GHz.

Figure 5.8 shows the simulation results of ideal 10x10 arrays and full models, both with and without RCSs. It can be observed that within the range of 37.5 to 38.5 GHz, only a negligible loss of below 0.5 dB was incurred due to the design of the feeding component. However, outside this frequency range, the full model exhibited lower gain, indicating that the efficiency degradation beyond the range of 37.5 to 38.5 GHz is primarily attributed to limitations in the design of the feeding component.

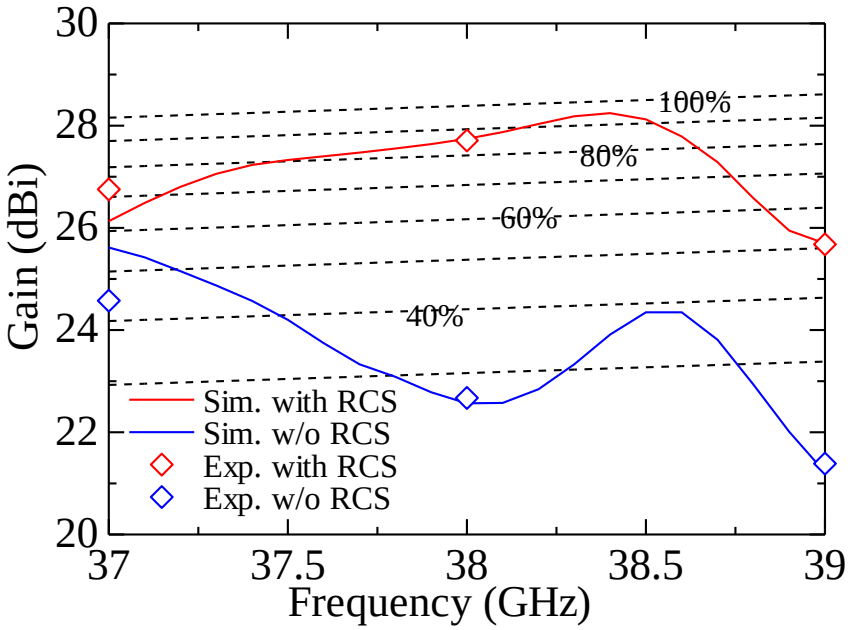

Fig. 5.7. Antenna gain as a function of aperture efficiency.

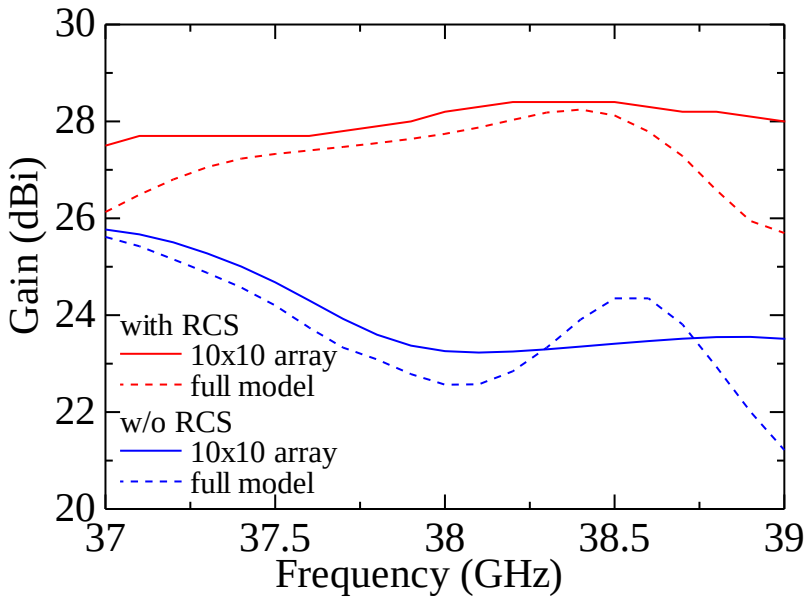

Fig. 5.8. Simulated antenna gain between 10x10 array and full model.

5.5 Summary

This section details the fabrication and performance evaluation of an antenna design with reflection canceling structures (RCSs) and a traditional antenna array without RCSs for reference. Utilizing the proposed design parameters, the antenna features a compact single-layer configuration and a standard WR-28 aperture, ensuring ease of use. Measurement and simulation results of the reflection coefficient S11, depicted in Figure 10, validate the accuracy of the finite-element method (FEM) simulations. The RCS antenna array exhibits reduced reflection losses (< 15 dB at 38 GHz), showcasing superior performance within the specified frequency range.

Relative radiation patterns (Figures 11 and 12) confirm successful fabrication of devices with both configurations, emphasizing a remarkable reduction in sidelobes near $\theta = \pm 60°$ on the $\phi = 45$-degree plane with RCSs. This reduction suggests the potential of RCSs in enhancing antenna efficiency by mitigating sidelobes.

Comparisons with a standard gain horn antenna demonstrate higher gains and aperture efficiency (> 80%) at 38 GHz for the proposed antenna compared to the traditional one. Future work could explore further optimizations beyond the specified frequency range, addressing limitations in the design of the feeding component and extending the efficiency gains observed within the current parameters. The results affirm the effectiveness of the proposed RCS design in enhancing antenna performance, providing a promising foundation for future advancements in antenna technology.

5.6 References

[5.1] Y. Tsunemitsu et al., "Single-layer slotted waveguide array with reflection canceling stairs," in proc. IEEE AP-S Int. Symp., Albuquerque, USA, 2006. pp. 3149-3152.

[5.2] W. Liu and Y. Tsunemitsu, "The Slotted Waveguide Array Antenna with Reflection Canceling Stairs in Millimeter Waveband," in proc. EuCAP, Copenhagen, Denmark , 2020, pp. Poster-2-A10.

[5.3] W. Liu and Y. Tsunemitsu, "The Waveguide Slot Array Antenna in Millimeter Waveband using the Reflection Canceling Stairs for the Sidelobe Suppression," in proc. IEEE AP-S Int. Symp., Montreal, Canada, 2020, pp. 531-532.

[5.4] W. Liu and Y. Tsunemitsu, "A Single-Layer Center-Feed Slotted Antenna Array with Reflection Canceling Stairs in 38-GHz Waveband," in proc. EuCAP, Madrid, Spain, 2022.

[5.5] W. Liu and Y. Tsunemitsu, "Grating Sidelobe Suppression in Single-Layer Center-Feed Waveguide Antenna Array at 38 GHz," in proc. IEEE AP-S/URSI. 2022, pp. 1220-1221.

[5.6] W. Liu and Y. Tsunemitsu, "A Waveguide Slot Array Antenna With Reflection-Canceling Stairs for Sidelobes Suppression at 38 GHz," in IEEE Access, vol. 11, pp. 72942-72949, 2023. doi: 10.1109/ACCESS.2023.3294821

Chapter 6. Comprehensive investigation on slotted waveguide antenna

6.1 Fabrication tolerance improvement by inclined stairs

We propose and optimize the slotted waveguide antenna with inclined reflection canceling stair to enhance the design flexibility and suppress the side lobes rising from the offset variation. By employing the inclined slope on the stair, better phase and amplitude matching condition have been achieved which results in ultra-low reflection of -77 dB for single unit. In addition, there is a tradeoff between the minimal reflection condition and the most flexible design condition of the inclined slope. By setting h1 as 0.36 mm, below - 40 dB reflection can be obtained when the h2 is within the range of 0.1 to 0.8 mm. Thus, we can tune the h2 to adjust the waveguide space of next slot to realize uniform radiation without introducing any varying offset.

Fig. 6.1 illustrates the schematic structure of one unit of the proposed slotted waveguide antenna. The slot length (Ls) and offset (L_o) are designed in advance to achieve uniform radiation. To obtain 10% radiation, respective value L_s and L_o are 3.88 and 1.38 mm, while the width and height of rectangular waveguide are 3.556 and 7.112 mm. Consequently, there are 3 parameters to describe the inclined stair as shown in Fig. 6.1. As the discussion in , the reflection canceling effect is obtained due to the reflection from slot and stair have equal amplitude and 180^o phase difference, which results in mutually cancel for them to obtain ultra-small reflection. As a result, the h_1 and L_{stair} are tuning the amplitude and phase of reflection from the stair respectively in [1]. Moreover, in this paper, the inclined slope with parameter of h_2 can precisely adjust both the phase and amplitude simultaneously. Fig. 6.2 illustrates a comparison between the slotted waveguide with rectangular stair [black dot line] and with proposed inclined stair [red dot line]. The compensated function of inclined stair is proved that -77 dB reflection is obtain when (h_1, h_2) = (0.41 mm, 0.40 mm), which is 20 dB smaller than the waveguide with only rectangular stair.

Fig. 6.3 illustrates that, there is a large flexibility of inclined slope. when the h_1 is kept as 0.36 mm, less than -40 dB reflection of the unit can be achieved only if the h_2 is with the range of 0.1 to 0.8 mm. The flexibility of h_2 makes it possible to control

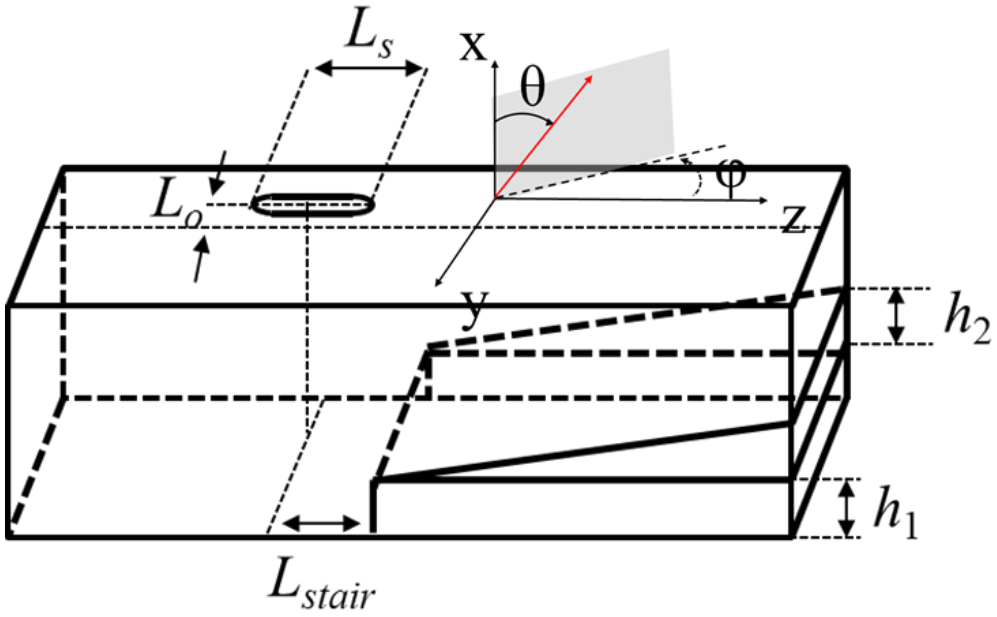

Fig. 6.1. The schematic of proposed slotted waveguide antenna with inclined reflection canceling stair. Notice that all the definition of φ and θ in this paper are based on this figure.

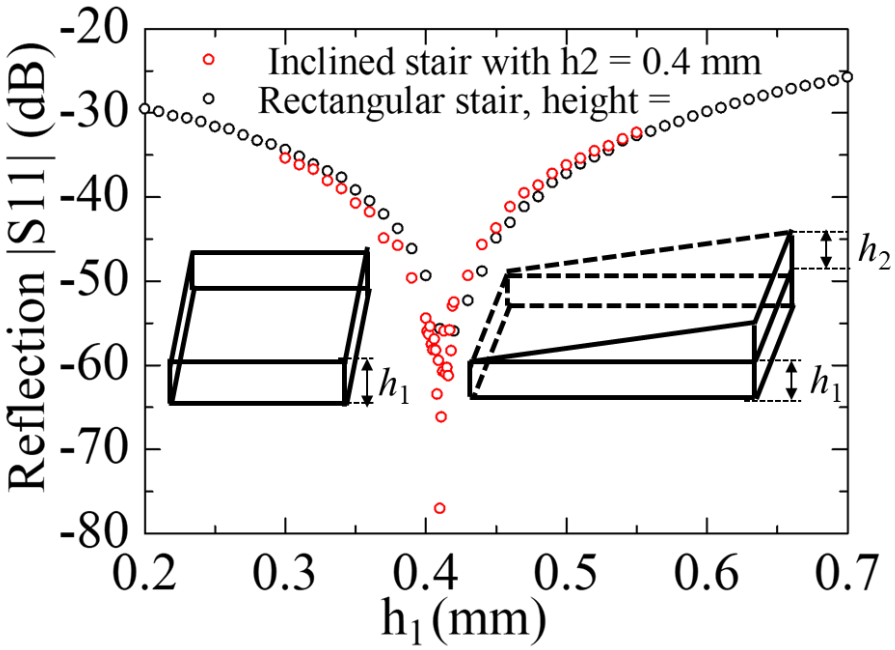

Fig. 6.2. The reflection amplitude |S11| as a function of height. Red line denotes a sweeping curve of waveguide with an inclined stair where the h1 is fixed as 0.4 mm

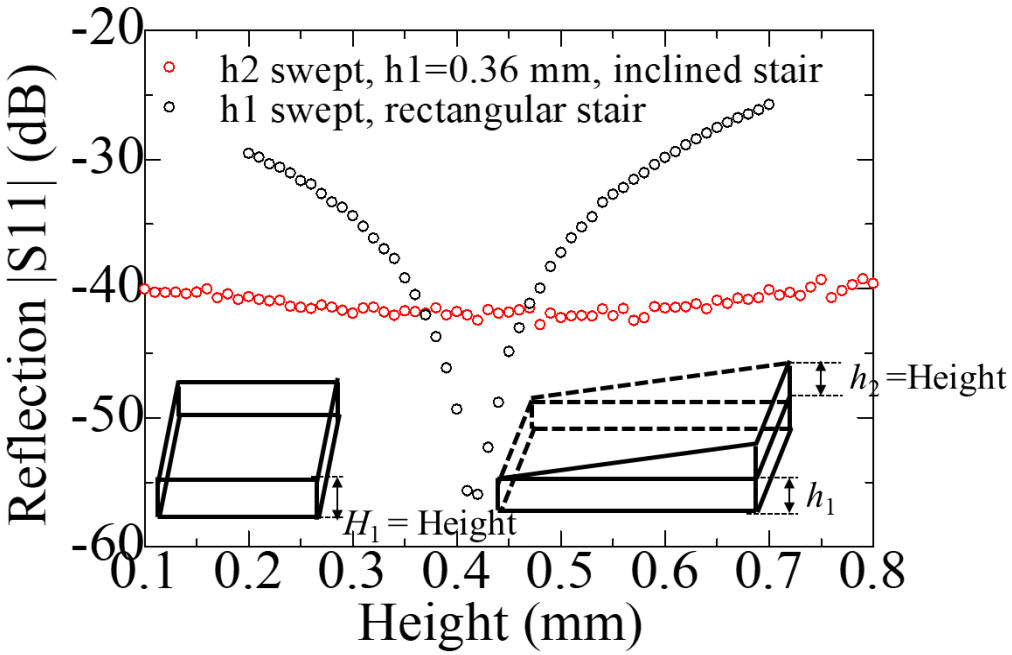

Fig. 6.3. The reflection amplitude |S11| as a function of height. Red line denotes a sweeping curve of waveguide with an inclined stair where the h is fixed as 0.36 mm and h1 is swept from 0. 1 to 0.8 mm. Black line denotes a sweeping curve of waveguide with only stair, where h is swept from 0.2 to 0.7 mm.

the waveguide height of next slot to tuning the radiation amount without changing the offset and h1 is swept from 0. 3 to 0.55 mm. Black line denotes a sweeping curve of waveguide with only stair, where h is swept from 0.2 to 0.7 mm.

We have proposed and numerically analyzed an inclined slope employing on the rectangular reflection canceling stair for sotted waveguide antenna for millimeter applications. The enhancement of reflection suppression by the inclined slope was confirmed by using proposed device with parameters of (h_1, h_2) = (0.4 mm, 0.41 mm), where -77 dB reflection (>20 dB better than rectangular stair) was obtained. Consequently, we have also confirmed the large design flexibility of the inclined slope that -40 dB reflection with h_1 = 0.36 mm can be achieve only if h_2 is at the range of 0.1 to 0.8 mm.

6.2 Round type radiating array

Based on the same slotted waveguide design procedure in [1,2], we can design a 10×10 array with slotted waveguide antenna based on inclined reflection canceling stair. For comparison, we also investigate the radiation distribution of 10×10 array with rectangular reflection stair in Fig. 6.4. where Fig. 6.4(a) illustrates the 3-dimensional radiation pattern. Figure 6.4(b) shows the radiation pattern of designed array with inclined stair. We notice that much stronger suppression is achieved in Fig. 6.4(b) such as at $\varphi = 0$ and 90 degree plane. There are two different reasons for generation of large side lobe at the $\varphi = 0, 90$ degree and at 45-degree plane. The former is caused due to the unoptimized geometry of slot allocation of the array. Since the rectangular reflection canceling stair has strict height, we need to adjust the offset of next slot to achieve uniform radiation. The un-flexibility of design of slot also brings difficulty to design an antenna with different numbers of slots, which is essential for array. The latter is caused due to the varying-offset of each slot. To solve the problems above, we propose the optimized array deign in Fig. 6.4(b) with inclined stair. By shrinking the waveguide at edge, the symmetry of antenna is improved, which is promising to suppress the sides lobes at E-plane and H-plane. The inclined stair provides large flexibility to keep radiation power constant without tuning the offset of slot. Consequently, it gives the freedom to manage array geometry. Figure 5(a) shows that even we decrease the number of slots from 100 to 76, similar sidelobes suppression is achieved. On the other hand, obvious improvement is obtained in E-plane and H-plane by Fig. 6.5(b).

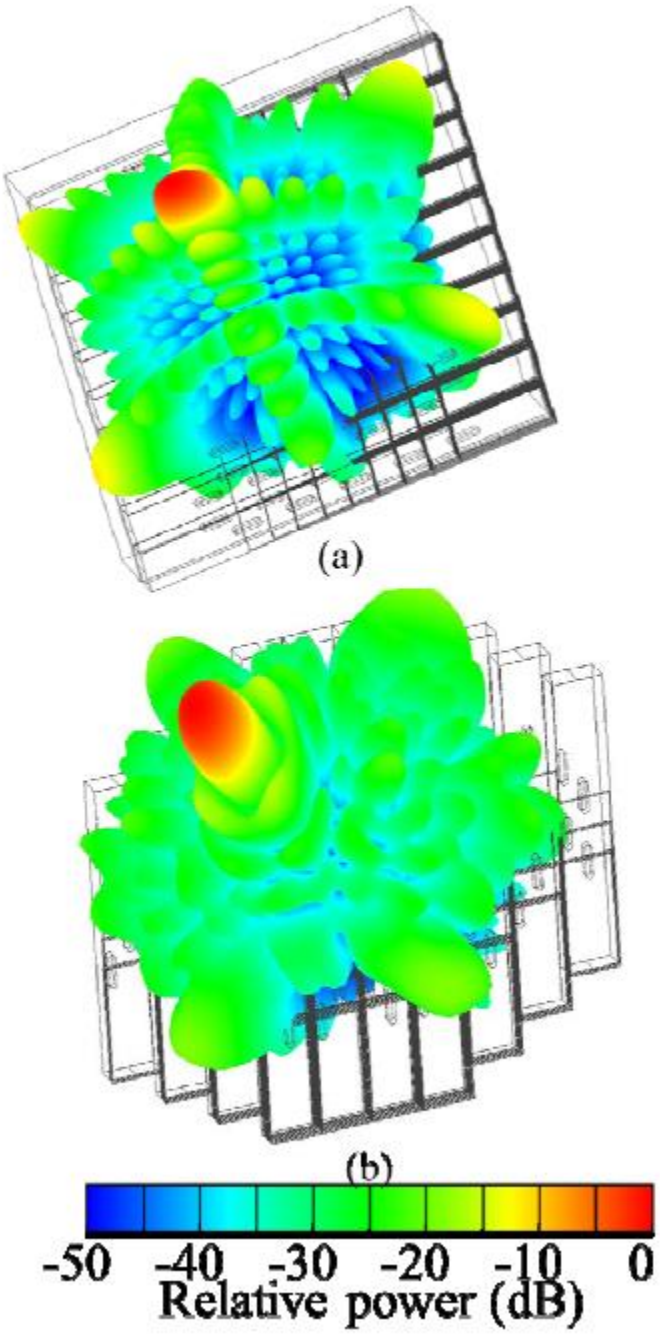

Fig. 6.4. (a) 3-dimensional radiation pattern by utilizing 10×10 array with rectangular reflection canceling stair, (b) designed antenna array with 76 slots.

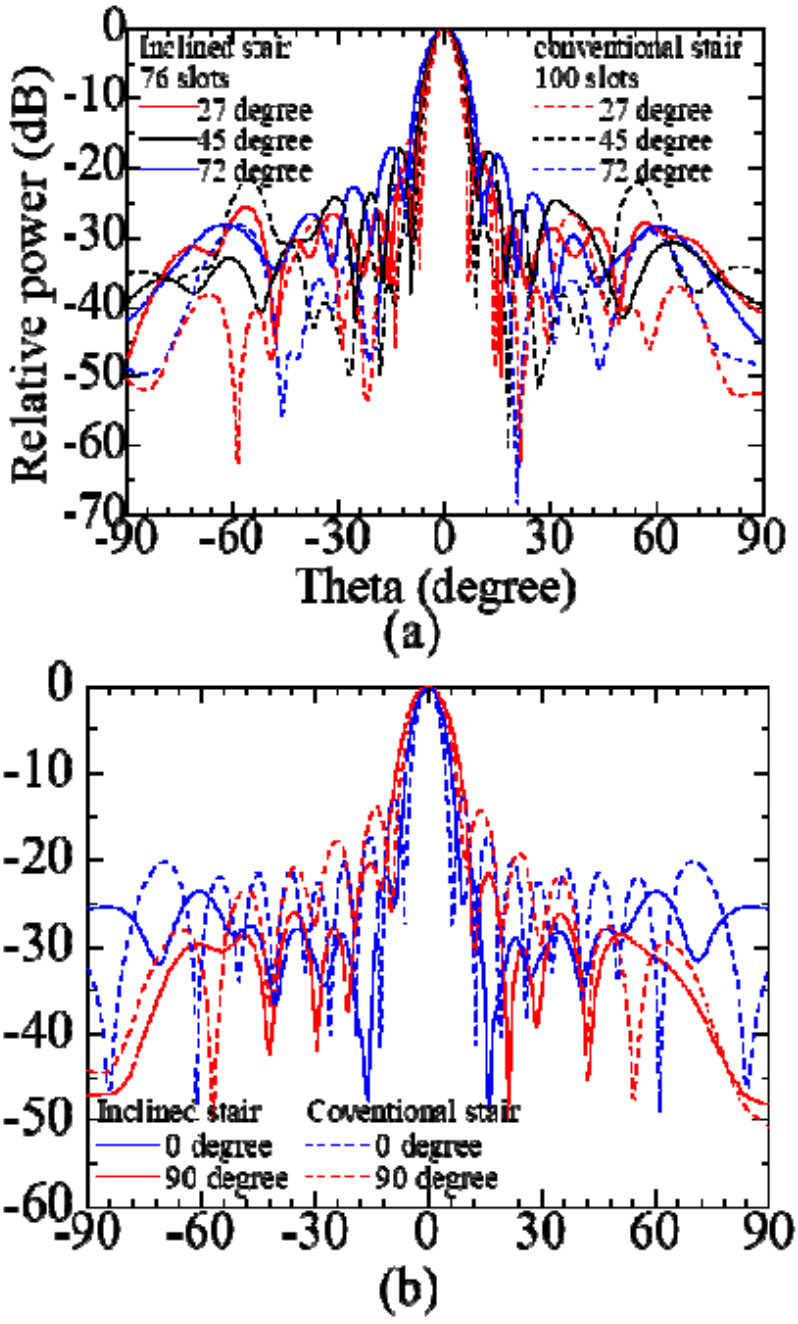

Fig. 6.5. (a) the respective relative radiation pattern in the plane of φ= 27o (red line), 45o (black line) and 72o (blue line), (b) The respective radiation pattern in the E-plane and H-plane. Notice that solid line is with inclined stair and solid line is with conventional stair. .

6.3 Discussions on the propagation loss by Perturbated-boundary condition

Perturbated-boundary condition are used in this section to evaluate propagation loss [3,4].

Loss evaluation for TE_{10} mode can be carried out by the perturbation boundary condition. The transmission loss inside a hollow rectangular metallic waveguide increases rapidly when the wavelength approaches the cutoff limitation:

$$f_c = \frac{c}{2 \cdot a} \tag{6.1}$$

First, the lossless T.E. mode can be solved by the following transverse Helmholtz equation:

$$(\nabla_t^2 + k_{c0}^2)H_{z0} = 0; \frac{\partial H_{z0}}{\partial n}|_{\partial S} = 0 \tag{6.2}$$

where $k_{c0}=\sqrt{\omega^2\mu\epsilon - k_{z0}^2}$ is the transverse wave number, and H_{z0} is the lossless magnetic field in the transmission direction.

Hence the Helmholtz equation of first order perturbation modification can be written as follow:

$$(\nabla_t^2 + k_c^2)H_z = 0; \frac{\partial H_z}{\partial n}|_{\partial S} = L(E_l) + N(E_n) \tag{6.3}$$

where the derivative of the axial magnetic field is a none zero value, which is generated from the two components (***l*** and ***n*** direction, respectively) of the surface electric field.

When considering the waveguide has a large but finite conductivity, the small tangential electric field (at the surface formed by ***l*** and ***n***) can be written by the Leontovich condition:

$$\boldsymbol{E}_{//} = \frac{1+j}{\sigma\delta}\left(\boldsymbol{n} \times \boldsymbol{H}_{o//}\right) \tag{6.4}$$

where the ***n*** is the normal unit vector outward from the waveguide surface, σ is the metallic conductivity, $\delta = \sqrt{2/(\mu_c \omega \sigma)}$ is the skin depth and $Z_s = (1+j)/\delta\sigma$ is the surface impedance. Besides, according to equation (9), the tangential electric field can be calculated as:

$$\boldsymbol{E}_{//}|\partial S \simeq (Z_s \cdot \frac{-jk_z}{k_{c0}^2} \cdot \frac{\partial H_{z0}}{\partial\, l})|_{\partial S}\boldsymbol{z} - Z_s \cdot H_{z0}|_{\partial S}\boldsymbol{l} \tag{6.5}$$

Consequently, the perturbation boundary condition generated by the ***l*** component can be written as follow through the means of Maxwell equations:

$$L(E_l) = \frac{-1}{Z_s \cdot \sigma}\omega^2 \mu\epsilon \frac{\mu_c}{\mu} H_{z0} \tag{6.6}$$

The normal component of the magnetic field, which is contributed from the **z** component of the surface electric field in equation (10), can be obtained from:

$$H_n|_{\partial S} \simeq \frac{j}{\mu_c \omega}\frac{\partial E_z}{\partial l}|_{\partial S} = \frac{Z_s k_z}{\mu_c \omega k_{c0}^2}\frac{\partial^2 H_{z0}}{\partial l^2}|_{\partial S} \tag{6.7}$$

As a result, the perturbation condition generated by equation (6.7) is obtained:

$$N(E_n) = \frac{1}{Z_s \cdot \sigma} \frac{k_{z0}^2}{k_{c0}^2} \frac{\partial^2 H_{z0}}{\partial l^2} |_{\partial S} \tag{6.8}$$

Then, by using the two-dimensional Green theorem, we can treat the lossless field and the first perturbation as follow:

$$\oint_S H_{z0} \nabla_t^2 H_z - H_z \nabla_t^2 H_{z0} dS = \oint_{\partial S} H_z \frac{\partial H_{z0}}{\partial n} - H_{z0} \frac{\partial H_z}{\partial n} dl \tag{6.9}$$

From equation (6.10) and Helmholtz equation (6.2), (6.3), we obtain:

$$(k_{c0}^2 - k_c^2) \int_S H_{z0} H_z dS = \int_{\partial S} H_z \frac{\partial H_{z0}}{\partial n} - H_{z0} \frac{\partial H_z}{\partial n} dl \tag{6.10}$$

We can ignore the first term on the right side of the equation (6.10).

Then by substituting equations (6.3), (6.6), and (6.8) in (6.10), the right side of (6.10) becomes:

$$\int_{\partial S} -H_{z0} \frac{\partial H_z}{\partial n} dl = \frac{1}{Z_s \sigma} \int_{\partial S} \left(\omega^2 \mu \epsilon \frac{\mu_c}{\mu} |H_{z0}|^2 - \frac{k_{z0}^2}{k_{c0}^2} H_{z0} \frac{\partial^2 H_{z0}}{\partial l^2} \right) dl \tag{6.11}$$

Since the H_{z0} is a sinusoid function in terms of $\boldsymbol{l}$, we have the following relation:

$$H_{z0}\frac{\partial^2 H_{z0}}{\partial l^2} = -|\frac{\partial H_{z0}}{\partial l}|^2 \tag{6.12}$$

Then by substituting (6.12) into (6.11), we finally obtain:

$$\int_{\partial S} -H_{z0}\frac{\partial H_z}{\partial n}\,dl = \frac{1}{Z_c\sigma}\int_{\partial S}\left(\omega^2\mu\epsilon\frac{\mu_c}{\mu}|H_{z0}|^2 + \frac{k_{z0}^2}{k_{c0}^2}\left|\frac{\partial H_{z0}}{\partial l}|^2\right)\right) dl \tag{6.13}$$

Notice that two coefficients of equation (6.13) are far smaller than 1, so we can replace the H_z by H_{z0} to calculate the left side of equation (6.10):

$$(k_{c0}^2 - k_c^2)\int_S H_{z0}\,H_z dS = (k_{c0}^2 - k_c^2)\int_S |H_{z0}|^2\,dS \tag{6.14}$$

Consequently, we obtain the following equation:

$$k_{z0}^2 - k_z^2 = k_{c0}^2 - k_c^2$$

$$= 2(1-j)k_{z0}\frac{1}{Z_c\sigma}\frac{\int_{\partial S}\left(\omega^2\mu\epsilon\frac{\mu_c}{\mu}|H_{z0}|^2 + \frac{k_{z0}^2}{k_{c0}^2}\left|\frac{\partial H_{z0}}{\partial l}|^2\right)\right) dl}{\int_S |H_{z0}|^2\,dS} \tag{6.15}$$

$$= 2(1-j)k_{z0}\xi$$

Finally, we can obtain the transmission constant with first order perturbation modification:

$$k_z = \beta - j\alpha = \sqrt{k_{z0}(k_{z0} + 2\xi) - 2j\xi k_{z0}} \qquad (6.16)$$

where the α is attenuation constant and β is phase constant.

We plot α as a function of normalized angular frequency ω/ω_c, where ω_c is the cutoff angular frequency [see Fig. 6.6(a)]. With decreasing the waveguide width, we find the loss is increased from 0.52 dB/m (for a standard WR-28 waveguide) to 0.74 dB/m for a waveguide with a 5-mm waveguide width, as illustrated in Fig. 6.6(b).

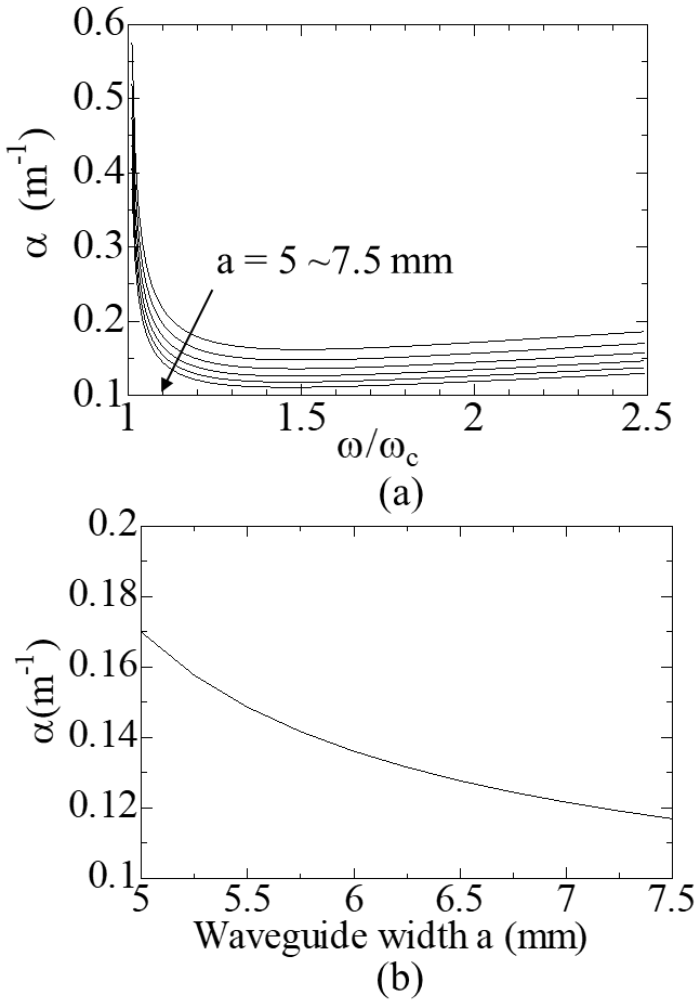

Fig. 6.6. transmission loss α of rectangular waveguide as a function of (a) normalized frequency ω/ω_c, where ω is angular frequency and ω_c is cutoff angular frequency. The material of waveguide is copper. (b) wide wall width a at 38 GHz.

6.4 Summary

This chapter delves into a comprehensive investigation of slotted waveguide applications through three distinctive case studies, each contributing valuable insights to the advancement of this technology.

1. Inclined Stair for Enhanced Tolerance: The first case study explores the application of inclined stairs in slotted waveguide design. This innovative approach serves to elevate processing tolerance, addressing challenges associated with fabrication precision. By incorporating inclined stairs, the study demonstrates a notable improvement in processing tolerance, showcasing the potential for this technique to enhance manufacturing feasibility.

2. Circular Array Performance: The second case study focuses on the performance of circular slotted waveguide arrays. Comparing these arrays to their rectangular counterparts, the study highlights the superior symmetry inherent in circular arrays. This inherent symmetry proves advantageous in mitigating side lobes, particularly when compared to rectangular configurations. The findings underscore the potential of circular slotted waveguide arrays in achieving enhanced performance through improved radiation characteristics.

3. Perturbated Boundary Conditions for Transmission Loss Analysis: The third case study employs perturbated boundary conditions to scrutinize transmission losses in slotted waveguides. Specifically, the study investigates the transmission loss in a 5-mm copper waveguide at 38 GHz. Conclusive results indicate that, within this frequency domain, the transmission loss for the specified waveguide size is negligible. The study establishes the viability of perturbated boundary conditions for accurately assessing transmission losses in slotted waveguides operating at 38 GHz.

Collectively, these case studies contribute to a nuanced understanding of slotted waveguide applications. The exploration of inclined stairs for improved tolerance, the performance evaluation of circular arrays, and the analysis of transmission losses through perturbated boundary conditions collectively advance our comprehension of slotted waveguide intricacies. These insights are crucial for enhancing the design, fabrication, and performance of slotted waveguides, particularly in the context of applications operating at 38 GHz.

6.5 References

[6.1] W. Liu and Y. Tsunemitsu, "Slotted waveguide antenna with inclined stairs for effective side lobes suppression at 38 GHz," 2021 15th European Conference on Antennas and Propagation (EuCAP), Dusseldorf, Germany, 2021, pp. 1-3, doi: 10.23919/EuCAP51087.2021.9411506.

[6.2] J. Xu, W. Hong, Z. H. Jiang, and H. Zhang, "Low-profile circular patch array fed by slotted substrate integrated waveguide," IEEE Transactions on Antennas and Propagation, vol. 67, no. 2, pp. 960-970, 2018.

[6.3] S. Marini et al., "Improved computation of propagation losses in waveguide structures using perturbation of boundary conditions," IEEE Microwave and Wireless Components Letters, vol. 21, no. 11, pp. 577-579, 2011.

[6.4] S. Marini et al., "Advanced analysis of propagation losses in rectangular waveguide structures using perturbation of boundary conditions," 2011 IEEE MTT-S International Microwave Workshop Series on Millimeter Wave Integration Technologies, IEEE, 2011.

Chapter 7 Conclusion and prospective research

7.1 Conclusion of this work

In conclusion, this paper presented a simulation and experimental study on a waveguide slotted array antenna with RCSs for sidelobe suppression at 38 GHz. The main objective of the study was to improve the aperture efficiency of the antenna. Two optimization methods were employed: the use of RCSs to minimize reflection and the optimization of the broad wall width and slot offset to suppress grating lobes. The design procedure for the feed part of the antenna was also presented.

The proposed antenna design experimentally achieved a measured S11 of less than -20 dB and a gain of more than 27.71 dBi at 38 GHz, corresponding to an aperture efficiency of 85.6%. These results were in good agreement with the simulation results, confirming the feasibility of using the proposed antenna in millimeter-wave communication systems.

7.2 Prospective research

As we conclude this doctoral research on slotted waveguide antenna arrays, it is essential to look ahead and identify key factors that will drive and enhance the impact of this study in the future. Three major factors are poised to significantly influence and propel further advancements in the realm of slotted waveguide antennas.

1. Advancements in Manufacturing Technology: The continuous evolution and enhancement of manufacturing technologies, particularly the burgeoning field of 3D printing, hold immense promise for the fabrication of antennas. The utilization of 3D printing techniques in antenna manufacturing can revolutionize the production process, allowing for intricate and customized designs that were previously challenging to achieve. This technological improvement is anticipated to streamline the manufacturing of slotted waveguide antenna arrays, fostering greater precision and efficiency in the production phase.

2. Computational Capabilities for Complex Design: The ongoing improvements in computer software and hardware performance are instrumental in unlocking new frontiers for antenna design. Higher computational capabilities empower researchers to delve into more complex and intricate designs, enabling the exploration of innovative configurations and patterns. This enhanced computational prowess will be invaluable for optimizing the performance of slotted waveguide antenna arrays, pushing the boundaries of what is achievable in terms of efficiency and functionality.

3. Escalating Application Demand at 38 GHz: The increasing demand for applications operating at 38 GHz represents a pivotal factor propelling the relevance and significance of slotted waveguide antenna arrays. As the need for high-frequency communication systems and radar applications continues to surge, the unique capabilities offered by slotted waveguide antennas make them indispensable in addressing the challenges posed by this frequency range. This growing application demand positions the research conducted in this study at the forefront of meeting the evolving needs of modern communication and sensing systems.

In essence, the convergence of improved manufacturing techniques, enhanced computational capabilities, and escalating application demands at 38 GHz forms a compelling trifecta that will amplify the impact of slotted waveguide antenna arrays. Embracing and capitalizing on these advancements will undoubtedly pave the way for future breakthroughs, ensuring that this research remains at the forefront of innovation in the dynamic field of antenna technology.

Appendix:

App. I: Integral of an important function for dipole antenna radiation

The (I.1) is an essential integral to derive the antenna radiation pattern.

$$I = \int_{-L}^{L} \sin[\mathrm{k}(\mathrm{L}+\mathrm{z})] e^{-ikzcos\theta} dz \tag{I.1}$$

First, we try to solve the problem below:

$$J = \int sin(\alpha + \beta \mathrm{z}) \cdot e^{\gamma z} dz \tag{I.2}$$

By using the following Euler equation:

$$e^{\mathrm{i}\cdot(\alpha+\beta \mathrm{z})} = cos(\alpha + \beta \mathrm{z}) + i \cdot sin(\alpha + \beta \mathrm{z}) \tag{I.3}$$

We obtain that:

$$L = e^{i\alpha} \int e^{(i\beta+\gamma)z} dz \tag{I.4}$$

Then we have the relation that:

$$J = Im(L) \tag{I.5}$$

Besides, we can calculate the value of J as follows.

$$L = e^{i\alpha} \cdot \frac{1}{i\beta + \gamma} \cdot e^{(i\beta+\gamma)z} \tag{I.6}$$

By organizing the equation I.6 as a proper format, we obtain the following:

$$L = e^{\gamma z} \frac{\gamma - i\beta}{\beta^2 + \gamma^2} \cdot [cos(\alpha + \beta z) + i \cdot \sin(\alpha + \beta z)] \tag{I.7}$$

As a result, the imaginary part of L can be denoted as follows:

$$J = Im(L) = \frac{e^{\gamma z}}{\beta^2 + \gamma^2} \cdot [\gamma \cdot \sin(\alpha + \beta z) - \beta \cos(\alpha + \beta z)] \tag{I.8}$$

By substituting the detail formula of the coefficient α, β and γ, we can get the solution of the original problem (I.1).

Here the coefficients are:

$$\alpha = kL \tag{I.9.1}$$

$$\beta = k \tag{I.9.2}$$

$$\gamma = -ikcos\theta \tag{I.9.3}$$

Then we substitute all the three parameters (I.9) into (I.8). consequently, we can obtain the solution of the original problem:

$$I = \frac{e^{-ikcos\theta z}}{k^2 \sin^2\theta}[-ikcos\theta \sin(\alpha + \beta z) - kcos(\alpha + \beta z)] \tag{I.9.4}$$

Notice that this integral is essential for basic dipole antenna radiation derivation. However, in almost every reference, the detailed deriving process is missing. It is trivial but not intuitive, especially for the audience who are not familiar with the integral calculation. Thus, we give the explanation in this appendix.

App. II: Python code for perturbated boundary condition loss estimation

```
import numpy as np
from numpy import sin,cos
from numpy import pi
from numpy import exp,log,log10
a = 5 # mm
b = 3.556 # mm
miu_c = 1.256629e-6
miu = 1.2566370614e-6
epsilon = 8.854187817e-12
c = 1/(miu*epsilon)**0.5
fc = c/2/a
fc = fc*1e-6
f = 38
a = a*1e-3 # m
b = b*1e-3 # m
f = f *1e9    # Hz
omega = 2*pi*f   # rad/s
sigma = 59.5e6  #Cupper
delta = (2/miu_c/sigma/omega)**0.5
# TE10
m = 1
n = 0
```

```
kx = m*pi/a
ky = n*pi/b
k = omega*(miu*epsilon)**0.5
kc0 = (kx**2+ky**2)**0.5
gamma0 = k**2 - kc0**2
def Hz(x,y):
   return sin(kx*x)*cos(ky*y)
N = 100
x = np.arange(0,a,a/N)
y = np.arange(0,b,b/N)
dx = a/N
dy = b/N
I1 = 0
for i in x:
   I1 += 2*omega**2*miu*epsilon*(abs(Hz(i,0))**2*dx)
for i in y:
   I1 += 2*omega**2*miu*epsilon*(abs(Hz(0,i))**2*dy)
for i in range(len(x)-1):
   I1 += 2*gamma0**2/kc0**2*abs((Hz(x[i+1],0)-Hz(x[i],0))/dx)**2*dx
for i in range(len(y)-1):
   I1 += 2*gamma0**2/kc0**2*abs((Hz(0,y[i+1])-Hz(0,y[i]))/dx)**2*dx
I2 = 0
```

```
ds = a*b/N/N
for i in x:
    for j in y:
        I2 += abs(Hz(i,j))**2*ds
ksi = delta/4/gamma0*I1/I2   # use summation to calculate integral approxiamtely
gamma = (gamma0*(gamma0+2*ksi)-2j*ksi*gamma0)**0.5
gamma_sqr = gamma**0.5
alpha = -1*gamma_sqr.imag
```

App. III: Manufacturing drawings

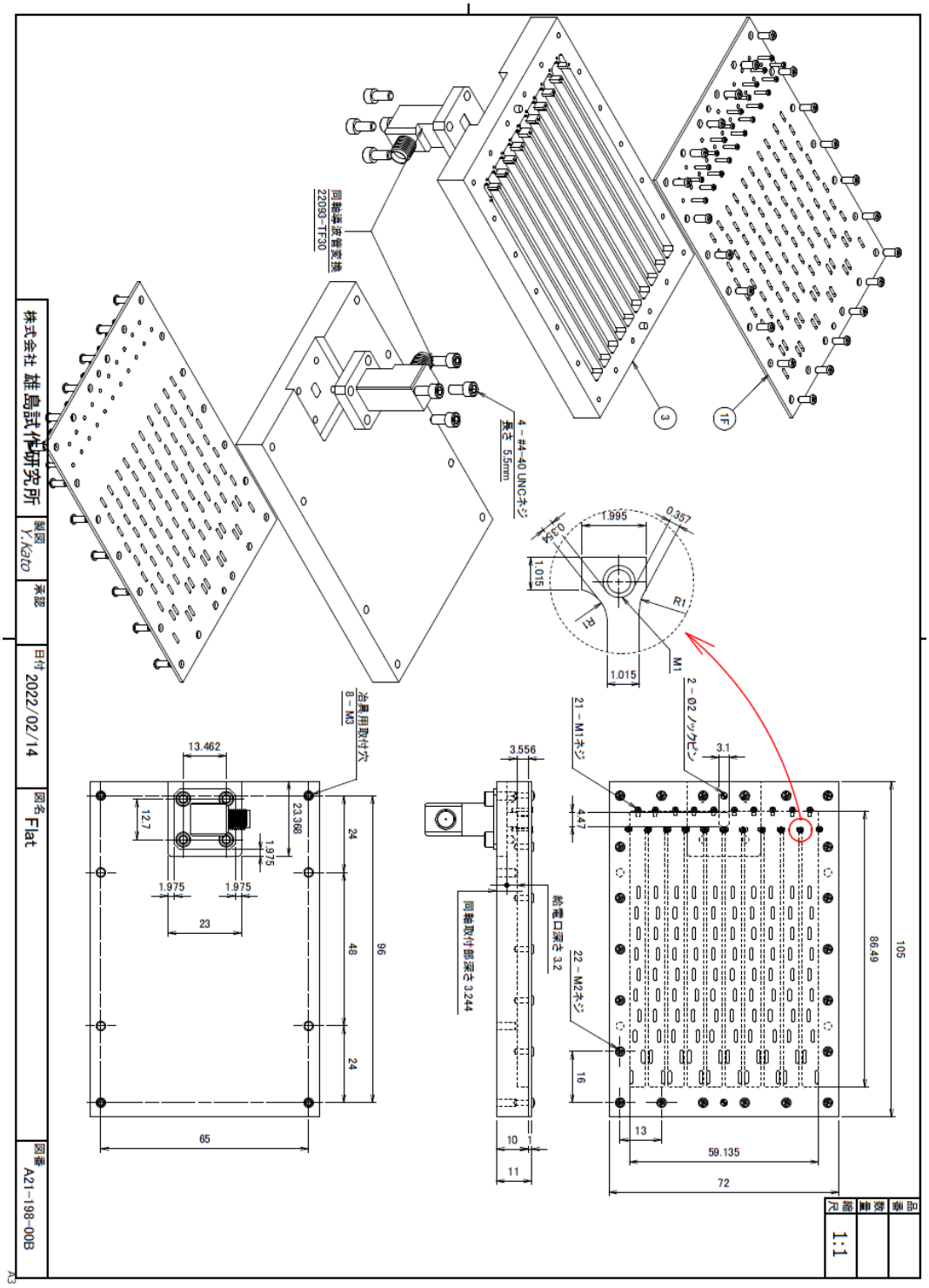

Appendix

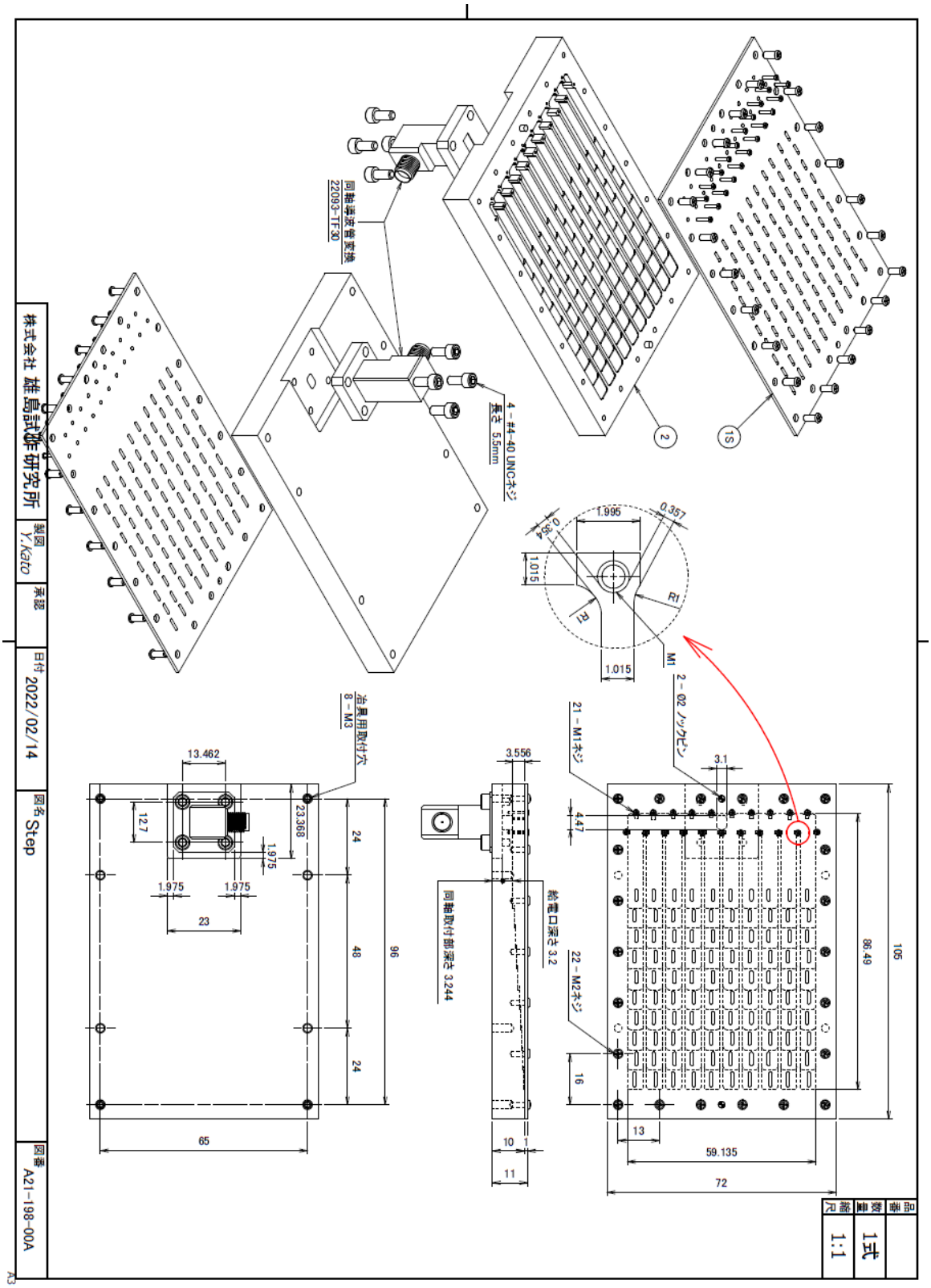
株式会社 雄島試作研究所
製図 Y.Kato
承認
日付 2022/02/14
図名 Step
図番 A21-198-00A
A3
同軸導波管変換
2203-TF30
4 - #4-40 UNCネジ
長さ 5.5mm
2
1S
1.995
0.357
1.015
R1
R2
M1
2 - Ø2 ノックピン
治具用取付穴
8 - M3
21 - M1ネジ
22 - M2ネジ
3.556
3.1
4.47
13.462
23.368
127
1.975
23
24
48
96
65
同軸取付部深さ 3.244
給電口深さ 3.2
86.49
105
16
13
59.135
72
10
11
加工
軸数 1式
縮尺 1:1
品番

App. IV. 3-D radiation patterns

Section 1:5-mm with RCS

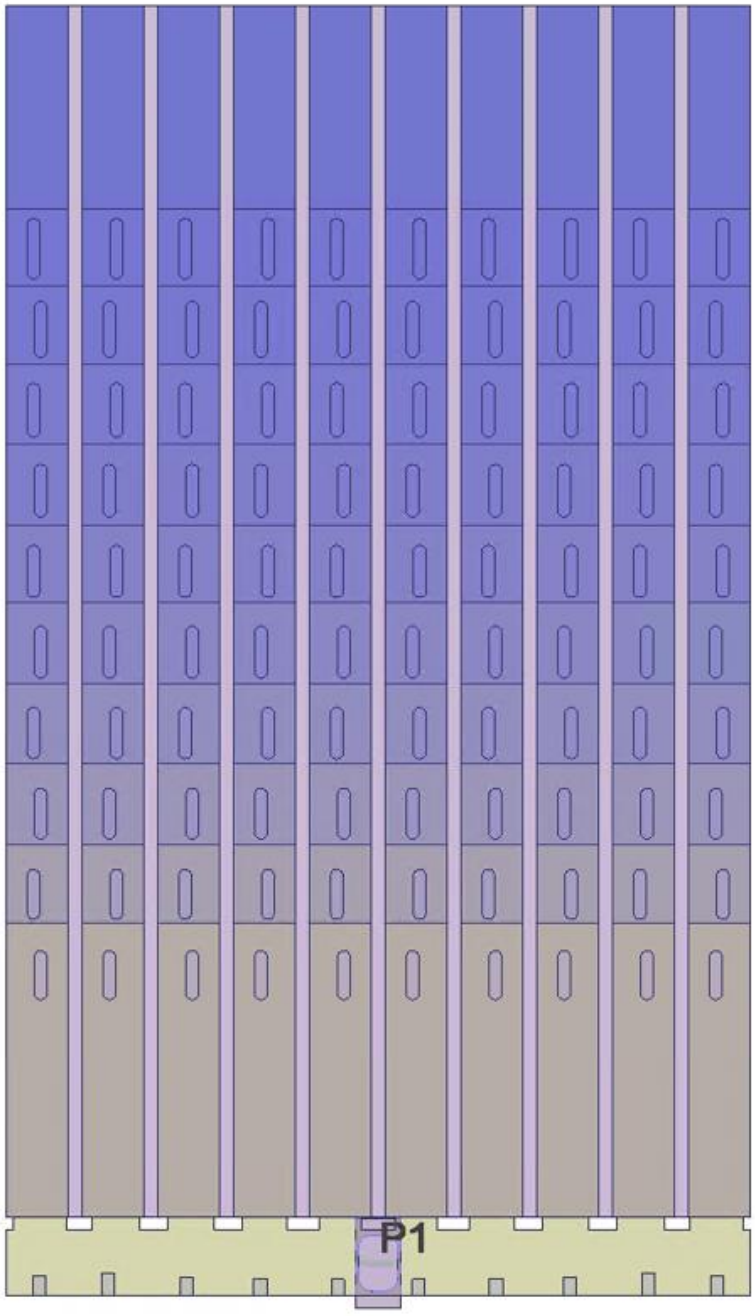

Appendix

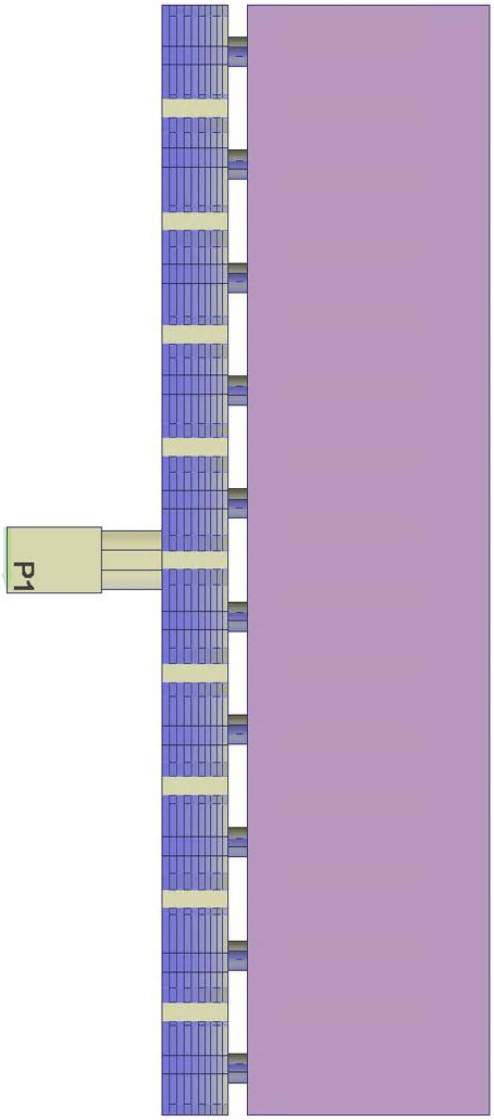

Appendix

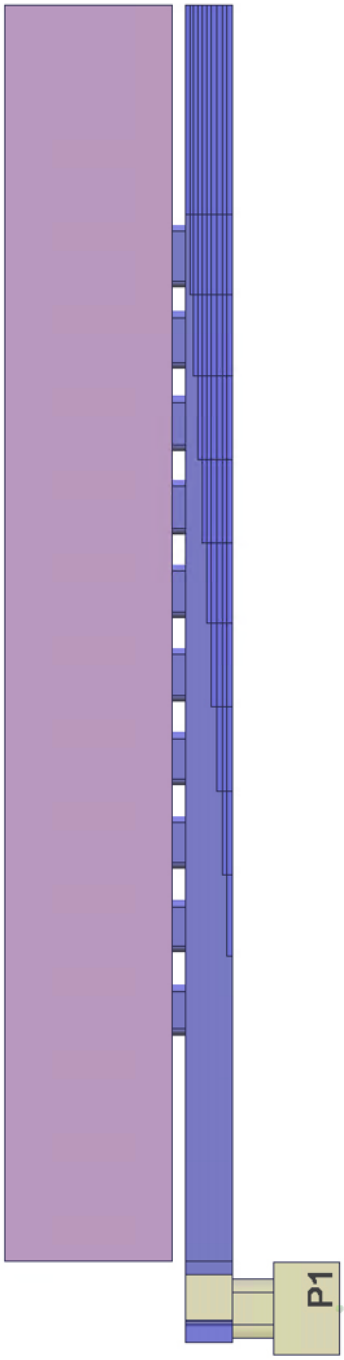

Appendix

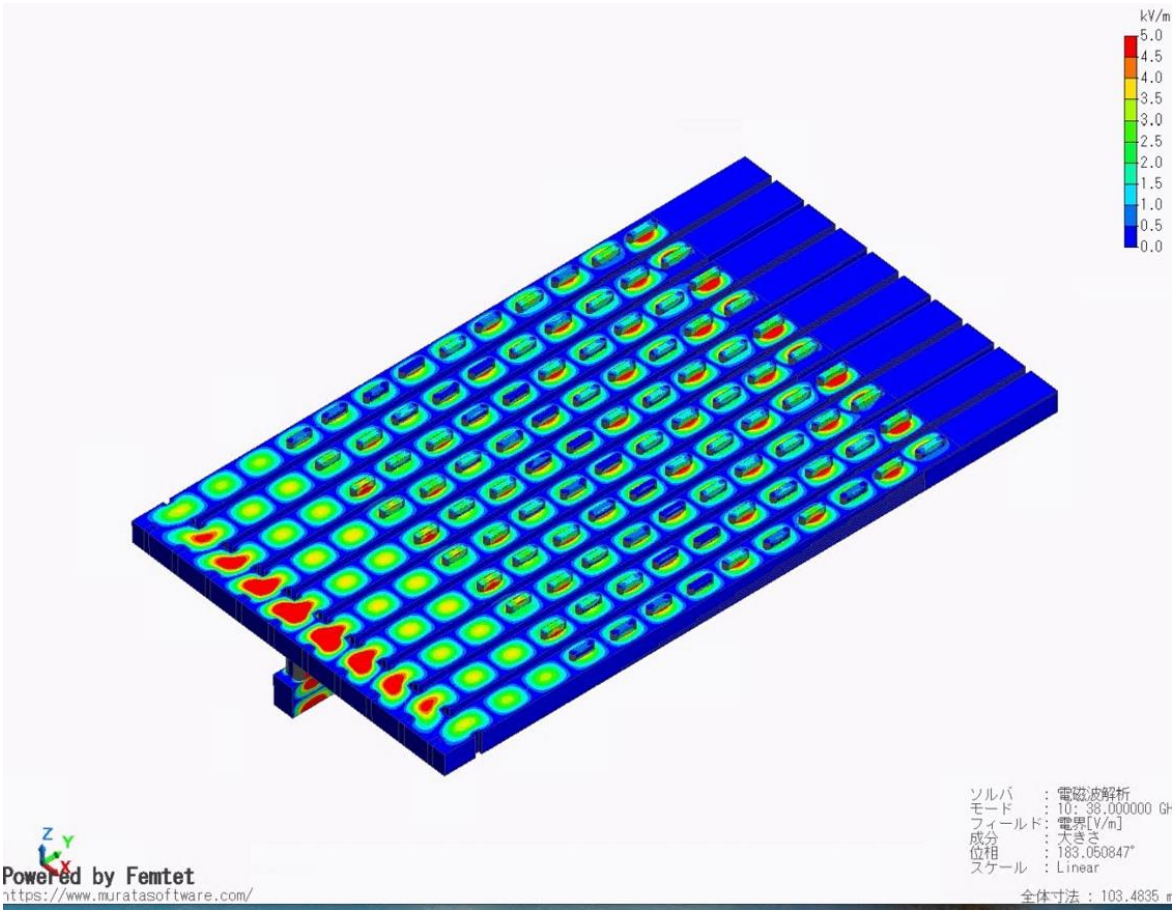
kV/m
5.0
4.5
4.0
3.5
3.0
2.5
2.0
1.5
1.0
0.5
0.0
ソルバ : 電磁波解析
モード : 10: 38.000000 GH
フィールド: 電界[V/m]
成分 : 大きさ
位相 : 183.050847°
スケール : Linear
全体寸法 : 103.4835 m
Z Y X
Powered by Femtet
https://www.muratasoftware.com/

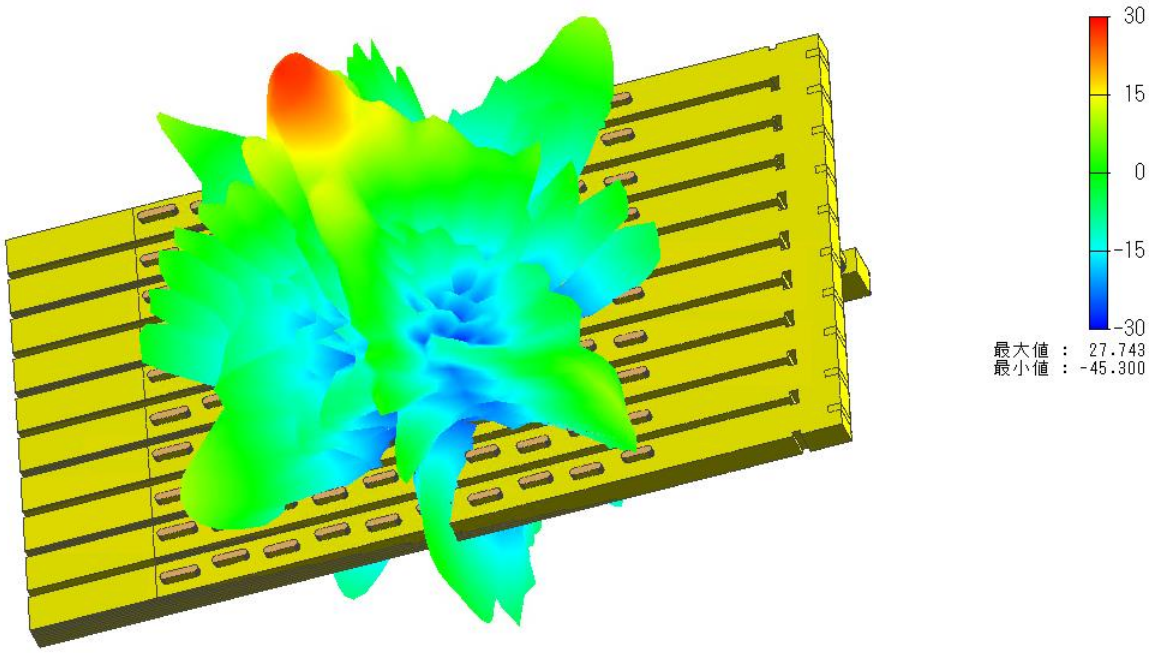

Pmax = 27.743 dBi

Section 2: 5-mm without RCS

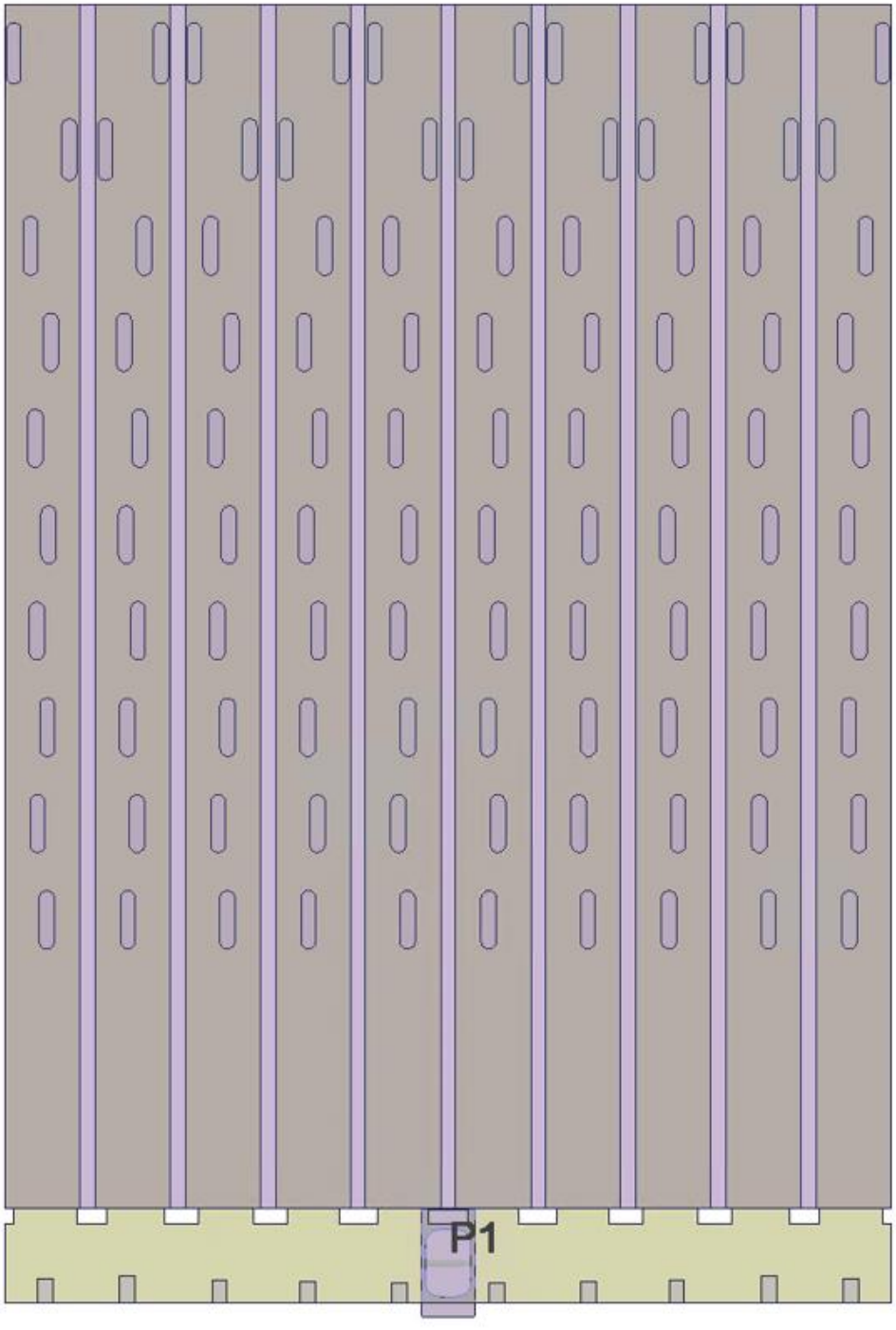

Appendix

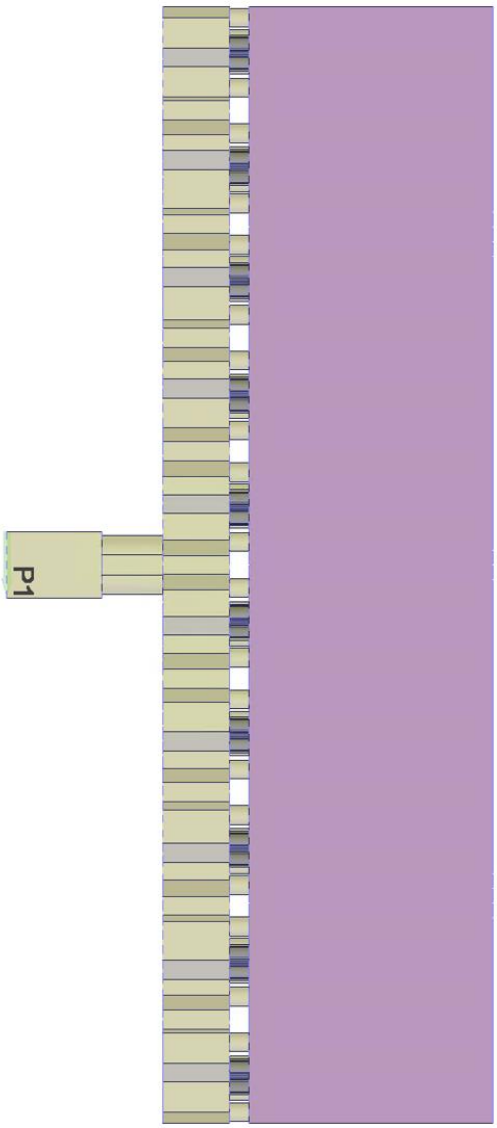

Appendix

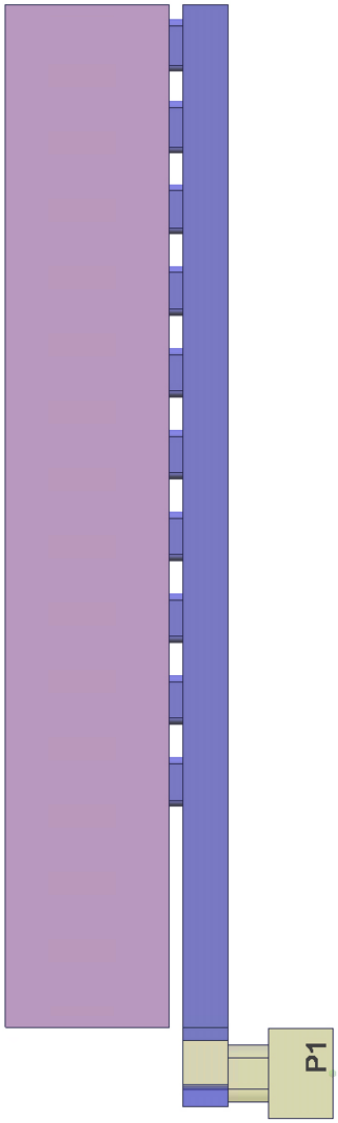

Appendix

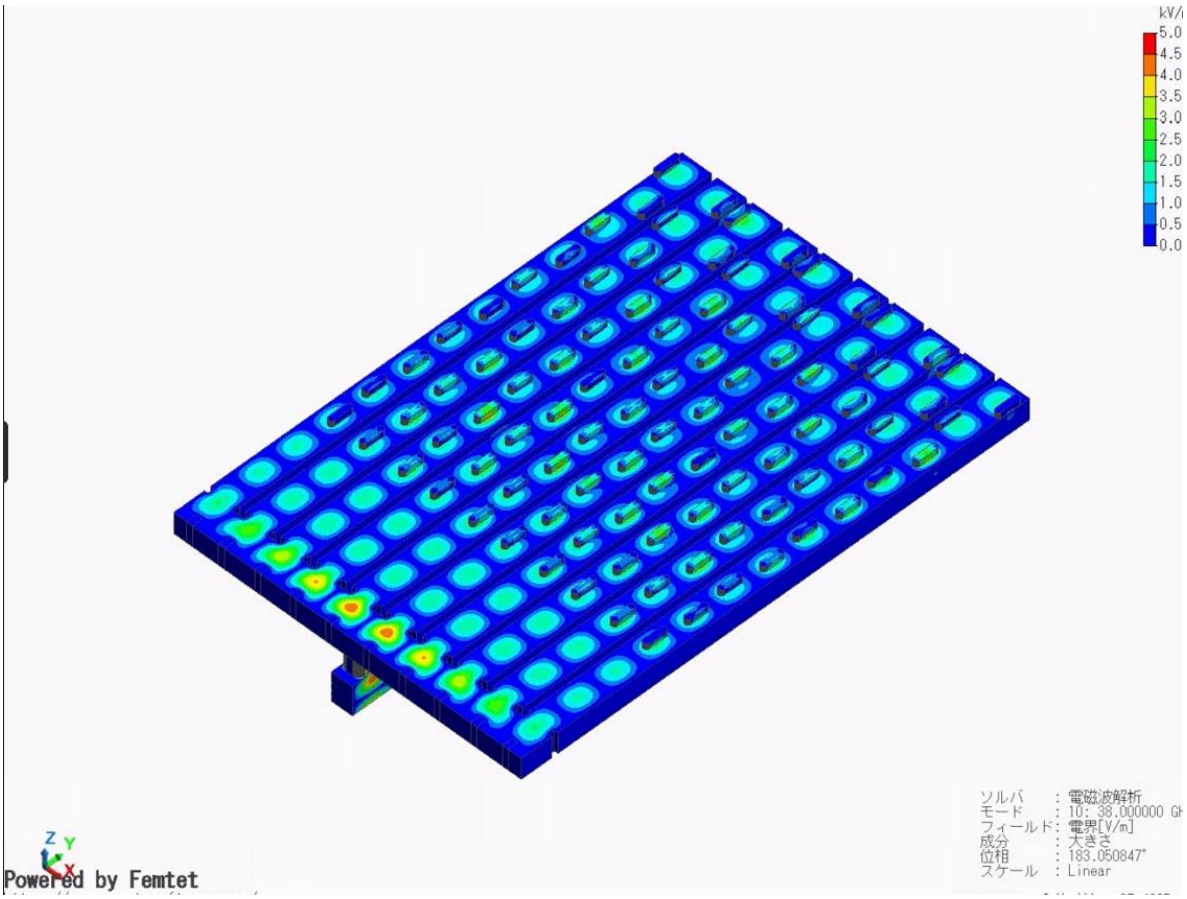
kV/
5.0
4.5
4.0
3.5
3.0
2.5
2.0
1.5
1.0
0.5
0.0
ソルバ : 電磁波解析
モード : 10: 38.000000 GH
フィールド: 電界[V/m]
成分 : 大きさ
位相 : 183.050847°
スケール : Linear
Z Y
X
Powered by Femtet

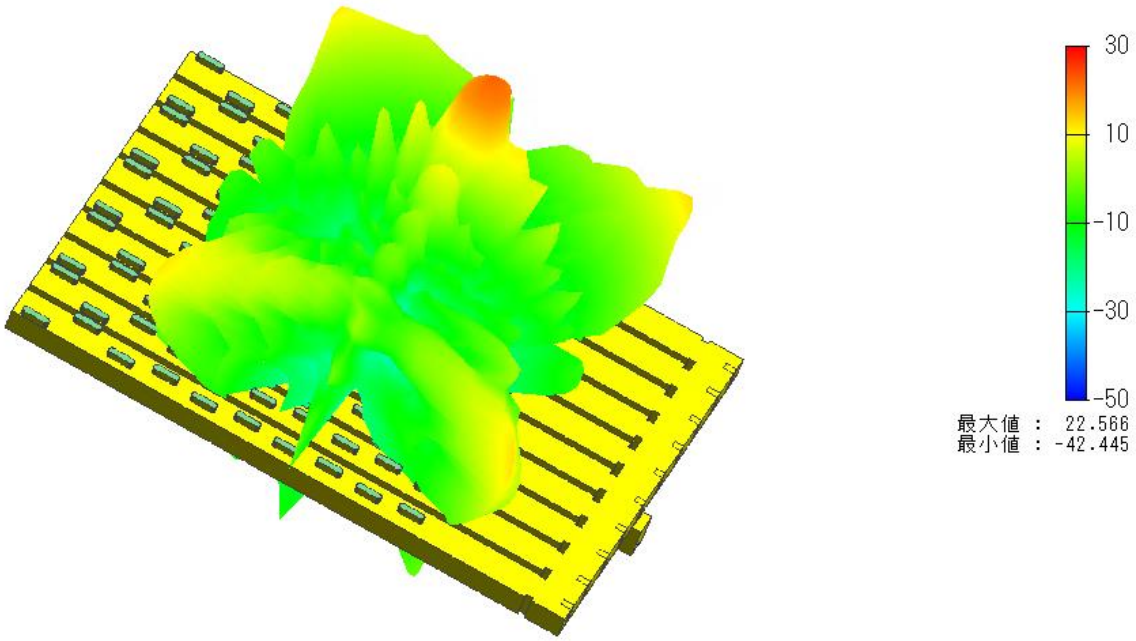

Pmax = 22.566 dBi

Section 3: 7.112-mm with RCS

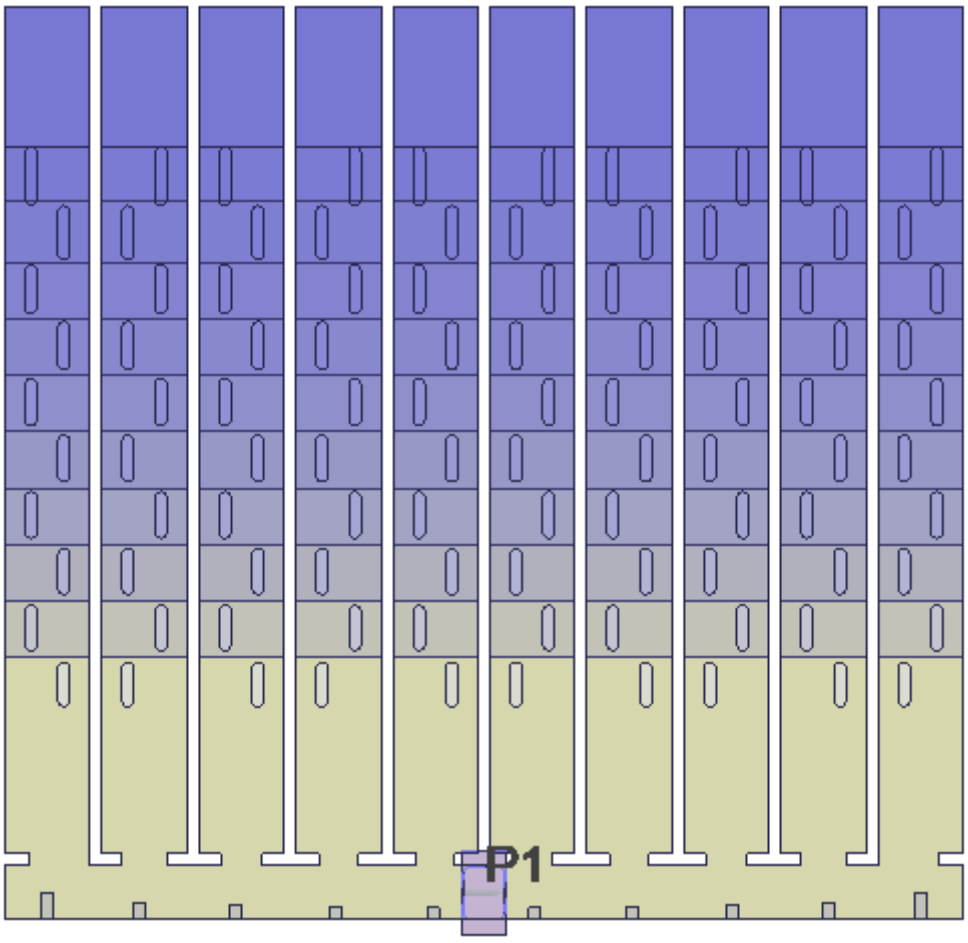

Appendix

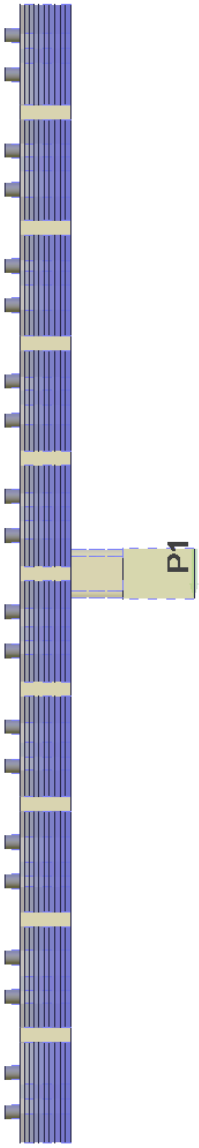

Appendix

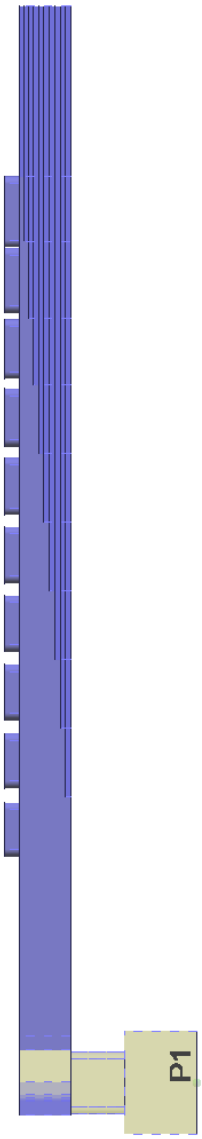

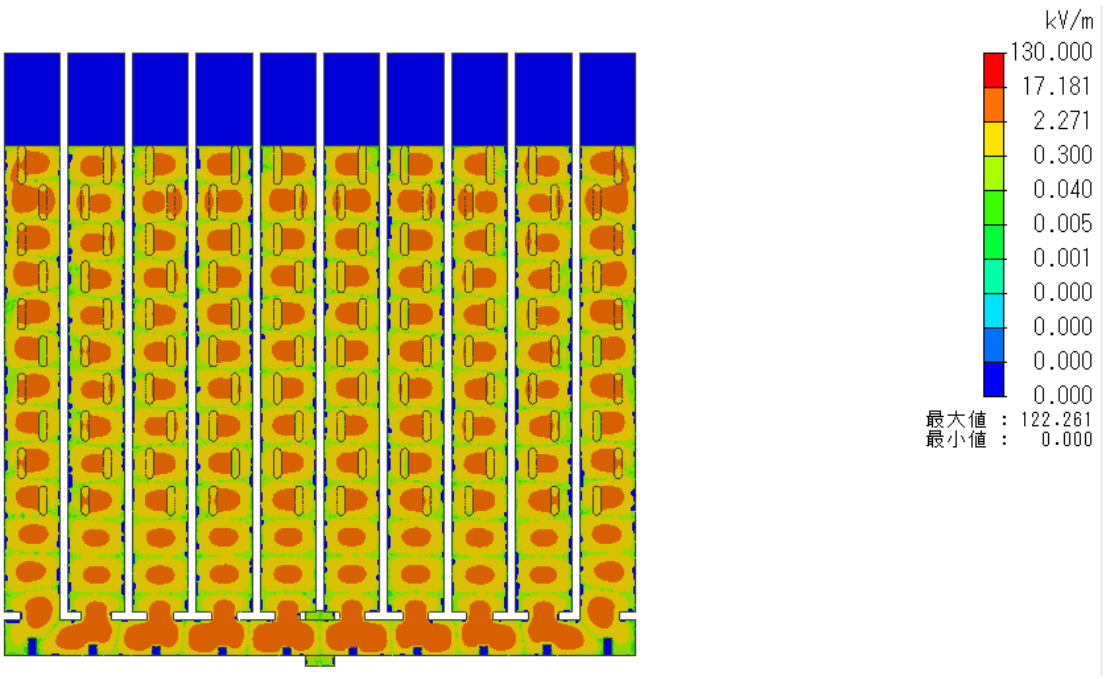
kV/m
130.000
17.181
2.271
0.300
0.040
0.005
0.001
0.000
0.000
0.000
0.000
最大値 : 122.261
最小値 : 0.000

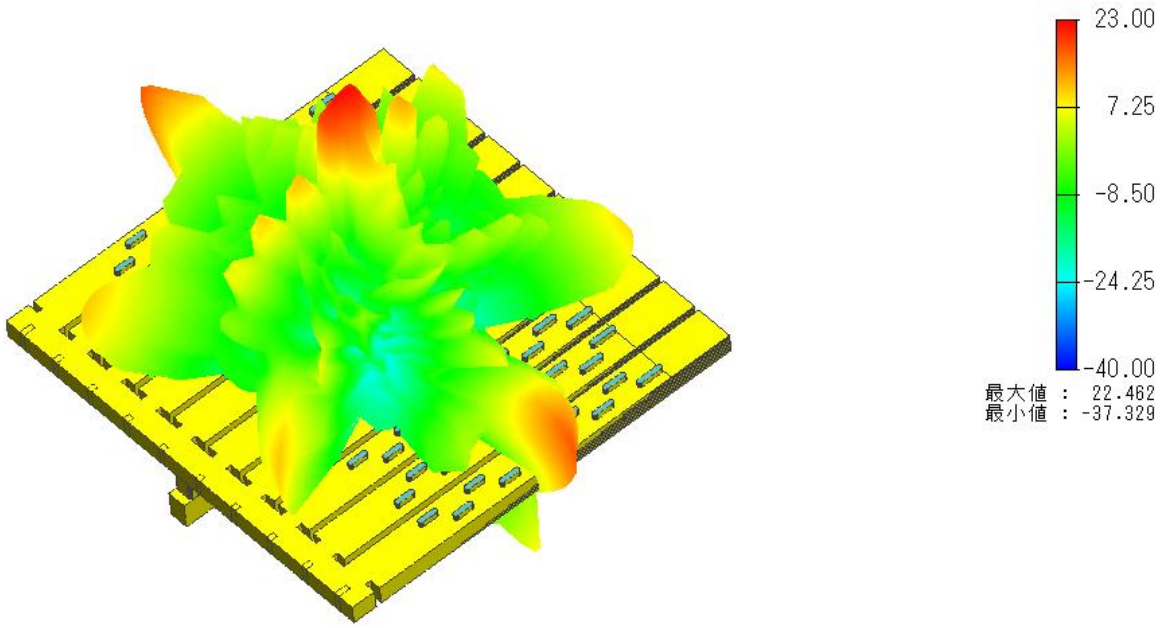

Pmax = 22.462 dBi

Section IV: the mode patten of fed part

Input aperture:

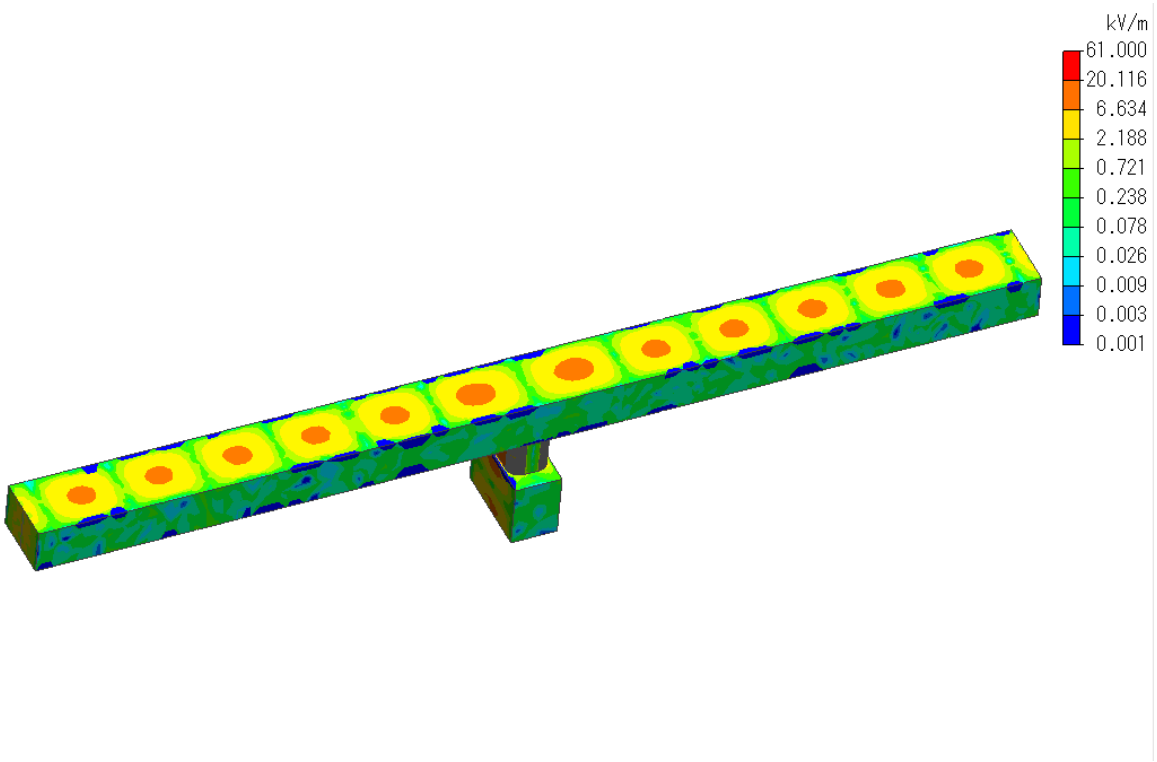

Appendix

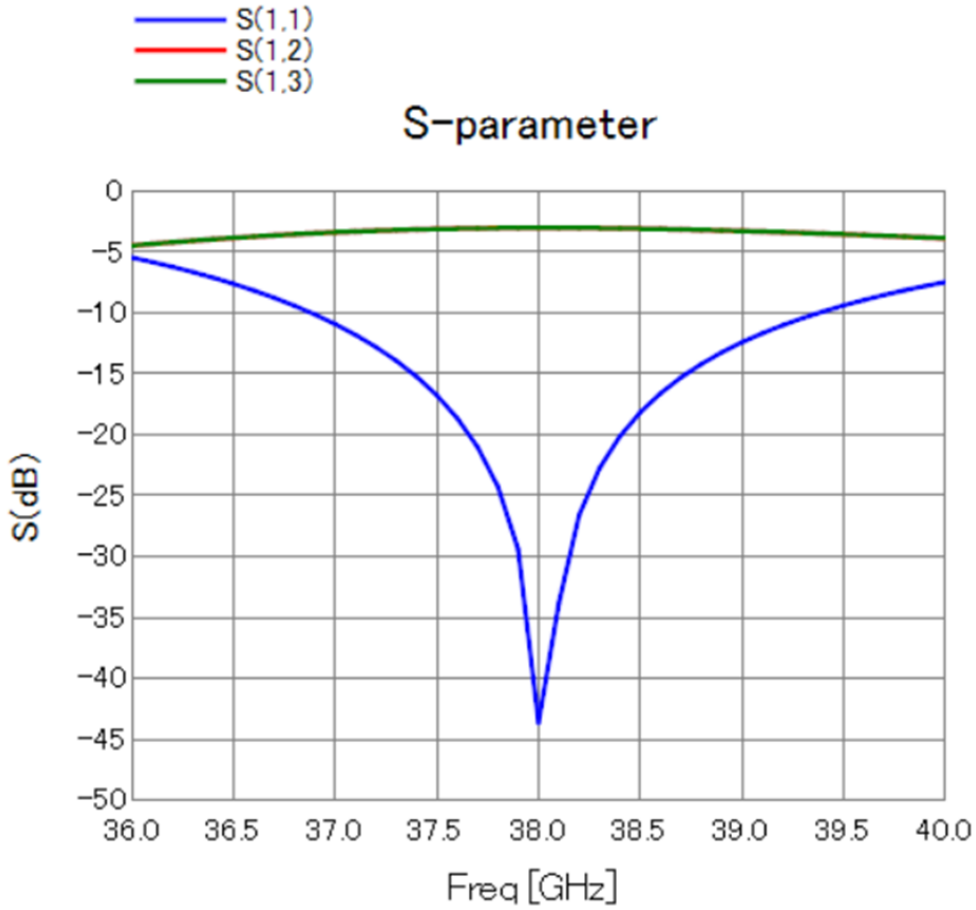
S(1,1)
S(1,2)
S(1,3)
S-parameter
S(dB)
0
-5
-10
-15
-20
-25
-30
-35
-40
-45
-50
36.0
36.5
37.0
37.5
38.0
38.5
39.0
39.5
40.0
Freq [GHz]

Feeding waveguide array:

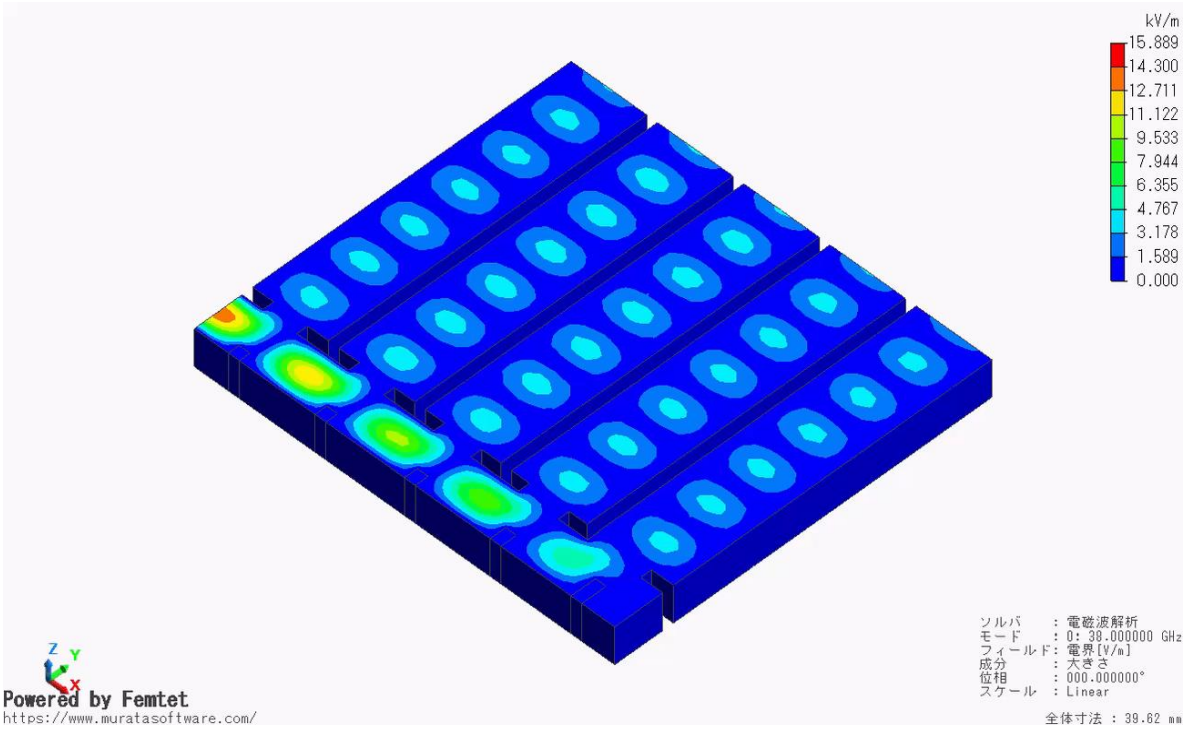

Section V: linear waveguide design result

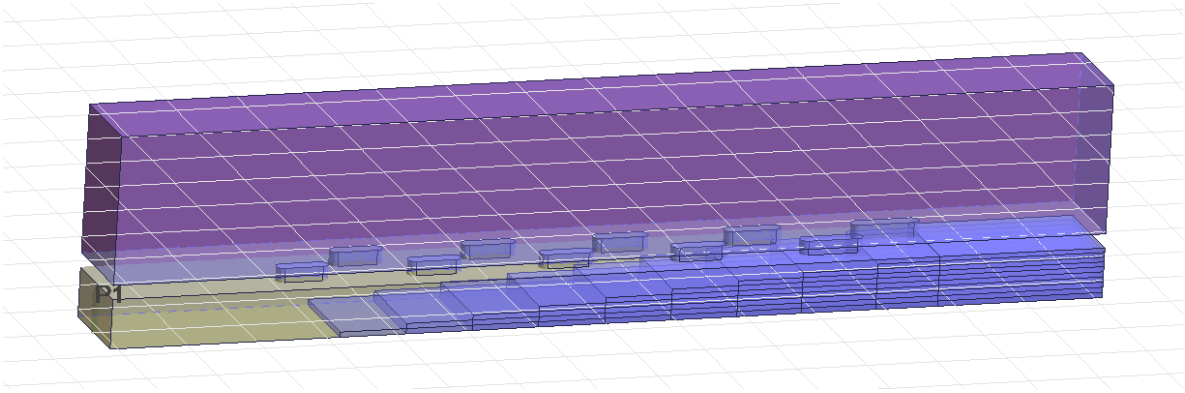

Appendix

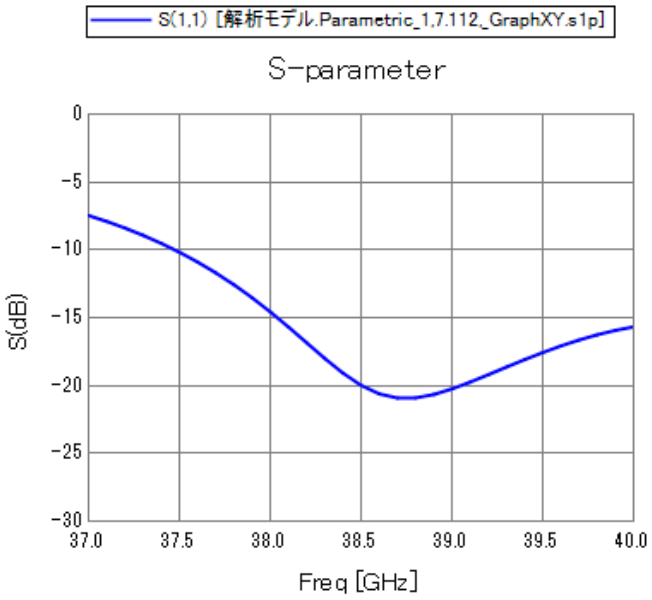
S(1,1) [解析モデル.Parametric_1.7.112_GraphXY.s1p]
S-parameter
S(dB)
0
-5
-10
-15
-20
-25
-30
37.0
37.5
38.0
38.5
39.0
39.5
40.0
Freq [GHz]

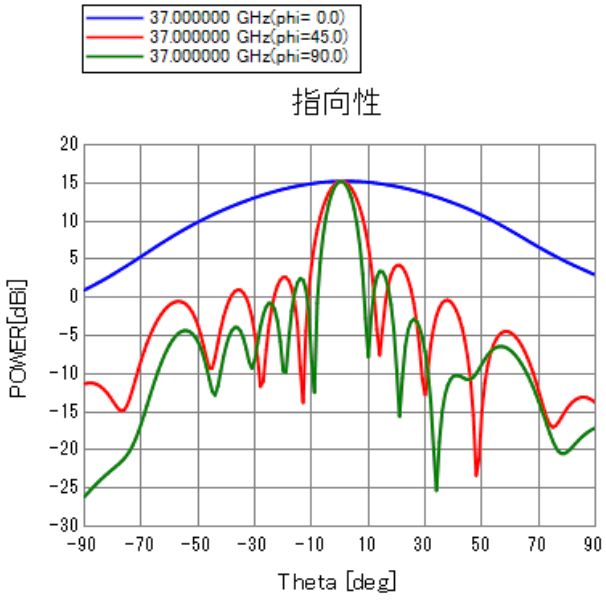
37.000000 GHz(phi= 0.0)
37.000000 GHz(phi=45.0)
37.000000 GHz(phi=90.0)
指向性
POWER[dBi]
20
15
10
5
0
-5
-10
-15
-20
-25
-30
-90
-70
-50
-30
-10
10
30
50
70
90
Theta [deg]

App. V Supplement data plot for simulation

As we described in chapter 4, we have simulated all the 4 types of devices. Here, in this section, we give some additional data plot.

Section I: single waveguide

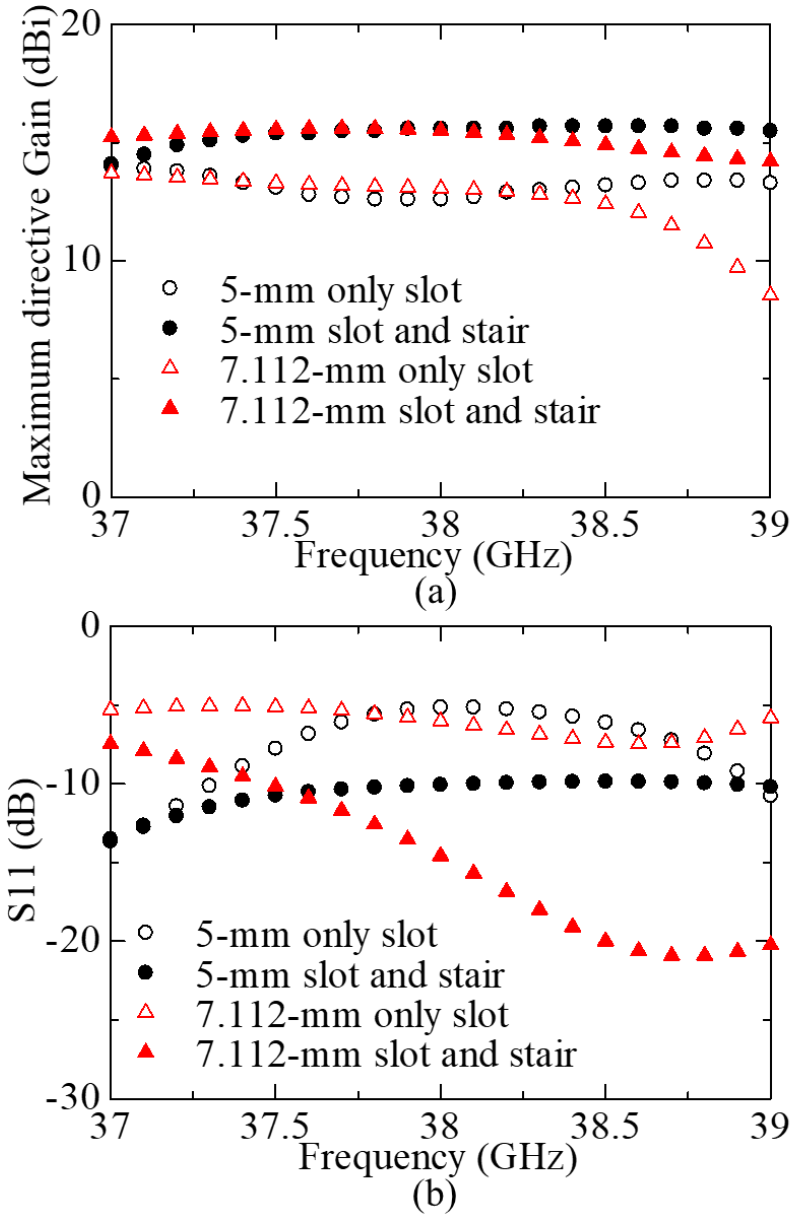

Fig. 1. (a) maximum bore-sight directive gain and (b) reflection (|S11|) of single waveguide as a function of frequency.

Section II: 10x10 array

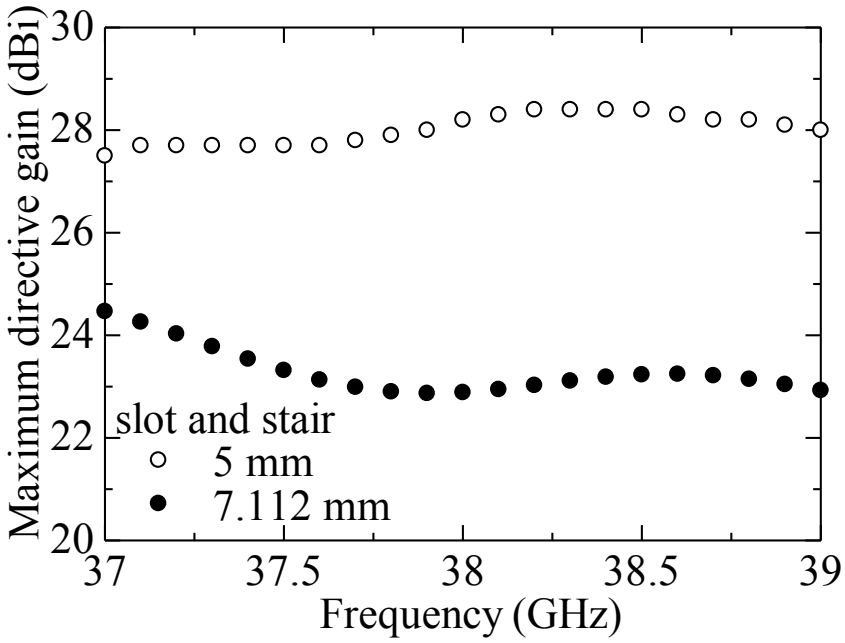

Fig. 2. Maximum bore-sight directive gain of 10 x 10 array as a function of frequency. reflection canceling stairs are employed in both cases.

Section III: Entire model:

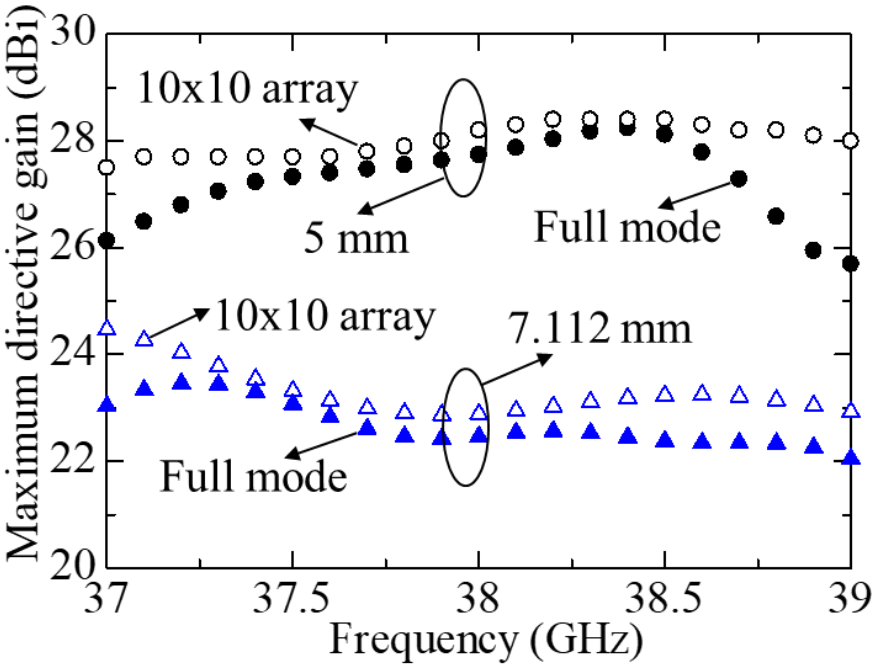

Fig. 3. Maximum bore-sight directive gain as a function of frequency.

App. VI: Procedure to make model in Femtet

The entire default space without any geometry structure is ideal conductor. The users are supposed to draw geometry structures with dielectric or air and then set boundary conditions or port conditions.

To this end, to build a model of slotted waveguide in Femtet is to build the air boundary that contained inside a slotted waveguide.

First, we need to build a rectangular prism. Six parameters determine a prism, the initial point coordinates (x, y, z) and the width, height and length (a, h, l). For simplicity, we usually set that $(x, y, z) = (-\frac{a}{2}, 0,0)$, where the line $x = 0$ is the axis of the rectangular. The following example shows that how to draw a prism in our desire position.

Example I: To build the rectangular in the red rectangular. We know that the slotted waveguide parameters $(a,,h,l)$, the slot parameters (ls,lo). Besides the rectangular waveguide is made by the method previously, where x=0 is the center axis. And we assume that the thickness and width of the slot are t and 1, while the first slot has $\frac{3}{2}\cdot\lambda_g$.

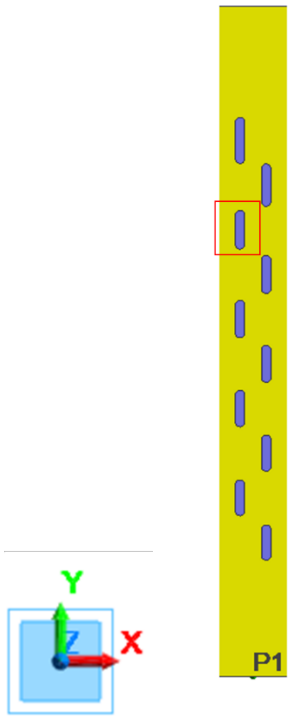

Fig. 1.

To this end, we can first calculate the coordinates of the initial point of this rectangular.

$$(x,y,z)=(-lo-\frac{1}{2},\left(\frac{7}{2}+\frac{3}{2}\right)\cdot\lambda_g-\frac{ls}{2},h) \qquad \text{(VI.1)}$$

Besides, the slot parameters are:

$$(x, y, z) = (1, ls, t) \tag{VI.2}$$

Example II: how to make a cylinder in the desired position.

We need to know the center point (x, y, z), the radius r and the height h. As the figure shown in Figure 1. We try to draw the top cylinder inside the red rectangular. Radius is 0.5, height is t. We just need to determine the center point of the cylinder.

$$(x, y, z) = (-lo, \left(\frac{7}{2} + \frac{3}{2}\right) \cdot \lambda_g + \frac{ls}{2}, h) \tag{VI.3}$$

From the example I and II, we know the method to make prism and cylinder.

Next, we need to know how to multiplate the identical bodies along some direction. We should know the direction vector, the distance between each unit and the numbers of target array.

Another essential process is mirror like rotation. We need first find a point in the axis, and then find the normal vector of the mirror plane.

These basic processes are enough to build basic antenna model in Femtet for a simulation.

List of publications:

International Conference:

[1]. W. Liu and Y. Tsunemitsu, "The Array Antenna for Solar Energy Harvesting from The Sun," in Proc. IEICE and IEEE AWPT, Singapore, 2017, pp. D2-S5-07.

[2]. W. Liu and Y. Tsunemitsu, "The Slotted Waveguide Array Antenna with Reflection Canceling Stairs in Millimeter Waveband," 2020 14th European Conference on Antennas and Propagation (EuCAP), Copenhagen, Denmark, 2020, pp. 1-4, doi: 10.23919/EuCAP48036.2020.9135800.

[3]. W. Liu and Y. Tsunemitsu, "The Waveguide Slot Array Antenna in Millimeter Waveband using the Reflection Canceling Stairs for the Sidelobe Suppression," 2020 IEEE International Symposium on Antennas and Propagation and North American Radio Science Meeting, Montreal, QC, Canada, 2020, pp. 531-532, doi: 10.1109/IEEECONF35879.2020.9329930.

[4]. W. Liu and Y. Tsunemitsu, "Slotted waveguide antenna with inclined stairs for effective side lobes suppression at 38 GHz," 2021 15th European Conference on Antennas and Propagation (EuCAP), Dusseldorf, Germany, 2021, pp. 1-3, doi: 10.23919/EuCAP51087.2021.9411506.

[5]. W. Liu and Y. Tsunemitsu, "A Single-Layer Center-Feed Slotted Antenna Array with Reflection Canceling Stairs in 38-GHz Waveband," 2022 16th European Conference on Antennas and Propagation (EuCAP), Madrid, Spain, 2022, pp. 1-5, doi: 10.23919/EuCAP53622.2022.9769631.

[6]. W. Liu and Y. Tsunemitsu, "Grating Sidelobe Suppression in Single-Layer Center-Feed Waveguide Antenna Array at 38 GHz," 2022 IEEE International Symposium on Antennas and Propagation and USNC-URSI Radio Science Meeting (AP-S/URSI), Denver, CO, USA, 2022, pp. 1220-1221, doi: 10.1109/AP-S/USNC-URSI47032.2022.9887098.

Academic Journal:

[1]. W. Liu and Y. Tsunemitsu, "A Waveguide Slot Array Antenna With Reflection-Canceling Stairs for Sidelobes Suppression at 38 GHz," in IEEE Access, vol. 11, pp. 72942-72949, 2023. doi: 10.1109/ACCESS.2023.3294821

Acknowledgements

I would like to express my deepest gratitude to Professor Shigeru Yoshimori, my principal advisor, for his unwavering support, insightful guidance, and continuous encouragement throughout the entire journey of this doctoral thesis. Professor Yoshimori's expertise, dedication, and mentorship have been instrumental in shaping the direction and quality of this research.

I am also immensely thankful to Associate Professor Yasuhiro Tsunemitsu for his valuable insights, constructive feedback, and dedicated involvement as my co-advisor. His guidance has greatly enriched the depth and scope of this work.

I extend my sincere appreciation to Professor Naohisa Goto, Professor Makoto Ando, and Professor Toshiyuki Maeyama for their contributions to related research aspects. Their expertise and collaboration have significantly influenced the development of this thesis, and I am truly grateful for their support.

A special note of gratitude goes to my family, whose unwavering support has been my pillar of strength. To my parents Zhiqiang Liu and Sumei Meng, your encouragement and belief in my abilities have been a driving force. To my husband Dr. Peng Zhou, your patience, understanding, and encouragement sustained me through the challenges. To my two wonderful daughter Wenzhen Zhou and Wenjing Zhou, your love and joy brought balance to my life, making this academic journey all the more meaningful. Besides, I would like also to appreciate my parents-in-Law Zhihong Zhou and Yangli Gong, for them encouragement in daily life. Specially, I would like to thank my sister Shi Wang, who support me in terms of every aspect of my life.

In closing, I am profoundly thankful to everyone who has been part of this academic endeavor. Your support, encouragement, and collaboration have made this research possible, and for that, I am truly grateful.

Wenbo Liu
2023.11.20